2009

Structural and Functional Considerations in the Design of Collagen-Based Electrospun Scaffolds

Chantal Ayres
Virginia Commonwealth University

Virginia Commonwealth University

This is to certify that the dissertation prepared by Chantal Emma Ayres entitled STRUCTURAL AND FUNCTIONAL CONSIDERATIONS IN THE DESIGN OF COLLAGEN-BASED ELECTROSPUN SCAFFOLDS has been approved by her committee as satisfactory completion of the dissertation requirement for the degree of Doctor of Philosophy.

David G. Simpson, Ph.D., Department of Anatomy and Neurobiology

Gary L. Bowlin, Ph.D., Department of Biomedical Engineering

Michael A. Fox, Ph.D., Department of Anatomy and Neurobiology

Thomas W. Haas, Ph.D., Department of Biomedical Engineering

Hu Yang, Ph.D., Department of Biomedical Engineering

Gerald E. Miller, Ph.D., Chair, Department of Biomedical Engineering

\

Rosalyn S. Hobson, Ph.D., Associate Dean, School of Engineering

Russell D. Jamison, Ph.D., Dean, School of Engineering

F. Douglas Boudinot, Ph.D., Dean of the Graduate School

May 3, 2009

STRUCTURAL AND FUNCTIONAL CONSIDERATIONS IN THE DESIGN OF COLLAGEN-BASED ELECTROSPUN SCAFFOLDS

A Dissertation submitted in partial fulfillment of the requirements for the degree of Doctor of Philosophy in Biomedical Engineering at Virginia Commonwealth University.

by

CHANTAL EMMA AYRES
B.S. Virginia Tech, 2002
M.S. Virginia Commonwealth University, 2004

Director: David G. Simpson, Ph.D.
Associate Professor, Department of Anatomy and Neurobiology

Co-Director: Gary L. Bowlin, Ph.D.
Associate Professor, Department of Biomedical Engineering

Virginia Commonwealth University
Richmond, Virginia
May 2009

Acknowledgement

First, I'd like to express my gratitude to everyone at VCU who has helped me through these years. Much of the time, this help came in the form of laughter. Thank you to everyone in the Bowlin lab, with special thanks to Scott Sell and Michael McClure. Their combination of technical expertise and witty banter will never be forgotten. In the Simpson lab, we've had a number of people filter in and out but the gut wrenching amusement I got from Hurricane Henrietta and Magdon helped me through many days (although I don't think Henrietta and Magdon realized they were providing such hilarity). I will never look at tanning spray, wedding rings or Fan restaurants the same again. A huge and special thanks goes out to Thomas Turner and Rusty Bowman- the camaraderie I shared with both of them was unmatched and the days would have been endlessly long without them. I will certainly miss their "interesting" humor and huge smiles. The best thing about being with them is that together, they can make anything funny (even things that really shouldn't be). I'd also like to express my appreciation to my committee- Dr. Michael Fox, Dr. Thomas Haas and Dr. Hu Yang. Their expectations and concerns were always right on point. To Dr. Gary Bowlin, who has helped me immeasurably these past few years- thank you! For helping me to get a teaching assistantship and all your crazy observant editing (how do you even notice that stuff?) I am truly grateful. Last but not least- a gigantic thank you to Dr. David Simpson for all his help and guidance. Sometimes I wanted to hug him and sometimes I wanted to strangle him but I always knew that whatever crazy idea he had was best for me in the long run. I am forever indebted to you and can only hope that you think twice about some of your more dangerous plans when I am not there to tell you it's a bad idea (and please remember to turn the power supply off!). Finally, thank you to my friends and family for all their support and guidance through the years. I have enormous appreciation for all of you, especially Mom, Dad, Collette, Marc and Matthew. My last acknowledgement goes out to my husband-to-be, Christopher Sander. I'm not sure if could get through an entire day without you, let alone the past 4 years of my doctoral research. You have put up with my measly stipend and constant moaning for many years now- how on earth did you do it? As always, your support and love has been completely unwavering and I consider myself a ridiculously blessed and lucky person to have ever found you.

Table of Contents

List of Tables

Page

List of Figures

Page

List of Abbreviations

α-SMA	Alpha-smooth muscle actin
ANOVA	Analysis of variance
CTGF	Connective tissue growth factor
ECM	Extracellular matrix
EGF	Epidermal growth factor
FFT	Fast Fourier transform
HFIP	Hexafluoroisopropanol
IL-1	Interleukin-1
MMP	Matrix metalloproteinases
PBS	Phosphate buffered saline
PCL	Poly(ε-caprolactone)
PDGF	Platelet derived growth factor
PDS	Polydioxanone
PEG	Poly(ethylene glycol)w
PGA	Poly(glycolide)
PLGA	Poly(lactide-co-glycolide)
PLA	Poly(lactide)
PU	Polyurethane
RGD	Arginine-glycine-aspartate
RPM	Revolutions per minute
SEM	Scanning electron microscopy
TFE	trifluoroethanol
TGF-β	Transforming growth factor-beta
THF	Tetrahydrofuran
TIMP	Tissue inhibiting matrix metalloproteinases
TNF	Tumor necrosis factor

Abstract

STRUCTURAL AND FUNCTIONAL CONSIDERATIONS IN THE DESIGN OF COLLAGEN-BASED ELECTROSPUN SCAFFOLDS

By Chantal Emma Ayres, M.S.

A Dissertation submitted in partial fulfillment of the requirements for the degree of
Doctor of Philosophy in Biomedical Engineering at Virginia Commonwealth University.

Virginia Commonwealth University, 2009

Director: David G. Simpson, Ph.D.
Associate Professor, Department of Anatomy and Neurobiology

Co-Director: Gary L. Bowlin, Ph.D.
Associate Professor, Department of Biomedical Engineering

Electrospinning can be used to selectively process a variety of natural and synthetic polymers into highly porous scaffolds composed of nano-to-micron diameter fibers. This process shows great potential as a gateway to the development of physiologically relevant tissue engineering scaffolds. In this study we examine the structural and functional considerations regarding electrospun scaffolds for dermal template applications using novel quantification techniques. In order to characterize scaffold structure, a technique utilizing the fast Fourier transform was developed to systematically quantify fiber alignment and evaluate how different electrospinning parameters impact the structure and material properties of an electrospun scaffold. Gelatin was suspended at varying concentrations (80, 100, 130 and 150 mg/ml) and electrospun from 2,2,2 trifluoroethanol onto a rotating mandrel (200-7000 RPM). Scaffold anisotropy developed as a function of fiber diameter and mandrel speed and the induction of varying degrees of anisotropy imparted distinctive material properties to the electrospun scaffolds. Fiber alignment was the variable most closely associated with the regulation of peak stress, peak strain and modulus of elasticity. Next, we examined how the chemical and physical composition of the local microenvironment and the unmasking of possible RGD sensitive binding sites through collagen denaturation, independent of scaffold architecture and porosity, impacts cellular processes. We cultured human dermal fibroblasts on electrospun nylon coated with a variety of non-denatured and thermally denatured collagen-based proteins, as well as recovered electrospun collagen and gelatin (in an effort to examine if the electrospinning process degrades the collagen α chain). Differences in adhesion, proliferation and migration were exhibited between collagen-based proteins. Adhesion inhibition assays using a cyclic RGD peptide demonstrated no change in cell adhesion on non-denatured proteins and a significant drop in cell adhesion on thermally denatured proteins. Based on gel analysis and the results of our functional assays we conclude that collagen α chain structure is not directly altered by the electrospinning process. Overall, these results are critical to the understanding of how structure and architecture contribute to the overall properties of a scaffold, as well as how molecular variations can modulate scaffold functionality in a cellular environment.

CHAPTER 1 Wound Healing

Injuries to the skin and the subsequent healing of a wound represent a complex process that occurs on a continuum. At one extreme of this continuum, the tissue undergoes regeneration and there is a complete restoration of normal structure and function. This positive result usually occurs in younger patients while in the adult, wound resolution typically occurs at the other extreme of the continuum and the dermis is reconstituted as scar tissue. As a non-functional analog of the dermis, scar tissue can subject the patient to physiological as well as psychological complications. Scar tissue is inelastic, painful, often disfiguring and can drastically limit joint movement. Implanting dermal regeneration templates (comprised of model structural and biologic properties) to act as a substitute for the provisional matrix may enhance the wound healing process and tip the scales toward scarless wound healing.

STRUCTURE OF NORMAL SKIN

Epidermis: Compositional and Architectural Features. Intact skin is structurally and functionally divided into the epidermal and dermal compartments. These compartments are separated by a basal lamina rich in Type IV collagen and laminin-5 [2]. The epidermis, or outer layer of the skin, is cellular in nature and in a state of constant turnover [3]. Keratinocytes represent upwards of 90% of the total cell population and form a multi-layered, hydrophobic barrier that protects the underlying dermis from dehydration [4]. Melanocytes, Merkel cells and Langerhans cells are also present in the epidermis. Melanocytes produce pigments that determine skin color, Merkel cells mediate cutaneous innervation and Langerhans cells regulate aspects of immune surveillance. As a consequence of its cellular composition, injuries to this superficial layer of the skin (also known as partial thickness injuries) commonly result in the regeneration of a functional epithelium [5]. The dermo-epidermal junction is composed of reticulin fibers and small collagen fibrils [3]. *Rete* pegs, macroscopic protrusions of the epidermal layer, project at irregular intervals into the dermis. These structures increase surface area and the adhesion of the epidermis to the dermis. This junction is unique in each area of the body and with aging a flattening of these ridges is commonly seen [6].

Dermis: Compositional and Architectural Features. The dermis, or deeper layer, makes up the greater part of skin and is an irregular, fibrous network of connective tissue embedded in an amorphous ground substance that functions to resist compression [3]. The dermis is sparsely populated by interstitial fibroblasts and macrophages. Fibroblasts produce and remodel the collagen that serves as the backbone of this tissue. Nutrients are supplied by the numerous small caliber blood vessels that are present. The many functions of the dermis include defense from mechanical injury, supplying oxygen and nutrients to the epidermis and allowing joint movement and stretch [6]. When both the epidermal and dermal layers of the skin are compromised (also known as a full thickness injury), wound healing is characterized by varying amounts of both regeneration and scarring [7][8].

The dermis of the skin is further subdivided into a papillary layer and reticular layer. These domains are continuous with one another and have no distinct borders; each contains specific collagen isotypes and exhibits distinctive architectural features [2][9]. The papillary layer, found directly beneath the epidermis, is comprised primarily of Type III collagen and a small quantity of Type I collagen. The fibers in this layer exhibit smaller cross-sectional diameters than those found in the reticular layer and are modestly aligned in parallel with the local lines of tension (e.g. Langers' lines). The deeper layer, the reticular dermis, is composed of dense, random arrays of Type I collagen organized into large-scale bundles [10-12]. Type III collagen is present, but at substantially lower concentrations than Type I collagen. Notably, with electrospinning it is theoretically possible to process collagen into tissue engineering scaffolds that are composed of fibers that approximate the size scale and architecture observed in the native dermis [13-16].

EVENTS LEADING TO WOUND RESOLUTION

Wound resolution in a full-thickness injury involves a complex, orchestrated series of events. The healing process is affected by various factors ranging from the initial severity of the injury, the age of the individual and intrinsic or extrinsic factors. Intrinsic factors include the health of the patient: presence or absence of disease, age, immune status, and nutritional state. Extrinsic factors include complications at the injury site: degree of wound contamination, infection and necrosis, and presence or absence of medications. Keratinocytes and interstitial fibroblasts mediate the majority of the events that are necessary to resolve a wound. The events that take place during wound healing overlap in time and can be sub-divided into inflammation, tissue formation and tissue remodeling [1]. Perturbations that impact the natural progression of these processes exacerbate scar formation [18-20].

Inflammation. During this phase, platelet activation and aggregation, fibrin clot formation and clot remodeling occur. These primary events of the wound healing cascade take place over a time frame of minutes to hours. All of these actions work to reestablish hemostasis in the wound bed. Platelets delivered to the injury via blood vessels undergo activation and spread, leading to the accumulation of additional platelets within the developing thrombus and hemostasis. Platelets facilitate the assembly of a fibrin plug and release PDGF (platelet derived growth factor) to recruit macrophages and fibroblasts to the area [1][21]. The platelet plug and fibrin clot produced during this phase mark the onset of the evolution of a provisional wound matrix or "natural dermal template" for the subsequent stages of the healing process [1][37]. Next, monocytes infiltrate the wound bed from blood vessel walls, differentiate into macrophages and release PDGF as well as vascular endothelial growth factor (VEGF), molecules that instigate the formation of granulation tissue [1]. These macrophages also bind to the ECM and become phagocytotic, engulfing microorganisms and ECM fragments that are present in the wound [1]. Adherence to the ECM also causes monocytes and macrophages to express a variety of growth factors that are critical to the initiation and diffusion of tissue formation. Principal signaling molecules released by monocytes and macrophages include colony stimulating factor 1 (CSF-1), TNF-α (tumor necrosis factor-α), TGF-α (transforming growth factor-α), EGF (epidermal growth factor), IL-1 (interleukin-1), leukotrienes and notably, in the adult, TGF-β1 and TGF-β2 [1][21]. TGF-β3 predominates in fetal tissues where the continuum of healing favors regeneration [22-24]. Overall, the presence of monocytes and macrophages in a wound bed is essential for the transition between tissue inflammation and formation and sets the stage for eventual wound resolution [1].

Tissue Formation. Re-epithelialization begins shortly after injury and functions to approximate the architecture of the tissue prior to wounding and reestablish the basement membrane. Initially, epidermal cells undergo a phenotypic change to allow cell movement; these cells then release MMP-1 to degrade the ECM and begin to migrate inward from the periphery of the injury. One to two days after the initial injury, these cells begin to proliferate at an accelerated rate and express basement membrane proteins [1]. As re-epithelialization occurs, a new basement membrane is established from the margin of the wound inward [1]. The basement membrane is formed as cells migrate; when these cells take up residency and begin to proliferate and differentiate, an increased quantity of basement membrane is produced. Epidermal cells then return to their original phenotype and reattach themselves to the newly formed basement membrane and underlying dermis.

Granulation tissue, a provisional matrix that evolves from the platelet plug and fibrin clot that mark inflammation, is enriched in fibrin, fibronectin, collagen and gelatin and is characterized by newly formed capillaries and develops approximately four days after injury. Fibroblasts are signaled to penetrate the provisional matrix in response to PDGF, as they enter the wound bed they synthesize and deposit new ECM. During this interval of the wound healing cascade macrophages release a steady stream of growth factors (namely TGF-β and PDGF) to stimulate tissue formation and angiogenesis [1]. At the close of the tissue formation phase the provisional matrix is composed of fibrin, fibronectin and hyaluronic acid, this provisional matrix will eventually be replaced by a collagenous matrix. After the synthesis, deposition and remodeling of the ECM, fibroblasts undergo apoptosis, resulting in a primarily acellular scar [1].

Tissue Remodeling. During the remodeling stage the provisional matrix is transformed into granulation tissue, this process is marked by the differentiation of fibroblasts into the myofibroblast [25]. Myofibroblasts, a highly contractile phenotype, express α-smooth muscle actin (α-SMA) at increased rates, develop increased intrinsic capacity to contract and begin to apply tension across the provisional matrix/granulation tissue, an action that pulls the free edges of the wound inward, reducing the total surface area of the injury [25]. Molecular markers of the myofibroblast include an increased expression and accumulation of α-SMA (regarded as the most reliable myofibroblast marker) [26][27], increased expression of fibronectin [25][28] and αvβ5 integrin expression [29]. Myofibroblast contraction is stimulated by TGF-β1, TGF-β2, PDGF, matrix stiffness and attachment of fibroblasts to the collagen matrix through cell adhesion complexes [1]. Aside from the presence of α-SMA, myofibroblasts also differ from fibroblasts in manner in which they are linked to surrounding extracellular environment, this cell type expresses focal adhesions that are significantly larger than those of classical fibroblasts (8-30 μm compared to 2-6 μm) [34]. These focal adhesions, termed "super mature" focal adhesions, exhibit a precise molecular composition and contain large amounts of vinculin, paxillin, tensin and integrins αvβ3 and α5β1 [34].

Wound healing progression and the formation of dermal constituents are modulated by matrix metalloproteinases (MMP's) secreted by cells. These proteases function in the extracellular environment and function to degrade ECM proteins, they are also thought to influence various cell processes such as proliferation, migration and differentiation [1][25]. The extent and quality of tissue remodeling during the transition between granulation tissue and scar formation depends highly upon the rate of collagen synthesis and degradation. MMP function is regulated by a complex regulatory cascade; these enzymes are deposited into the ECM as inactive pro-enzymes. They are stablizied in this state by small peptides, the tissue inhibiting matrix metalloproteinases (TIMP's) [1][25]. The pro-MMP peptide is converted at the cell membrane by MT-1MMP (MMP-14), a membrane bound protease, into an active enzyme.

During early remodeling, the balance of MMP and TIMP mediated regulation favors matrix deposition; in the later stages the balance veers towards matrix degradation [35]. Impaired ECM reorganization in chronic wounds may be related to decreased levels of MMP expression (specifically MMP-1 and MMP-2) caused by increased expression of

TIMP's (specifically TIMP-1 and TIMP-2) [38]. These observations correspond with published results from another laboratory that measured an increased MMP to TIMP ratio in scarless wounds [30]. MMP expression can be controlled through growth factors (such as PDGF and TGF-β) and integrins, cell surface receptors that allow cells to distinguish specific elements of the surrounding environment [31]. The ability of cells to environmentally discriminate underscores the vital role that dermal template composition may play in regulating the wound healing cascade [17].

Myofibroblast Differentiation and Scar Formation. The myofibroblast represents a critical marker of tissue remodeling. These cells may originate from resident interstitial fibroblasts that populate tissues adjacent to the injury and from a circulating pool of CD45+ leukocytes called fibrocytes [32-34]. The relative contribution of each cell source to the myofibroblast population remains to be fully delineated. Fibroblasts initially differentiate into an intermediate cell type known as the proto-myofibroblast. This differentiation is caused by the composition, organization and mechanical properties present in the ECM surrounding the fibroblast, as well as locally released soluble signals known as cytokines [34]. The major function of this cell type is tissue remodeling and the proto-myofibroblast only applies a nominal amount of tension across the matrix. β and γ-cytoplasmic actin stress fibers, isoforms present in non-muscle cells, are found in both quiescent fibroblasts and proto-myofibroblasts [34]. The actin of fibroblasts is arranged in a cortical network and this cell type lacks significant contractile capacity (with respect to the myofibroblast); the proto-myofibroblast expresses more actin and elaborate stress fibers, factors that underlie the increased contractile capacity of this phenotype [35]. As a function of the matrix stress developed during remodeling, proto-myofibroblasts differentiate into myofibroblasts and express bundled α-SMA stress fibers. TGF-β1 induces the myofibroblast differentiation program through a Smad dependent intracellular signal pathway [35] [39]. TGF-β1 initiates the release of CTFG (connective tissue growth factor) and these cytokines act in tandem to promote myofibroblast differentiation. Additionally, integrin αvβ5 has been implicated in myofibroblast differentiation [29]. However, even in the presence of high levels of TGF-β1, myofibroblasts will only exhibit contractile activity with a sufficiently rigid matrix [34].

The presence of α-SMA positive stress fibers greatly enhances myofibroblast contractile capacity. The appearance of these fully differentiated cells marks the onset of the contractile phase of wound remodeling [34][35]. Myosin II stress fibers are also present in myofibroblasts; these fibers attach to actin fibers by the phosphorylation of myosin light chain kinase (MLCK) and are inactivated by the dephosphorylation of myosin light chain phosphatase (MLCP) [36]. Stress fiber contraction is modulated by MLCK in response to intracellular Ca^{2+} and is rapid when MLCP is activated. Conversely, stress fiber contraction is sustained when MLCP is inactivated by the Rho/ROCK (Rho-kinase) pathway [36]. Recent studies have shown that myofibroblast contraction is modulated by MLCP inactivation by the Rho/Rock pathway, indicating that this mechanism may be able to promote sustained rather than rapid wound closure [36]. Rho, a family of GTP-binding proteins, acts as a molecular switch to regulate various cell processes. More specifically, the RhoA GTP-ase has been shown to control stress fiber and focal adhesion formation through the activation of ROCK and may be modulated by TGF-β1 [58].

Myofibroblasts halt their wound contraction and undergo apoptosis when wound tissue is adequately repaired. Myofibroblast activity that does not stop when the tissue is sufficiently repaired leads to tissue deformation and scarring [34]. Processes that may develop as a function of very slow or rapid wound contraction, such as insufficient or excessive remodeling, may also influence the quality of wound resolution. While the mass suicide of myofibroblasts following wound resolution is not completely understood, it is believed to occur in response to a reduction in stress experienced by the cells and an increase in cell-cell contact [34].

WOUND HEALING MODEL

The major events that underscore wound healing can be loosely divided into inflammation, tissue formation and tissue remodeling. Wound healing can be more specifically differentiated by the development of the fibrin clot, provisional matrix and granulation tissue. The formation of these structures is crucial to the wound healing process; the timing and progression of these events influences eventual wound resolution and scar formation. A variety of devices, called dermal regeneration templates, have been developed in attempts to modulate the wound healing process and promote scarless (or at the very least, reduced scarring) wound healing.

Dermal regeneration template implantation focuses on the early stages of inflammation and the provisional matrix. Initially, the provisional matrix is predominantly composed of fibrin, fibronectin and hyaluronic acid; constituents that represent an “immature” matrix. Implanted dermal templates are usually composed of materials that are characteristic of a more “mature” matrix similar to the provisional matrix seen later in wound healing (which is composed primarily of collagen). The possible problem in this scenario is the placement of a “mature” matrix in an environment primed to respond to an “immature” matrix. The constituents and signals in the environment must adapt and continue the wound healing process to reflect the material in place. This adaptation may indicate why matrix synthesis and degradation, as well as differentiation, appears to occur more readily on dermal fibroblast plated gelatin scaffolds versus collagen scaffolds [17]; the presence of collagen may indicate an already remodeled wound matrix. However, experiments conducted in our laboratory indicate that implanted gelatin scaffolds appear to induce significant inflammation, retard cell penetration and increase scar formation. Conversely, implanted collagen scaffolds appear to cause minimal inflammation, promote cell penetration and induce less scarring than implanted gelatin scaffolds. A dermal template composed of a combination of these two materials may stimulate the various poor wound remodeling processes seen on collagen scaffolds while reducing the considerable inflammation induced by gelatin scaffolds.

TISSUE ENGINEERING: LIMITATIONS

The ability to fabricate tissues in vitro for use in reconstructive therapy in vivo has encountered both biological and technical limitations. In vivo, normal developmental processes take place over an extended period of time. During embryonic development the mass and density of tissues increases in parallel with the volume of capillaries present and the capacity of the cardiovascular system to deliver oxygen and provide nutrient exchange. In these embryonic tissues, "timing" is perfect with regards to oxygen need and delivery; in areas of high oxygen demand, there is high capillary growth. In the bioengineering paradigm, the degree of development and, eventually, the fate of the tissue (i.e. survival), is dependent upon capillary in-growth and oxygen delivery/nutrient exchange. Bioengineered tissue fabricated in vitro lacks cardiovascular support and must be sustained by passive diffusion when it is implanted in vivo. If passive diffusion does not deliver adequate oxygen and nutrients, tissue death occurs. This consideration greatly limits the mass and density of tissue that can be fabricated and supported in vitro

Limiting the mass of an implant has consequences on implant performance. For example, while it is possible to fabricate small pieces of cardiac-like tissue, it is unclear if this type of tissue could provide a meaningful benefit to a recipient patient. Increasing the mass of this type of implant would clearly increase its overall performance profile and enhance its ability to truly augment cardiac performance. However, as the mass and cellular density of this type of tissue is increased, the diffusion barriers that must be circumvented to support the tissue become increasingly more difficult to overcome.

Preparing bioengineered tissue in a bioreactor (a generic designation for a device designed to increase nutrient exchange) can, to some extent, increase the mass of tissue that can be supported in vitro. However, when first implanted, any tissue fabricated in vitro must still be supported by the passive diffusion of nutrients from the surrounding interstitium until a functional capillary network and nascent interconnections with the cardiovascular system of the host develop.

These observations underscore the essential role that tissue engineering scaffolds play in the bioengineering paradigm. These scaffolds must have sufficient mechanical integrity to support an implant, yet support rapid capillary formation. Additionally, scaffolds must readily support cell infiltration and allow for scaffold penetration in three-dimensional space. Scaffolds must have a high degree of biocompatibility, otherwise any immune reaction will have to be managed, adding additional burdens to patient recovery for any procedure in which engineered tissues are used to reconstruct damaged or missing organs.

Identifying suitable materials to be used in the fabrication of tissue engineering scaffolds remains critical to advancing this field of medicine. While several candidates have been identified it remains unclear which material will undergo more complete development. In summary, for many applications, an ideal material is one that exhibits excellent biocompatibility (low inflammatory potential) and supports rapid and extensive capillary growth.

OVERVIEW

This study examines the structural and functional considerations regarding electrospun scaffolds for tissue-engineering applications. While this work focuses on the use of electrospun scaffolds as dermal templates for improving wound resolution, the techniques and assays developed to examine the structural and functional aspects of these materials are applicable for use in a variety of arenas and scaffold production methods. The major idea here is that material identity and *initial* fabrication parameters (factors that control material and molecular properties, as well as signaling cues for cells) have a profound impact on the overall functionality of a scaffold. Recent research in tissue engineering has focused on mimicking the complex and multifunctional nature of the native ECM (a scaffold whose composition and architecture has a profound impact on the phenotypic and functional properties of a cellular compartment); this task is entirely unfeasible unless there is an understanding regarding how scaffold structure develops and how the functionality of a scaffold can be modulated by initial considerations (i.e. material identity, fiber alignment, pore size, fiber size, etc.). The remainder of this document is organized into chapters in the following order:

- Nanotechnology in the design of scaffolds: innovations in structure and function (currently under review for publication in *Wiley Interdisciplinary Reviews: Nanomedicine, 2009*)

- Measuring fiber alignment in electrospun scaffolds: a user's guide to the 2D fast Fourier transform approach (published in the *Journal of Biomaterials Science, Polymer Edition, 2007, volume 19, pages 603-621)*
- Modulation of anisotropy in electrospun tissue-engineering scaffolds: analysis of fiber alignment by the fast Fourier transform (published in *Biomaterials, 2006, volume 27, pages 5524-5534)*
- Incremental changes in anisotropy induce incremental changes in the material properties of electrospun scaffolds (published in *Acta Biomaterialia, 2007, volume 3, pages 651-661)*
- Investigation of Dermal Fibroblast Adhesion on Denatured Electrospun Materials (in the process of being submitted for review in *Biomaterials* at the time this document was prepared)

This document begins with a review covering the current scaffold production methods and recent advancements with regards to the overall structure and function of a scaffold, specifically examining recent innovations in scaffold composition, architecture and the use of bio-techniques during scaffold fabrication. Next, a review detailing the use of the fast Fourier transform (FFT) for measuring fiber alignment in a scaffold is given. This powerful characterization tool can be used to assign a numerical value to fiber alignment, a scaffold feature that plays a central role in determining the material properties of a scaffold, as well as acting as a source of guidance cues for cells. The detail in which the FFT technique is discussed in this section will enable readers to better understand the use of the FFT method to investigate scaffold structure. The next chapter demonstrates the effect of fiber diameter and mandrel speed on the induction of anisotropy in an electrospun scaffold (as measured by the FFT technique). Additionally, the effect of electrospinning voltage and air gap distance on fiber alignment was examined during this study but was not included in the final paper (the work regarding these details can be found in Appendix A). The subsequent chapter examines how changes in fiber diameter, fiber alignment (as quantified by the FFT technique) and angle of testing modulate the material properties of an electrospun scaffold. The final chapter in this document examines the development and use of a series of novel assays for the systematic evaluation of protein structure. These investigations were conducted in an effort to examine how the chemical and physical composition of the local microenvironment and the unmasking of possible RGD sensitive binding sites through collagen denaturation, independent of scaffold architecture and porosity, impacts cellular processes. The divulgence of binding sites following tissue injury may act as a signaling cue for cells and the presence of degraded proteins in a tissue-engineering scaffold may be advantageous. In addition, the results of these assays were used as a barometer to investigate if the electrospinning process alters collagen function. Overall, the results discussed throughout this document are critical to the understanding of how structure and architecture contribute to the overall properties of a scaffold, as well as how molecular variations can modulate scaffold functionality in a cellular environment. Understanding and characterizing these elements is crucial for the facilitation of a meaningful and clinically-relevant dermal template.

CHAPTER 2 Advancements in Scaffold Design

Preface: The following manuscript is currently under review for publication in Wiley Interdisciplinary Reviews: Nanomedicine, 2009 [16]. The work included explores the current tissue-engineering scaffold production methods as well as scaffold advancements with regard to composition, architecture and bio-techniques.

Nanotechnology in the Design of Tissue-Engineering Scaffolds:

Innovations in Structure and Function

CE Ayres[1], BS Jha[2], SA Sell[1], GL Bowlin[1] and DG Simpson[2]

[1]Department of Biomedical Engineering
Virginia Commonwealth University
Richmond, VA 23284

[2]Department of Anatomy and Neurobiology
Virginia Commonwealth University
Richmond, VA 23298

ABSTRACT

Engineered scaffolds function to supplement or replace injured, missing or compromised tissue or organs. The current direction in this research area is to create scaffolds that mimic the structure and function of the native extracellular matrix (ECM). It is believed that the fabrication of a scaffold that has both structural integrity and allows for normal cellular function and interaction will bring scaffolds closer to clinical relevance. Nanotechnology innovations have aided in the development of techniques for the production of nanofiber scaffolds. The three major processing techniques, self-assembly, phase separation and electrospinning, produce fibers that rival the size of those found in the native ECM. However, the simplicity, versatility and scalability of electrospinning make it an attractive processing method that can be used to reproduce aspects of the complexity that characterizes the native ECM. Novel electrospinning strategies include alterations of scaffold composition and architecture, along with the addition and encapsulation of cells, pharmaceuticals and growth factors within the scaffold. This paper will review the major nanofiber fabrication technologies as well as delve into recent significant contributions to the conception of a meaningful and practical electrospun scaffold.

INTRODUCTION

Engineered scaffolds are designed to augment or completely replace damaged, missing or otherwise compromised tissue or organs. These scaffolds may be permanently integrated into or bioresorbed by the body and must be capable of mimicking the conditions and characteristics present in local microenvironments throughout the mammalian organ system. The extracellular matrix (ECM) not only defines the three-dimensional architecture of an organ but is also engaged in a complicated relationship with the cellular elements that populate the surrounding environment. Biochemical and mechanical events can induce changes in the local microenvironment that modulate the composition and architecture of the ECM. In turn, these changes in the ECM can regulate the phenotype and functional properties of the cellular compartment. Communication between the cell and ECM molecules influences various cellular processes, such as adhesion, proliferation, differentiation, migration and apoptosis, as well as growth factor and cytokine modulation. The timing of these events critically affects tissue formation and remodeling, processes that are crucial for the integration of a scaffold into the surrounding environment. The fibers that make-up the backbone of the elaborate ECM network exhibit distinctive, and often times, regional variations in identity, cross-sectional diameter and polarity. For example, the ECM of the dermis can be subdivided into two discrete sub-compartments, a deep reticular layer and a superficial papillary layer. The reticular compartment is occupied by large diameter fibers of Type I collagen and elastin that are distributed into large-scale random bundles. Conversely, the superficial papillary layer of the skin contains small diameter fibers of Type III collagen and elastin that exhibit a modest degree of anisotropy. In order to produce a functional scaffold and improve over previous generations of scaffolds, the complex and multifunctional nature of the ECM must be characterized and replicated.

Advancements in nanotechnology, specifically in the field of nanofiber fabrication, have shown great promise with respect to developing clinically relevant scaffolds. Research in this arena focuses largely on the design and fabrication of nanofibers composed of natural and/or synthetic materials. Self-assembly, phase separation and electrospinning can all be used to successfully generate nanofibers well within the range of fibers present in the native ECM (50 to 500 nm) [41]. This review will focus on the method of electrospinning for the production of soft tissue scaffold implants; the electrospinning process is simple, rapid and allows for the production of scaffolds of various shapes, sizes and materials (both natural and synthetic) [13][42][43]. The latest innovations in electrospun scaffolds cover a broad range of exploration from using novel materials alone or in concert with other materials, to achieving a high level of control over scaffold architecture, to electrospinning polymer solutions with cells, antibiotics and growth factors. This paper will provide a review of existing nanofiber fabrication techniques as well as focus on present research developments involving electrospun scaffolds.

SCAFFOLD PRODUCTION METHODS

The native ECM is an elaborate network whose composition and structure can modulate the phenotype of the resident cells within a tissue or organ [44][45]. Scaffolds that can mimic the composition, structure and function of the native ECM represent a potential gateway to the production of clinically relevant scaffolds. Presently, the major techniques for the fabrication of nanofiber scaffolds are self-assembly, phase-separation and electrospinning.

Self Assembly. Self-assembly is the organization of disordered molecules into structures or patterns without external intervention. The most commonly researched self-assembled nanofibers, peptide amphiphiles (PAs), were initially developed by Berndt et al. for use in investigating the interaction between peptide structures and ligands [59]. PA systems are ligand-receptor pairs that are integrated into separate lipid molecules and fixed by means of self-assembly onto a surface [59]. PAs are composed of a hydrophilic peptide head group (a N-alpha amino group) attached to a hydrophobic tail group (a dialkyl chain moiety) and were originally developed using peptide sequences from collagen fragments [46][47]. Both dialkyl and monoalkyl PAs self-assemble and form a stable triple helix conformation [47]. Self-assembled PA nanofibers can have fiber diameters as small as 10 nm and pore sizes of 5-200 nm (well within the range of the native ECM and significantly smaller than those produced through electrospinning) [46][48]. Cells cultured in self-assembling peptide scaffolds have been reported to show functional cell behaviors and in some instances improved proliferation and differentiation [48][49]. However, the poor mechanical strength of self-assembled PA nanofiber scaffolds allows them to be used only under certain conditions; this technique has shown great promise when utilized in concert with other materials and/or techniques or when employed for purposes other than a stand alone tissue scaffold [49]. The Stupp laboratory has contributed significantly to the development and advancement of this technique. For example, these researchers developed heparin binding peptide amphiphiles (HBPAs) to bind and deliver growth factors through bioactive heparin [50]. Diabetic rats were transplanted with isologous islets and HBPA growth factor delivery scaffolds; results showed that blood vessel density in the implantation site and islet engraftment was improved and HBPA recipients reached normal blood glucose content at a higher rate than controls [50]. In addition, the Stupp laboratory demonstrated PA nanofiber scaffolds to be good candidates for use as bioactive implant surfaces [51]. In an effort to turn inert titanium foam into a bioactive implant, porous titanium was filled with PA nanofiber matrix; after 4 weeks, when used as a bone plug model in rat femurs to help implant fixation, bone formation was found inside and around the implant [51]. The development of self-assembled bioactive hydrogels has also been explored; the presence of various peptides on a simple hydrogel can alter the structure and biological activity of these gels [102-104]. Poly(ethylene glycol) (PEG)-based hydrogels containing arginine-glycine-aspartate (RGD) peptides and matrix metalloproteinase (MMP) substrates may be used for higher control over a matrix system [102][103]. In addition, altering the number of arms on the PEG macromer building blocks allows for control over the modulus of the gel [104]. While the self-assembly technique produces fibers that very closely approximate the size-scale of the native ECM, issues regarding scaffold mechanical properties and high complexity limit the use of this method as a large-scale scaffold fabrication option.

Phase Separation. To produce highly porous nano-fibrous scaffolds, Ma and Zhang utilized the already existing phase separation technique. Using biodegradable and biocompatible aliphatic polyesters such as poly(lactide) (PLA) and poly(glycolide) (PGA), fiber sizes from 50-500 nm and 98.5% porosities can be achieved by a thermodynamic separation of a polymer solution [41][47][52]. To produce these scaffolds, a polymer is dissolved in a solution, typically tetrahydrofuran (THF), then phase separated thermally or by adding a non-solvent to the polymer solution, creating a gel [41] [46] [52]. The solvent is then extracted from the gel using water and the gel is frozen and freeze-dried under vacuum [47][52]. Polymer gelation (time and temperature) is undoubtedly the most important step in this technique, controlling porosity and fiber size [47]. One of the most advantageous characteristics of this technique is that pore size and structure can be closely controlled by a number of porogens, such as sugar, inorganic salt and paraffin spheres [41][53][54]. However, the high level of control over these scaffold characteristics is clouded with issues regarding lingering porogen compounds post-extraction. Regardless, cell populations have demonstrated high growth and functionality on these scaffolds and these constructs may work well in bone tissue engineering [55][56]. In addition, layered phase separation scaffolds are being investigated with various biomolecule coatings (such as matrigel, collagen type I and III and elastin) for small diameter tube scaffolds or with multiple polymers (such as polyurethane (PU) and collagen) for nerve conduits [57][58]. While this technique is simple and consistent, issues regarding porogen extraction, the restricted number of usable polymers and the fact that it is not obviously amenable to large-scale production limits the practical use of this method for scaffold production[41][47].

Electrospinning. Electrospinning is a non-mechanical processing method that can be used to selectively fabricate nano to micron diameter fibers from a variety of synthetic polymers and natural proteins [13][61]. Electrospinning uses an electric field to process a polymer solution into a fibrous construct (Figure 2.1) [42]. In this process a polymer solution or melt is prepared in a suitable reservoir; bench scale devices typically use a syringe. This starting material is then charged to a high potential and directed towards a grounded target separated from the source by some distance (generally in the range of 10-30 cm). Typically, the electrospinning solution is fed at a metered rate into the electric field from a blunt-tipped needle. The electric potential drives the solution across the air gap that separates the source solution from the target ground. The carrier solvent evaporates as the material is driven across the air gap, resulting in the formation of discrete fibrils that deposit as a non-woven matrix. The nature of the process allows for the production of very small diameter fibrils with interconnected pores [13].

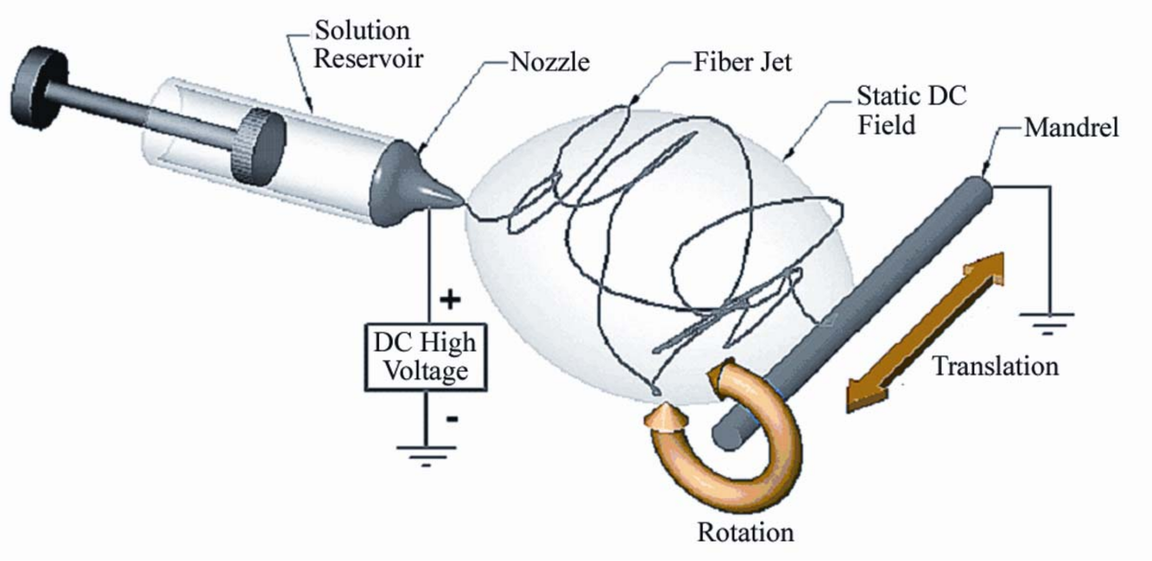

Figure 2.1. Schematic depicting the electrospinning process. A polymer solution or melt is charged to a high potential and directed toward a grounded target. The electric potential drives the polymer solution across the air gap and as the carrier solvent evaporates, discrete fibers are deposited as a non-woven matrix.

The material and biological properties of electrospun scaffolds can be regulated at several sites in the electrospinning process. Structural and functional characteristics can be modulated through compositional considerations; a variety of natural protein and synthetic polymers can be electrospun separately or in tandem to produce blended composites [43][62]. Our laboratories have successfully electrospun a wide variety of synthetic polymers such as PLA, PGA, polydioxanone (PDS), nylon and nitrocellulose as well as natural polymers such as collagen (types I, II, III and IV), gelatin, elastin and fibrinogen (Figure 2.2) [13-15][43][60-62][64][65]. Physical properties, including fiber diameter and pore dimension, can be regulated by controlling the composition of the electrospinning solvent and the identity, concentration, and/or degree of chain entanglements (viscosity) present in the starting polymer(s) [13][14][61]. Generally, fiber and pore diameter increase as the starting polymer concentration increases (Figure 2.3). During the electrospinning process, fiber alignment and overall scaffold anisotropy can be selectively controlled by mandrel speed and polymer concentration [14][63]. Higher mandrel rotational speeds and larger fiber diameters yield more highly aligned scaffolds. A variety of post-electrospinning processing techniques can be used to further tailor scaffold properties; for example, the material properties of a scaffold composed of natural proteins can be regulated by varying the degree of cross-linking present in the scaffold [64]. Overall, this technique is simple, inexpensive and versatile, allowing for a wide range of production materials and scaffold structure. However, there are various limitations with electrospinning including fiber sizes that are on the upper scale of fibers that approximate the size of those found in the ECM and the use of organic solvents to prepare polymers for electrospinning. Published results by Zeugolis et al. maintain that electrospun collagen solubilized in fluoroalcohols produces scaffolds that are essentially akin to gelatin [97]. Dong et al. recently published a study on the electrospinning of collagen from a mixture of phosphate buffered saline (PBS) and ethanol in order to overcome these degradation issues [98]. This study demonstrated that scaffold characteristics were similar between collagen scaffolds electrospun from PBS/ethanol and those electrospun from hexafluoroisopropanol (HFIP) and that the collagen triple helix remained intact when electrospun from PBS/ethanol (verified by Fourier transform infrared spectroscopy (FTIP)) [98].

In summary, our laboratories believe that electrospinning holds great promise. Both self-assembly and phase-separation techniques have been used to produce nanoscale scaffolds. However, electrospinning would appear to be a much simpler, more cost-effective, and highly adaptable fabrication strategy that can be scaled over a wide range of production values, factors critical to commercial and clinical success.

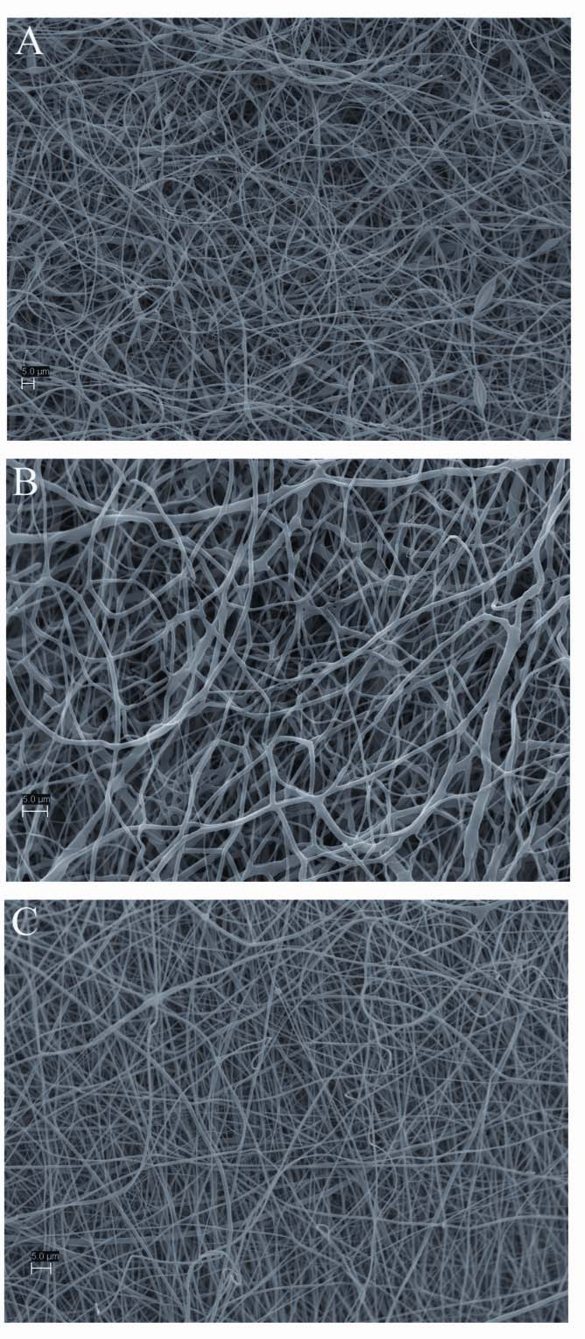

Figure 2.2 A-C. Scanning electron microscope (SEM) images at 2000x magnification of (A) electrospun collagen, average fiber diameter 0.88 ± 0.25 µm, (B) electrospun PDS, average fiber diameter 0.88 ± 0.30 µm and (C) electrospun 50:50 PDS:gelatin blend, average fiber diameter 0.70 ± 0.23 µm. All scaffolds were processed using HFIP.

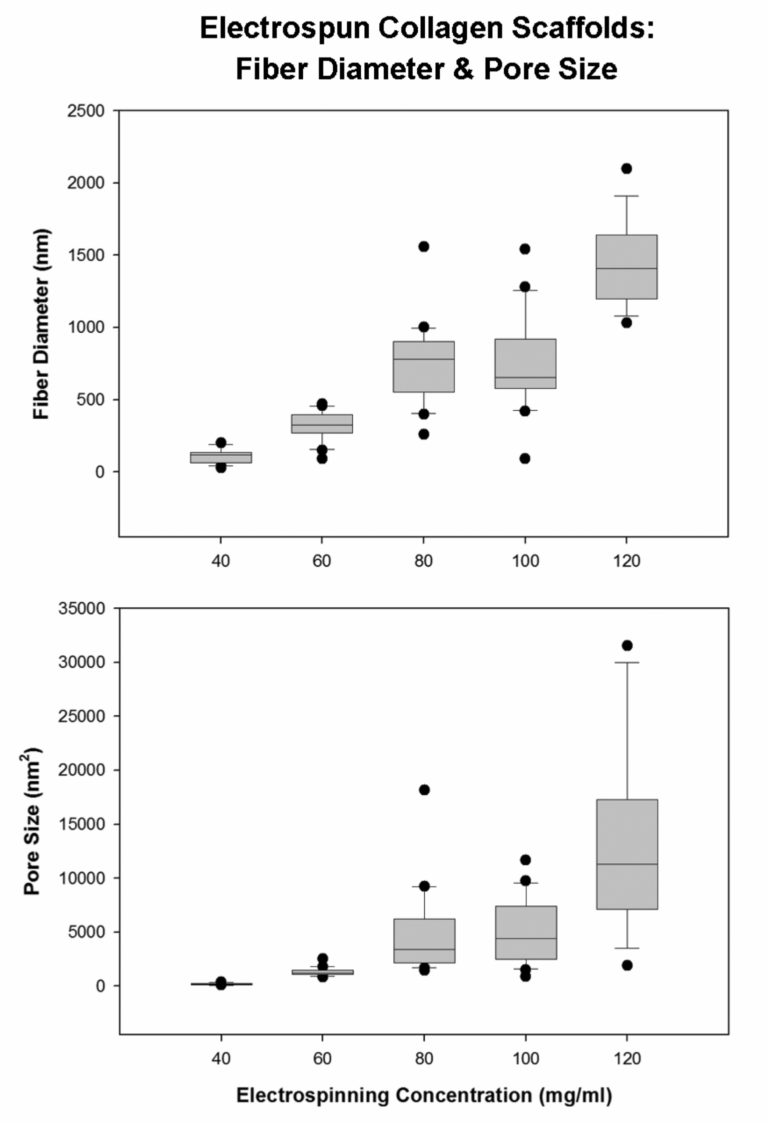

Figure 2.3. Plots illustrating the relationship between fiber diameter (top) or pore size (bottom) and starting concentration in electrospun collagen scaffolds.

SCAFFOLD ADVANCEMENTS

It is theoretically possible to extract and recover constituents of the native ECM and subsequently electrospin this highly heterogeneous blend of proteins into a scaffold. Superficially, this approach would appear to have merit; reconstituting the chemical composition of the native ECM using a whole tissue extract appears to offer a straightforward answer to a difficult problem. However there are several considerations that argue against this strategy. Notably, the clinical use of a material composed of such a complex mixture of proteins and antigenic determinants can be expected to aggravate wound healing by inducing a pronounced inflammatory response. The dynamics of electrospinning complex mixtures of proteins has not been explored to any great extent. It is clearly possible, and very likely, that novel polymers composed of proteins that do not normally co-assemble in vivo will group together within the electrospinning jet. “Multi-polymeric fibers” produced in this fashion may exhibit unique functional properties, but the risks of adverse immune reactions would appear to obviate the use of this type of material, even if it is prepared from an autologous source. It seems more likely that a more “minimalist” approach will dominate in the design of scaffolds. The next generation of scaffolds may well function as templates that can be used to control cellular phenotype yet contain the information necessary to “program” the local cell population to remodel the microenvironment into the appropriate composition.

Variable Scaffold Composition. Materials native to the ECM are a natural choice for use in scaffolds. The rapid infiltration of cells into electrospun collagen scaffolds suggest that producing scaffolds composed of materials already found in the ECM and fibrils that approach the diameter of native fibrils imparts unique biological properties to the scaffolds [42]. Collagen is the most abundant protein in mammals and acts as the major structural protein in skin, bones and tendons. Thermal denaturation of the collagen protein produces gelatin; this denaturation breaks the collagen triple helix into random coils, reducing the mechanical properties of the protein [15]. Experiments conducted in our laboratory indicate that implanted gelatin scaffolds appear to induce significant inflammation and retard cell penetration. Conversely, implanted collagen scaffolds appear to cause minimal inflammation and promote cell penetration (Figure 2.4). However, matrix synthesis and degradation, as well as cellular differentiation, appear to occur more readily with dermal fibroblasts plated onto gelatin scaffolds versus collagen scaffolds [67]. These results may be indicative of some of the design oversights of earlier generations of scaffolds. In terms of timing, scientists often focus on the provisional matrix; an "immature" scaffold found in the early stages of wound healing and predominantly composed of fibrin, fibronectin and hyaluronic acid. However, scaffolds are often composed of materials, such as collagen, that represent a "mature" matrix and, on a cellular level, may indicate an already remodeled would bed. The possible problem in this scenario is the placement of a "mature" matrix in an environment primed to respond to an "immature" matrix; which may explain why a number of cellular processes crucial to wound healing appear to occur more readily on scaffolds composed of gelatin [67]. Generally, the constituents and signals in the scaffold environment must adapt and continue the wound healing process to reflect the material in place. It is possible that an appropriate scaffold template could simply initiate a series of events that would eventually result in the total integration of the scaffold.

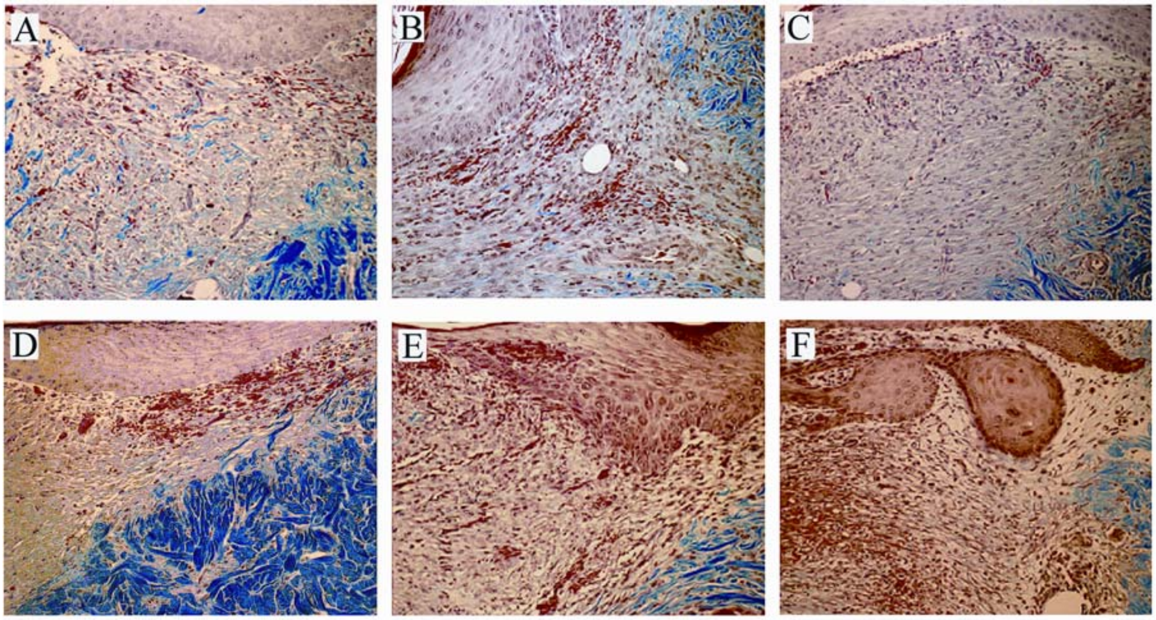

Figure 2.4 A-F. Trichome stained fibers of dermal tissue recovered from full thickness dermal wounds prepared on guinea pigs and implanted with electrospun collagen or gelatin scaffolds. In these experiments, cross-linked (0.5% gluteraldehyde/ethanol) electrospun type I collagen and gelatin scaffolds (approximately 150-250 µm thick and of varying fiber and pore size) were immersed in an antibiotic solution, covered with a silver impregnated dressing (to suppress bacterial growth) and sutured onto the dorsum of guinea pigs. Tissue samples were recovered for histological evaluation after 7 days. Each image was taken at the margin of the injury site, with healthy tissue to the right (mature, intact endogenous tissue is stained blue). Dermal wound implanted with electrospun type I collagen, (A) average fiber diameter 280 nm, average pore size 500 nm^2, (B) average fiber diameter 670 nm, average pore size 3720 nm^2 and (C) average fiber diameter 1000 nm, average pore size 3550 nm^2. Dermal wound implanted with electrospun gelatin, (D) average fiber diameter 240 nm, average pore size 440 nm^2, (E) average fiber diameter 470 nm, average pore size 1340 nm^2 and (F) average fiber diameter 660 nm, average pore size 5280 nm^2. After 7 days, the collagen implants appeared to be infiltrated with cells and had minimal inflammation; the gelatin implants were not highly penetrated and had a large magnitude of inflammation.

The wide range of both natural and synthetic materials that can be utilized in electrospinning represents a substantial advantage to this technique. While natural polymers already contain the binding sites and signaling capabilities needed by cells (a quality markedly absent in synthetic polymers) there are some limitations to natural polymers, including issues with immunogenicity, degradation, reproducibility and poor material properties (Figure 2.5) [41][66]. While the molecular structure of synthetic polymers (e.g. PLA, PGA) does not mimic the ECM, this class of materials has been highly researched, in part because of the capability to engineer scaffold material properties to enhance cell function. Material properties represent a critical structural variable in the design of scaffolds; in wound healing, material properties (specifically stiffness) have been implicated in the modulation of cellular phenotype, wound/cellular contraction and matrix remodeling (Figure 2.6) [68]. Product specifications targeted to bone reconstruction often require material properties that reach beyond what most natural materials can provide. For example, Lu et al. fabricated an electrospun scaffold composed of bioactive glass fibers that demonstrated an elastic modulus close to that of bone [69]. Obviously, the use of and availability to electrospin such a wide range of synthetic materials is an invaluable benefit to using the electrospinning technique.

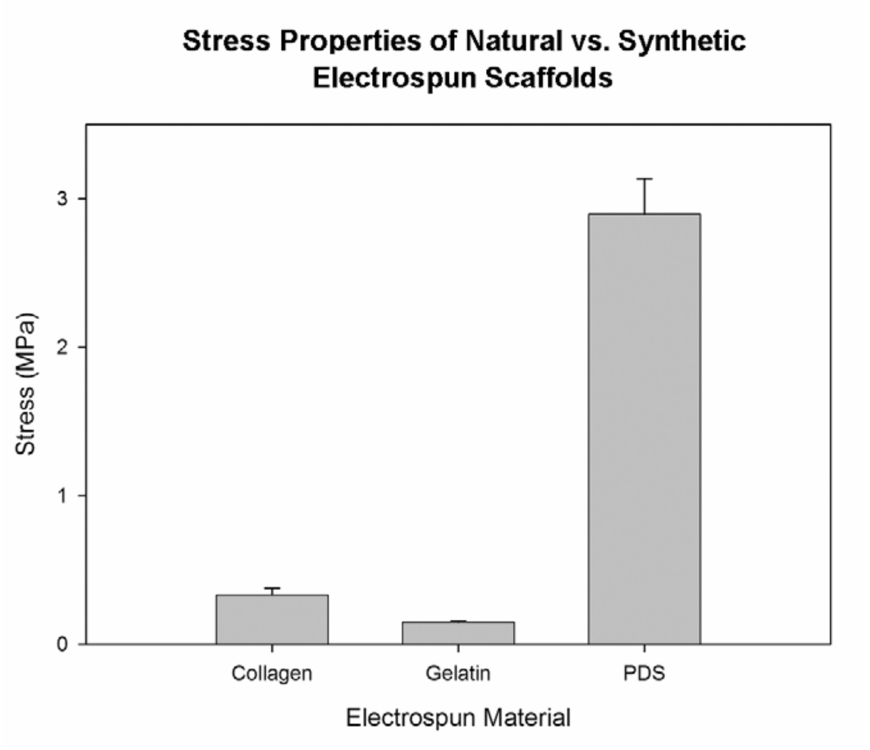

Figure 2.5. Plot illustrating the vast differences in the peak stress properties of natural versus synthetic electrospun scaffolds. Electrospun scaffolds were cut into dumbbell shaped samples using a die punch (2.67 mm wide, gauge length of 0.295 mm) and tested to failure at an extension rate of 10 mm/min. (A) Electrospun collagen, average fiber diameter 0.88 ± 0.25 µm. (B) Electrospun gelatin, average fiber diameter 0.85 ± 0.26 µm. (C) Electrospun PDS, average fiber diameter 0.88 ± 0.30 µm.

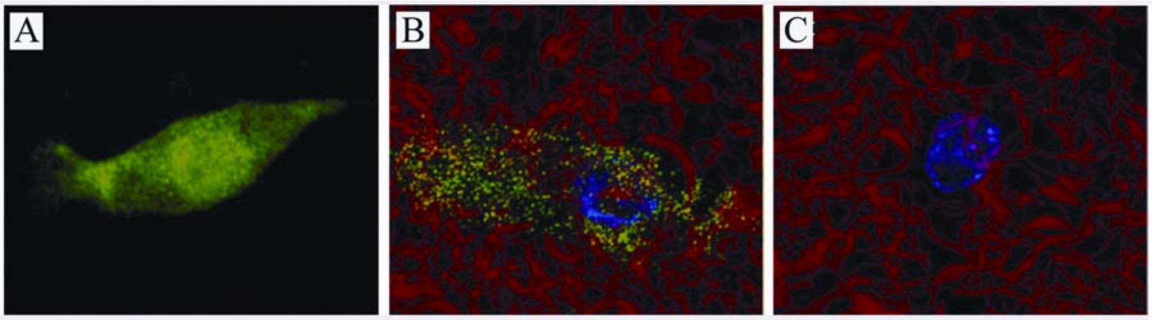

Figure 2.6 A-B. Confocal images of human dermal fibroblasts (HDFs) plated for 24 hr onto electrospun collagen scaffolds (red) cross-linked to varying degrees. (A) Scaffolds with a modulus of < 0.1 MPa (low degree of cross-linking) exhibited small fibrous arrays of α-SMA (green). (B) Scaffolds with a modulus of 0.2-0.3 MPa (medium degree of cross-linking) revealed small α-SMA foci. (C) Scaffolds with a modulus of > 0.3 MPa (high degree of cross-linking) showed no evidence of α-SMA. The presence and nature of the α-SMA in panels A and B indicates a shift to an intermediate proto-myofibroblast phenotype.

Electrospun blends (separate fibers of more than one material within the same scaffold) and/or hybrids (a mixture of more than one material within a single fiber) may be promising for producing a functional scaffold (within the caveats discussed concerning the expression of unexpected antigenic considerations). Electrospun scaffolds composed of highly original blends have been investigated, including such unusual candidates as a keratin/fibroin blend, collagen/silk fibroin hybrid and a zein (a plant protein derived from maize)/hyaluronic blend have been investigated [70-72]. The long-term efficacy of these compositions awaits further study. Additionally, hybrid scaffolds composed of purely synthetic materials, poly(ε-caprolactone) (PCL)/poly(lactide-co-glycolide) (PLGA), have shown promise as biodegradable guidance conduits in transected sciatic nerves [73]. Hybrids and blends of a combination of both natural and synthetic materials also have great potential, possibly creating a scaffold that is both biologically and biomechanically advantageous. Hybrids of collagen/elastin/PCL and gelatin/PCL have demonstrated favorable characteristics that may be valuable for use in cardiovascular tissue engineering, while blends of aligned collagen/PCL fibers may have future use in patients with large skeletal muscle defects [74][75]. Ko et al. has also reported positive results by electrospinning PLA with nano-sized demineralized bone powders (DBPs) [76]. PLA/DBP and PLA scaffolds implanted into rats with skull defects showed a greater amount of newly formed bone in the defect area with the PLA/DBP scaffolds, indicating a potential scaffold for the regeneration of bone tissue [76]. Additionally, electrospun scaffolds have recently been investigated for their potential use in the production of biosensors. Blended bovine serum albumin (BSA) and poly(ethylene oxide) (PEO) was electrospun into nanofibers and stained with fluorescein isothiocyanate (FITC) [77]. The FITC labeled fibers were demonstrated to be pH sensitive and could be used as a subtle pH sensor, possibility monitoring the biological activities of cells.

Multi-layered scaffolds that better mimic the variable nature of the native ECM are also promising for the generation of a functional scaffold. These layering techniques can range from simple acellular sequentially electrospun layers to more complex constructs that contain a variety of materials and cell types. Pham et al. demonstrated the generation of a PCL scaffold composed of multiple layers of nano or microfibers; the objective was to produce a scaffold with both large pores and small fibers [100]. The major concern with sequential layering is the possibility of delamination of the individual layers. Yang et al. produced cell-fiber multilayered structures completely within the electrospinning system [101]. This method involved electrospinning a collagen:PCL mixture onto a collection plate, then seeding with human dermal fibroblasts and/or epidermal keratinocytes (directly within the electrospinning system) and continuing this process until the desired thickness was achieved [101]. While this method would appear to be less susceptible to delamination of layers, concerns do arise regarding the placement of cells within the electrospinning system; namely cell exposure to the electric field and organic solvents used during the electrospinning process.

Coating of electrospun fibers is another method for tailoring the biological and mechanical properties of a construct. This approach lends itself nicely to electrospun scaffolds composed of synthetic fibers; the addition of a natural material on the surface of the synthetic fibers may greatly improve the surface properties of the scaffold, possibly enhancing cell attachment and proliferation. Additionally, any issues concerning degradation and poor material properties for an electrospun scaffold composed of natural materials are resolved. PCL, a frequently used material because of its slow degradation rate and favorable material properties, is often electrospun and coated with natural materials such as collagen and gelatin [41][78-80]. Plasma treatment, overnight soaking in a polymer solution and layer-by-layer self assembly are coating techniques that have demonstrated enhanced attachment, spreading and proliferation of cells cultured on the scaffolds [78-80]. Additionally, in an attempt to create a functional esophagus substitute, Zhu et al. investigated the coating of poly(L-lactide-co-caprolactone) (PLLC) with fibronectin (Fn) via polyester aminolysis then Fn coupling using gluteraldehyde, with encouraging results [81]. Researchers have also taken to coating synthetic electrospun fibers with more complex materials. Using the plasma treatment method, Jia et al. immobilized soluble eggshell membrane protein (SEP) onto electrospun PCL fibers; SEP is the membrane between the egg white and inner egg shell and consists primarily of collagen (types I, V, and X), osteopontin and sialoprotein (proteins important in bone remodeling) [82].

Adjustable Scaffold Architecture. The architecture of the ECM plays a crucial role in the overall function of a tissue and varies from tissue to tissue. It would seem that scaffolds should, at the very least, exhibit the gross structural properties of the tissue that it is designed to reconstruct. Engineered scaffolds must also have pores that allow for cell penetration, capillary in-growth and oxygen delivery/nutrient exchange. The flexibility of the electrospinning process allows for the modification of many characteristics of an electrospun scaffold, i.e. material, fiber alignment, material properties, pore size and fiber size.

Varying the degree of fiber anisotropy (alignment) present in an electrospun scaffold can be used to impart unique material and biological properties to a construct. In conventional electrospinning systems the degree of fiber alignment present in an electrospun scaffold can be controlled through the manipulation of the starting concentrations of polymer present in the electrospinning solutions and/or the speed of mandrel rotation [14]. The whipping motion that develops within the charged jet that is used to produce very small diameter fibers makes it difficult to induce anisotropy in this type of construct. As fiber diameter increases, the inertia of the charged jet dampens this whipping motion making it possible to use a rotating mandrel to collect, and induce, fiber alignment (Figure 2.7). Under ideal conditions the extent of fiber alignment can be modulated by varying the rotational speed of the collecting mandrel (Figure 2.8) [14][63]. In addition, electrospinning systems utilizing a gap method can also produce highly aligned fibers. Klinkhammer et al. demonstrated the use of this method by electrospinning PCL using dual, rectangularly shaped grounded collectors placed approximately 4 cm apart. Highly aligned fibers were collected and suspended in the air between the parallel collector bars [99]. We have examined this relationship using the fast Fourier transform (FFT) to measure and assign specific values of alignment to scaffold fibers; we then systematically conduct materials testing as a function of the degree of alignment [14][63][83]. From a biological standpoint, fiber alignment can be used to provide guidance cues and regulate cell shape. Chow et al. successfully investigated the use of scaffolds composed of highly aligned PDS to guide neurite and astrocyte growth along fibers to stimulate axonal regeneration in injured peripheral and central nervous system environments [84].

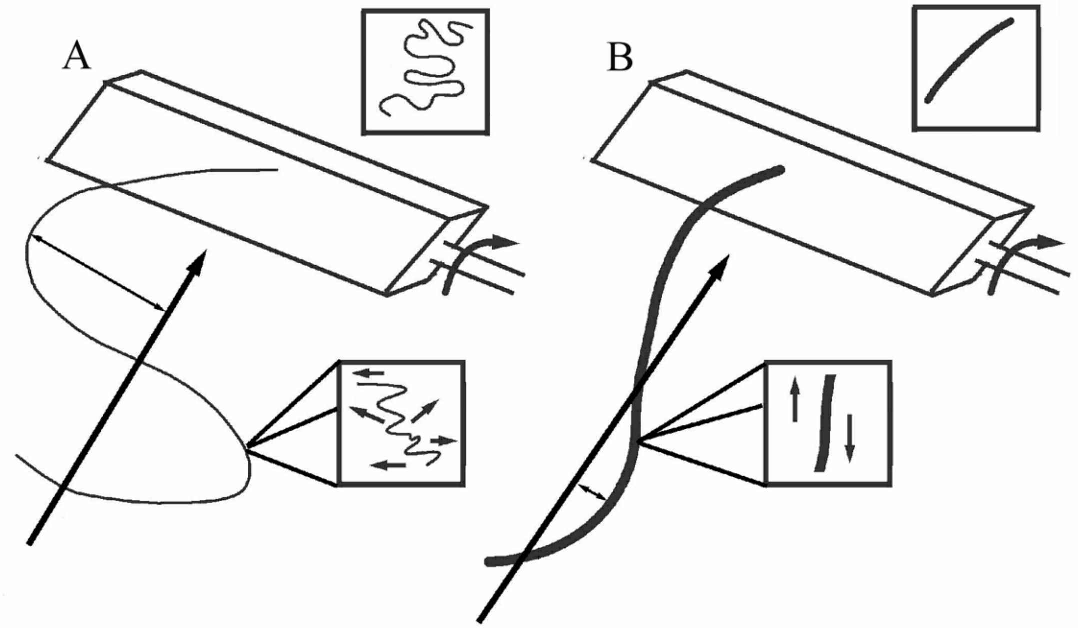

Figure 2.7 A-B. Schematic depicting the motion that develops within the charged jet as it moves across the electrospinning air gap. (A) Smaller fibers exhibit a considerable whipping motion, making it difficult to induce anisotropy. (B) As fiber size increases, the whipping motion dampens, making it possible to create scaffolds composed of aligned fibers.

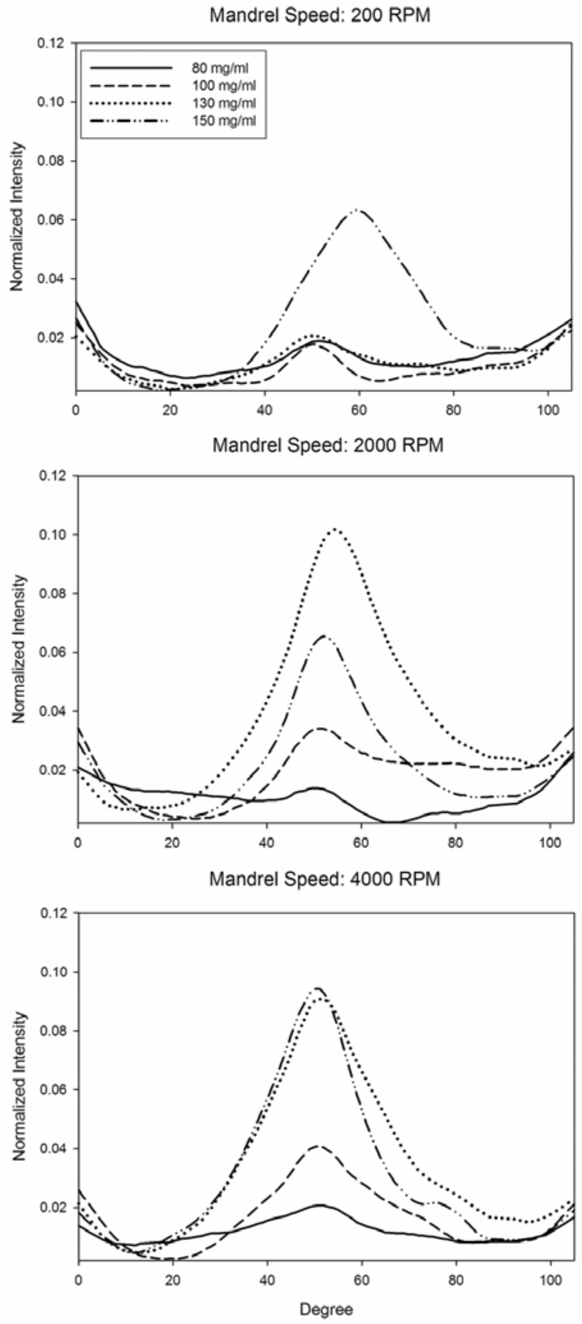

Figure 2.8. FFT analysis of scaffold alignment as a function of mandrel RPM. Various starting concentrations of electrospun gelatin (80, 100, 130, 150 mg/ml) were directed toward a mandrel rotating at 200 (top), 2000 (middle) and 4000 RPM (bottom). The extent of fiber alignment varied by fiber size and can be controlled by changing the rotational speed of the collecting mandrel. A higher peak indicates a larger degree of fiber alignment within a scaffold.

There are nearly endless possibilities regarding the overall shape and size of an electrospun scaffold; these characteristics are controlled by the mandrel used during the electrospinning process and the quantity and placement of fiber deposition. While flat mats are commonly utilized, electrospinning can be used to produce a variety of shapes and configurations; electrospun tubes are explored for their possible use in blood vessels and nerves. Small diameter vascular grafts using electrospun silk fibroin tubes were successful cultured with human endothelial cells and smooth muscle cells and reported burst strength and tensile properties similar to those of native vessels [85]. Aligned electrospun chitosan mesh tubes cultured with schwann cells may represent a functional substitute for autogenous nerve grafts [86]. The control over the quantity and placement of the electrospun fibers onto a mandrel allows for great variance in the overall thickness and shape of a scaffold. Matsuda and Kawahara have investigated the production of flexible catheter tips by electrospinning tubular scaffolds with gradient wall thickness, tube diameter or Young's modulus [87]. Research in the flexibility variation of electrospun scaffolds is applicable to many areas of tissue engineering.

Scaffold fiber and pore size can be adjusted by altering the starting electrospinning solution; in general, fiber diameter and pore size track together (e.g. small fibers and small pores). Traditionally, considerable effort has been expended to examine how average fiber diameter impacts scaffold performance. However, pore size represents an important variable in scaffold design; pore size must be sufficient enough to allow for cell penetration and the formation of blood vessels. HDFs cultured on highly porous PLGA scaffolds showed higher levels of viability and underwent more scaffold migration and infiltration than controls [81]. Pore size can be manipulated independent of fiber size by several methods. Zhu et al. utilized a very slowly rotating frame cylinder with metal struts to increase the overall porosity and individual pore sizes of a scaffold [81]. The frame cylinder mandrel functions to alter the electrostatic forces driving the fibers; high density fibers are driven to deposit onto the metal struts while low density fibers are driven to deposit between the metal struts, producing a highly porous scaffold [81]. Baker et al. increased scaffold porosity by co-electrospinning PCL, a slowly degrading material, and PEO, an aqueous soluble material [96]. The PEO was used as a sacrificial material and removed post-electrospinning by placement in aqueous solution; when cultured with mesenchymal stem cells (MSCs), PCL scaffolds with a large sacrificial PEO component (greater than 40%) showed markedly improved cellular infiltration [96]. The use of doping materials can also be exploited to regulate the pore size of electrospun materials. For example, cryogenic electrospinning uses the simultaneous deposition of ice crystals and electrospun fibers onto a cooled mandrel (the scaffold is immediately freeze dried to remove the ice crystals) to increase pore size. Subcutaneous implant studies conducted in rats detected improved infiltration and vascularization when compared to conventionally prepared electrospun scaffolds [88].

Post electrospinning processing methods also have a direct impact on scaffold performance. Scaffolds composed of natural proteins must be cross-linked to maintain the structural integrity of the construct. Glutaraldehyde solutions or vapors have been commonly used to cross-link protein based scaffolds. The glutaraldehyde cross-linking technique is inexpensive, efficient, cross-links over a variety of distances and reacts with many of the amino groups present in a protein [64]. The extent of cross-linking in an electrospun scaffold is a function of the percentage of glutaraldehyde present in the cross-linking solution. The degree of scaffold cross-linking increases as the percentage of glutaraldehyde present increases but eventually reaches saturation where no more cross-linking can occur (Figure 2.9) [89]. However, there may be some cytotoxity and calcification issues associated with this fixation agent [90]. Other methods of scaffold cross-linking have been developed, including a carbodiimide/ethanol technique. Carbodiimide is a zero-length cross-linker that has shown nominal potential cytotoxity issues and can be used to modulate material properties similar to (and in some instances, better than) glutaraldehyde fixation [64].

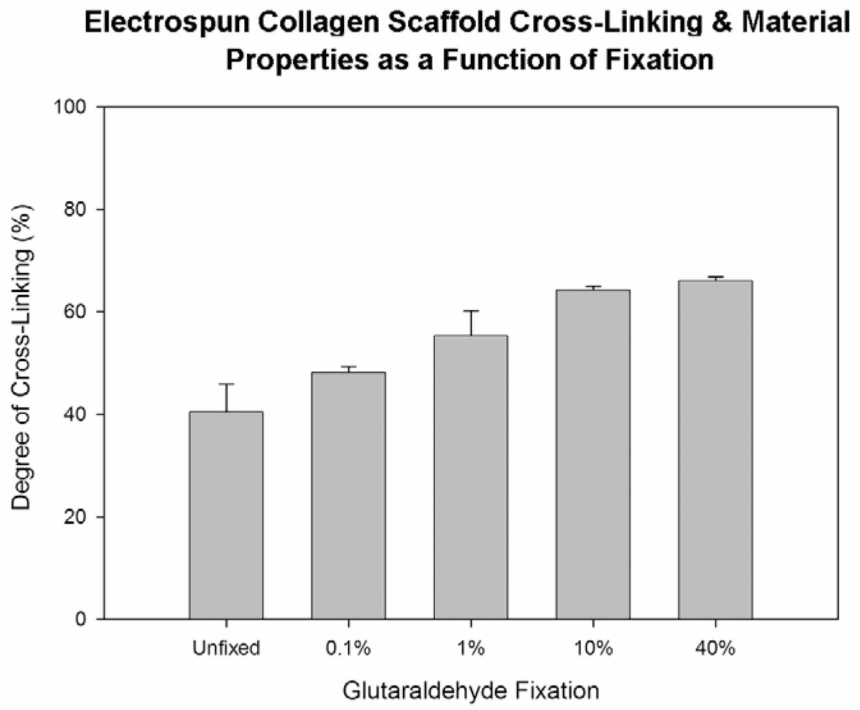

Percent Fixation	Peak Stress (MPa)	Tangential Modulus (MPa)	Strain at Break (%)
Unfixed	0.143 ± 0.020	0.083 ± 0.012	233.4 ± 22.4
0.1%	0.255 ± 0.041	0.262 ± 0.033	168.3 ± 17.8
1 %	0.283 ± 0.026	0.258 ± 0.022	210.0 ± 11.4
10%	0.317 ± 0.031	0.323 ± 0.033	168.9 ± 12.1
40%	0.325 ± 0.033	0.375 ± 0.033	123.3 ± 8.9

Figure 2.9. Plot and table demonstrating electrospun collagen scaffold cross-linking and material properties as a function of glutaraldehyde fixation. The extent of cross-linking increases as a higher volume of glutaraldehyde is present in the cross-linking solution (until saturation is reached).

Scaffold Bio-Techniques. Scaffold performance can also be regulated by the addition of specific factors directly into the electrospinning solution. For example, growth factors, pharmaceuticals and cells can be processed directly into a construct to regulate overall functionality. Successful incorporation of human foreskin fibroblasts and human-adipose derived adult stem cells into electrospun polyvinyl alcohol (PVA) nanofibers (a technique known as "cell electrospinning") was demonstrated by van Aalst et al [91]. Cells were grown to confluence, re-suspended in PBS, solubilized in PVA and electrospun at 20 kV in a chamber with constant CO_2 flow. The collector plate for the cell/PVA solution was a grounded aluminum disk set in a polycarbonate container filled with PBS. Post electrospinning assays demonstrated that cells incorporated into the PVA nanofibers upheld viability, proliferation and function [91]. Growth factors can also be incorporated into electrospun scaffolds by adding them directly to the pre-electrospinning solution. Research by Fu et al. involving the incorporation of bone morphogenetic protein-2 (BMP-2) into hydroxylapatite (Hap)/PLGA nanofibers demonstrated maintained BMP-2 biological activity in vitro and in vivo; furthermore, scaffolds containing encapsulated BMP-2 showed improved bone healing potential [92]. Electrospun scaffolds intended for chemotherapy have also been investigated; in vivo studies with PLGA electrospun nanofibers loaded with paclitaxel (a pharmaceutical used in cancer chemotherapy) showed sustained released and improved tumor inhibition [93]. Additionally, a two stream electrospinning set-up of poly(ester urethane) urea (PEUU) and PLGA dosed with tetracycline hydrochloride (tet) has been investigated and demonstrated strong and viable antibacterial activity when implanted in vivo [94]. Rate of release is also being investigated; Maretschek et al. have developed a technique to control protein release profiles using electrospun blends of PLLA and hydrophilic polymers [95]. However, there is a potential problem when incorporating pharmaceuticals (and growth factors and other peptides) into electrospun scaffolds: solvent induced-damage to the factors that have been processed directly into the fibers. To circumvent this issue, we have developed a method to trap our active agents into nano-to-micron scale alginate beads and process those supplemented beads directly into our electrospun scaffolds, sequestering the incorporated agents away from any potential effects of the solvent (Figure 2.10).

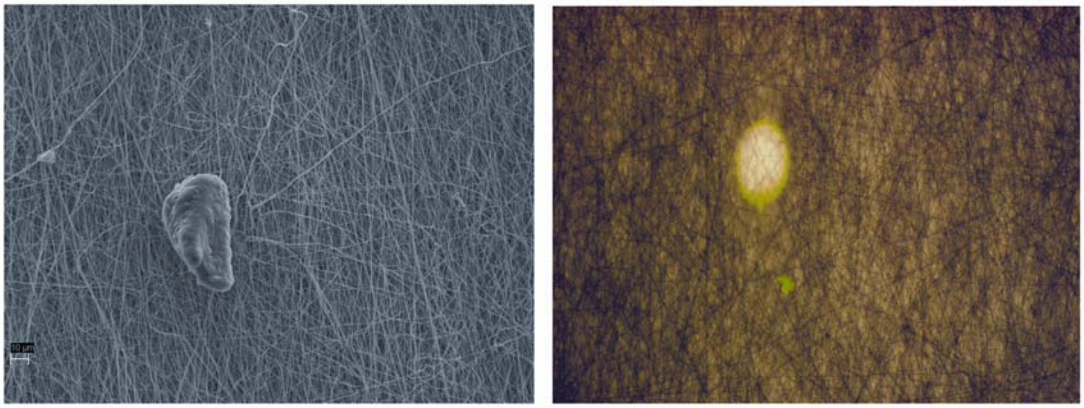

Figure 2.10. Images demonstrating the presence of alginate beads within an electrospun PDS scaffold. (Left) SEM image at 2000x magnification. (Right) Brightfield image with FITC labeled antibodies (green) trapped within the alginate bead.

CONCLUSION

In order to be clinically relevant, scaffolds must mimic critical elements of the native ECM. Defining the nature of these elements remains an active component of the research endeavor. Fundamentally, scaffolds must provide the structural integrity necessary to support normal cell function and interaction in three-dimensional space. While self-assembly and phase separation are excellent nanofiber production techniques, the ease and versatility of the electrospinning process allows for the fabrication of scaffolds composed of a variety of materials in a wide range of shapes and sizes. Continued innovation in the electrospinning field has shown promise and progress towards the development of functionally relevant scaffolds. Electrospun scaffolds composed of both natural and synthetic materials (either electrospun as a blend or hybrid or coated post-electrospinning) that work together to provide structural integrity while also providing the biological cues needed by cells represents a particularly attractive avenue of research. Progress regarding scaffold composition, in conjunction with the continued development of methods designed to control the gross and more subtle aspects of scaffold architecture and function, should yield insights into the processes that regulate normal tissue hemostasis. Finally, the successful addition of cells, pharmaceuticals and growth factors into scaffolds is creating an even more versatile nanofiber material. Research in tissue engineering will likely continue to characterize the immense structural and molecular distinctions of the native ECM and use this information to fabricate custom scaffolds according to their placement and function.

CHAPTER 3 Measuring Fiber Alignment Using the Fast Fourier Transform

Preface: The following manuscript appeared in the Journal of Biomaterials Science, Polymer Edition, 2007, volume 19, pages 603-621 [83]. The work included is intended to be a detailed guide to clarify the theory and practice of using the fast Fourier transform to measure scaffold fiber alignment. Additionally, various imaging and filtering modalities were examined in order to expand the use of this powerful characterization tool.

Measuring Fiber Alignment in Electrospun Scaffolds: a User's Guide to the 2D Fast Fourier Transform Approach

CE Ayres[1], BS Jha[2], H Meredith[2], JR Bowman[2], GL Bowlin[1], SC Henderson[2] and DG Simpson[2]

[1]Department of Biomedical Engineering
Virginia Commonwealth University
Richmond, VA 23284

[2]Department of Anatomy and Neurobiology
Virginia Commonwealth University
Richmond, VA 23298

ABSTRACT

In this study we describe how to use a two dimensional fast Fourier transform (2D FFT) to measure fiber alignment in electrospun materials. This image processing function can be coupled with a variety of imaging modalities to assign an objective numerical value to scaffold anisotropy. A data image of an electrospun scaffold is composed of pixels that depict the spatial organization of the constituent fibers. The 2D FFT function converts this spatial information into a mathematically defined frequency domain that maps the rate at which pixel intensities change across the original data image. This output image also contains quantitative information concerning the orientation of objects in a data image. We discuss the theory and practice of using the frequency plot of the 2D FFT function to measure relative scaffold anisotropy and identify the principal axis of fiber orientation. We note that specific degrees of scaffold anisotropy may represent a critical design feature in the fabrication of tissues that will be subjected to well-defined uniaxial mechanical loads. This structural property may also represent a source of guidance cues that can be exploited to regulate cell phenotype.

INTRODUCTION

Electrospinning technology shows great potential as a gateway to the development of physiologically relevant tissue engineering scaffolds [66]. This nonmechanical process has been used to fabricate natural protein polymers [13][61][62], biocompatible synthetic polymers [105][106] and blends of natural and synthetic polymers [15][43] into tissue-engineering scaffolds composed of nano-to-micrometer diameter fibers. The non-woven nature of the electrospun scaffold results in a tissue-engineering platform with a large surface area and highly interconnected pore spaces [107]. This architecture mimics the organization of the native extracellular matrix and can be tailored to selectively support a wide variety of cell types.

The elaborate and interconnected network of the native extracellular matrix exhibits varying degrees of anisotropy. The recapitulation of this structural feature may represent a critical design feature in the fabrication of tissue-engineered tendons, ligaments, blood vessels, and other organs that may be subjected to uniaxial mechanical loads. This is especially true in light of growing evidence that fiber alignment and overall scaffold anisotropy play central roles in defining the material properties of electrospun materials [14][63][108]. Anisotropic properties can also be expected to represent a source of guidance cues that can be exploited to regulate cell phenotype, cell migration, and the distribution of cells within an engineered tissue [45][84]. Our goal is to develop noninvasive techniques that can be used to objectively measure fiber alignment and overall scaffold anisotropy.

Morphological techniques and destructive materials testing strategies have been used to illustrate and detect anisotropy in electrospun materials. For example, we, and other authors, have used representative scanning electron micrographs to demonstrate fiber alignment in scaffolds prepared from various electrospun polymers [13][106][109][110]. This approach lacks precision and is obviously highly subjective. Materials testing can be used to detect directional bias and evidence of scaffold anisotropy [106]. However, without an objective measurement of fiber alignment, it is difficult, at best, to determine how specific degrees of anisotropy might contribute to the biological, and mechanical, performance of a given scaffold.

Optical techniques, that are non-destructive, such as laser scattering, have been used to evaluate fiber orientation in valve leaflets [111][112]. This elegant technique can resolve information to the level of individual fibers; however, it requires intensive data analysis to extract the descriptive parameters necessary to map the large-scale structural properties of a fibrous construct. Derivatives of Fourier transforms have long been used to measure the geometric composition of data images [113][114] and, to a lesser extent, have been applied to the analysis of biological systems. For example, these algorithms have been used to evaluate the impact of specific genetic manipulations on cardiac cytoarchitecture and myofibrillar organization [115]. In limited applications of this technique, electrospun scaffolds have been processed for scanning electron microscopy and subjected to a custom image analysis strategy designed to track and map fiber distribution [108]. Unfortunately, this approach limits data acquisition to surface features and the sample is lost to the analysis. In this review, we describe how a two dimensional fast Fourier transform (2D FFT), readily available in a number of programs designed for image analysis, can be coupled with a variety of optical imaging modalities to rapidly measure scaffold anisotropy [14][63].

MATERIALS AND METHODS

Electrospinning. Reagents were purchased from Sigma Aldrich (St. Louis, MO) unless noted. Gelatin was suspended at various concentrations (100, 120, 150 or 180 mg/mL) and agitated in 2,2,2 trifluoroethanol (TFE) for 24 hr [14][15][63]. Electrospinning suspensions were loaded into a 20 mL Becton Dickinson syringe capped with an 18 gauge blunt tipped needle. The air gap distance between the source suspension and the grounded target mandrel was set to 20 cm. A Harvard perfusion pump was used to meter the delivery of the electrospinning suspensions to the electric field; an accelerating voltage of 25 kV was used for all samples. The positive output lead of a high voltage power supply (Spellman CZE1000R; Spellman High Voltage Electronics Corporation) was attached by an alligator clip to the blunt tipped needle. A stainless steel rectangular (70 mm x 10 mm x 5 mm) mandrel designed to rotate from 0-6000 RPM was used as the grounded target. A digital stroboscope (Shimpo Instruments DT3-11A) was used to continuously monitor the target RPM. Samples were stored in a desiccation chamber to limit hydration prior to analysis.

Scanning Electron Microscopy. Dry, unfixed electrospun samples were sputter-coated for conventional scanning electron microscopy (SEM, Zeiss EVO 50 XVP). SEM images are amenable to 2D FFT analysis; however, data is restricted to the superficial surfaces of the specimen. Refer to the text for a discussion of the technical issues encountered when using this imaging modality.

Light Microscopy. Scaffolds were imaged with a Nikon TE300 microscope equipped with a Nikon DXM 1200 digital camera. Images were captured using a 20x 0.40 n.a brightfield objective and stored as uncompressed .TIF files with an image dimension of 3840 x 3072 pixels. The theoretical lateral resolution of the 20x lens used in this study is 0.838 µm; the average fiber diameter of the scaffolds presented in this study is greater than 0.8 µm. For routine 2D FFT analysis of scaffold structure, objective resolving power is matched to average fiber diameter. If an objective with inadequate resolving power is used to capture data sets, individual fibers are not detected and the resulting image is composed largely of optical noise. In general, this type of optical image/data set is unsuitable for analysis. We note, however, that under some circumstances the birefringence generated by sub-resolution fibers can be used to generate alignment data (see reference 14 for example). In this type of data set, image alignment values should be interpreted with caution and an external measure of alignment (for example materials testing) should be used to calibrate the reported 2D FFT values derived under these conditions. While the selected objective should have sufficient resolving power to image individual fibers, we attempt to keep objective magnification to a minimum. As objective magnification is increased, the total amount of surface area that is available for image capture is reduced. We believe that measurements of scaffold anisotropy should be averaged over as large as an area as possible. Local variations in fiber alignment can bias the 2D FFT process. If necessary, alignment data can be captured from several sites in a scaffold and averaged to circumvent the limitations inherent when a small sample surface area must be used to generate an alignment value.

Model Scaffold. Thin spaghetti (Mueller's, American Pasta Company, USA) was used to fabricate "model" scaffolds and to demonstrate how the 2D FFT generates and encodes alignment data. This material is easy to manipulate and allows for a variety of parameters to be explored. The thin spaghetti was arrayed in an uncooked or cooked (al dente, 5 minutes) state onto a flatbed scanner. Images were captured at 2048 x 2048 pixels and stored as grayscale .TIF files.

Confocal Laser Scanning Microscopy. A Leica TCS-SP2 AOBS confocal laser scanning microscope was used to capture images of electrospun scaffolds. The pinhole was optimized for all images to 1 Airy disk unit. The 514 nm laser line was used to illuminate the samples; images were captured at a scan resolution of 2048 x 2048 pixels in reflectance mode. Representative cross-sections in the confocal data sets were calculated and projected along the X and Y orientations (i.e. XZ and YZ digital slices). Electrospun samples were imaged with a 20x (0.70 n.a.) dry objective lens. Total surface area measured was 750 x 750 µm. The Voxel dimensions for this image are 0.36 x 0.36 x 0.36 µm. Confocal three dimensional data sets were compiled as an average intensity data image and processed by 2D FFT. Alignment analysis of confocal images is sensitive to the method used to compile a two dimensional projection of a three dimensional data set. We prefer to use an average projection in this type of analysis. While maximal projections can be used, average projections should only be compared to average projections and maximal projections should only be compared to maximal projections in 2D FFT analysis.

Demonstration of Scaffold Response to Strain. Scaffold response to uniaxial stretch was characterized using a custom-fabricated stretching device. The instrument was modeled after a device used in previously published studies to examine cellular response to static loads [45]. The device resembles the original design but was remanufactured from aluminum to lend additional stiffness to the stretching platform.

Stretch was applied by a set of calibrated thumbscrews that displace a set of specimen clamps a known distance. The stretching device was threaded to the stage of a Nikon TE 300 microscope. Dumbbell shaped samples (2.67 mm wide with a gauge length of 7.49 mm) of electrospun scaffolds were mounted in the testing apparatus and held directly over the objective light path. A given area was repeatedly photographed as calibrated degrees of stretch (5, 15, and 25%) were placed across the sample.

2D Fast Fourier Transform. A more detailed description of the 2D FFT approach for measuring scaffold anisotropy is presented in the results section of this manuscript. All images were stored and analyzed as uncompressed .TIF files to preserve image integrity; the image compression used in .JPG format will degrade image integrity and should not be used for archival storage. Grayscale 8-bit images were cropped to 2048 x 2048 pixels for analysis. ImageJ software (NIH, http://rsb.info.nih.gov/ij) supported by an oval profile plug-in (authored by William O’Connell) was used to conduct 2D FFT analysis. All alignment data was normalized to a baseline value of 0 and plotted in arbitrary units ranging from 0 to approximately 0.15.

Angle information concerning the principle direction of fiber alignment must be calibrated to the specific version of the NIH ImageJ software and oval profile plug-in used for analysis. Convention places the 0° position (Figure 3.1 B) at 3:00 o'clock on the unit circle and continues in a counterclockwise fashion with 90° at 12:00 o'clock, 180° at 9:00 o'clock and 270° at 6:00 o'clock. Some versions of ImageJ (1.36b) altered this convention and 0° was placed at 9:00 o'clock and continued in a clockwise fashion. Minor corrections were incorporated into our analysis to correct for this condition, but may not be necessary for all 2D FFT programs.

To produce the window mask (Figure 3.3 K), scaffold images were imported into and cropped using Adobe Photoshop (Adobe Systems, Inc.). The window mask should be constructed with a gradation of grayscale pixels (darkest at the periphery, lightest at the inner ring). Scaffold images were cut with the elliptical marquee tool into circular samples and the edges were set to feather by 20-25 pixels. These circular data images were then placed onto a grayscale window and flattened prior to 2D FFT analysis.

Materials Testing. Following 2D FFT analysis, samples were subjected to materials testing using a Bionix 200 Mechanical Testing Systems instrument equipped with a 50 N load cell (MTS Systems Corp, Eden Prairie, MN). Samples were cut into a series of dumbbell shaped samples (2.67 mm wide with a gauge length of 7.49 mm). Specimen thickness was determined with a Mitutoyo IP54 digital micrometer (Mitutoyo American Corp; Aurora, IL). Scaffolds were tested to failure using an extension rate of 10 mm/min to evaluate the stress, strain and modulus of elasticity [14][63].

RESULTS

Overview. The 2D FFT function converts spatial information in an optical data image into a mathematically defined frequency domain. This frequency domain maps the rate at which pixel intensities change in the spatial domain. Figure 3.1 provides an overview of how the output of this process is used to measure fiber alignment. A subjective evaluation of the depicted brightfield images (Figure 3.1 A, D and G) indicates that each scaffold is composed of fibers with varying degrees of alignment.

For analysis, grayscale brightfield microscopic images were captured and converted to an integer power of 2 pixel dimensions (256 x 256, 512 x 512, 1024 x 1024, etc.). If images have been captured in color they must be converted to grayscale for 2D FFT analysis. Care should be taken at the time of image capture to optimize sample illumination; uneven illumination can complicate and introduce error into the alignment analysis (see discussion in normalization section of this document).

Processing a brightfield data image by 2D FFT produces a frequency plot, or power spectrum. This plot is composed of grayscale pixels that are distributed into a pattern that can be used to measure the degree of fiber alignment present in an original data image (Figure 3.1 B, E and H). The frequency plot produced by NIH ImageJ software places low frequency pixels at the origin, or center, of the frequency plot (note: selected iterations of the FFT function invert this convention and place low frequency pixels at the image periphery). Low frequency signals correspond to domains within the original microscopy image that contain pixels of similar values, adjacent pixels do not vary to a great extent in intensity. The bulk of this information originates with the background and the overall shape of the image. High frequency pixels are placed away from the origin and toward the periphery of the frequency plot. This information corresponds to spatial domains that exhibit abrupt changes in pixel intensity. Edges, details and noise in the data image all contribute to the generation of high frequency pixels.

When an image of random fibers is processed by 2D FFT, the resulting frequency plot contains a cluster of white pixels that are concentrated in a symmetrical, circular pattern around the origin (Figure 3.1 B). At this point in the process we rotate the frequency plot 90° (the direction is irrelevant) to correct for the inherent rotation of the data that is induced by 2D FFT analysis. A circular projection is placed on the frequency plot (using the ImageJ circular marquee tool). Using the ImageJ oval profile plug-in the pixel intensities are then summed along the radius for each angle of the circular projection (0 to 360°; see Figure 3.1 B for an example of a circular projection and a single radius). The summed pixel intensities for each radius are then plotted against the corresponding angle of acquisition (position of the radial projection on the circular projection) to produce a 2D FFT alignment plot (Figure 3.1 C). Typically, the data from this analysis is reported for 0 to 180°; the frequency plot is symmetric so a complete summation from 0 to 360° is not technically necessary. The images and plots in figure 3.1 demonstrate this symmetrical property of the 2D FFT process.

The 2D FFT alignment plot of a random matrix will exhibit 4 peaks that occur every 90°. Peaks of nearly uniform height are a hallmark of a scaffold composed of random elements. These peaks reflect low frequency spatial information and edge artifacts. An analysis of the scaffold composed of random fibers illustrated in figure 3.1 A generates a peak 2D FFT alignment value of 0.038 units. For a gelatin-based scaffold with this alignment value, there will be no evidence of directional bias during destructive materials testing; average stress and strain at failure will be similar regardless of the direction that a test load is placed across this type of sample [63]. When brightfield data images are processed by 2D FFT, evidence of directional bias in materials testing develops at an alignment value of approximately 0.05 units [14][63].

If a data image containing aligned fibers is processed by 2D FFT, the resulting frequency plot contains pixels that are concentrated along a specific axis (Figures 3.1 D, E, G and H). An examination of this type of frequency plot prior to rotation reveals that the high frequency pixels that report alignment will be preferentially arrayed 90° with respect to the principle angle of fiber orientation. By rotating the frequency plot 90° prior to the radial summation step, the principle angle of fiber orientation can be directly obtained from the alignment plot (e.g. Figure 3.1 F and I). During radial summation the preferentially arrayed pixels act to increase the summed pixel intensity value along a defined axis, producing a prominent peak in the 2D FFT alignment plot. The 2D FFT alignment plots generated from sample scaffolds containing aligned elements exhibit asymmetrical peaks, two larger peaks at 90 and 270° and two smaller peaks at 0 and 360° (Figure 3.1 F and I). The degree of alignment present in the original data image is reflected by the height and overall shape of the most prominent peaks present in the alignment plot. A high and narrow peak indicates a more uniform degree of fiber alignment, a broad peak, or a shoulder on the peak indicates that more than one axis of alignment may be present. The principal axis of fiber alignment is determined by the position of the alignment peaks, in the illustrated examples (Figure 3.1, F and I) the principle axis of alignment is in the vertical direction in the processed image.

Specific degrees of alignment can be correlated with the onset of distinctive material properties. These material properties develop largely independent of fiber diameter [63]. When processing a brightfield data image by 2D FFT we observe the onset of anisotropic properties in an electrospun scaffold of gelatin at a threshold alignment value of 0.05 units. For example, the stress at failure for a random scaffold (Figure 3.1 C) of electrospun gelatin (2D FFT alignment value <0.05 units) is approximately 0.5 MPa in all directions. Once alignment values of 0.05 units are detected this type of scaffold, stress at failure will increase incrementally as a function of approximately 0.01 2D FFT alignment units. In a moderately aligned scaffold (similar to Figure 3.1 D) with a 2D FFT alignment value of 0.05 to 0.06 units the stress at failure increases to 0.75 MPa in parallel with the principle axis of fiber orientation. At 2D FFT alignment values of 0.06 to 0.07 units, stress at failure is approximately 1.0 MPa and, at alignment values of 0.07 to 0.08 units, stress at failure increases to 1.5 MPA when the test load is applied in parallel with the principle axis of fiber orientation [63].

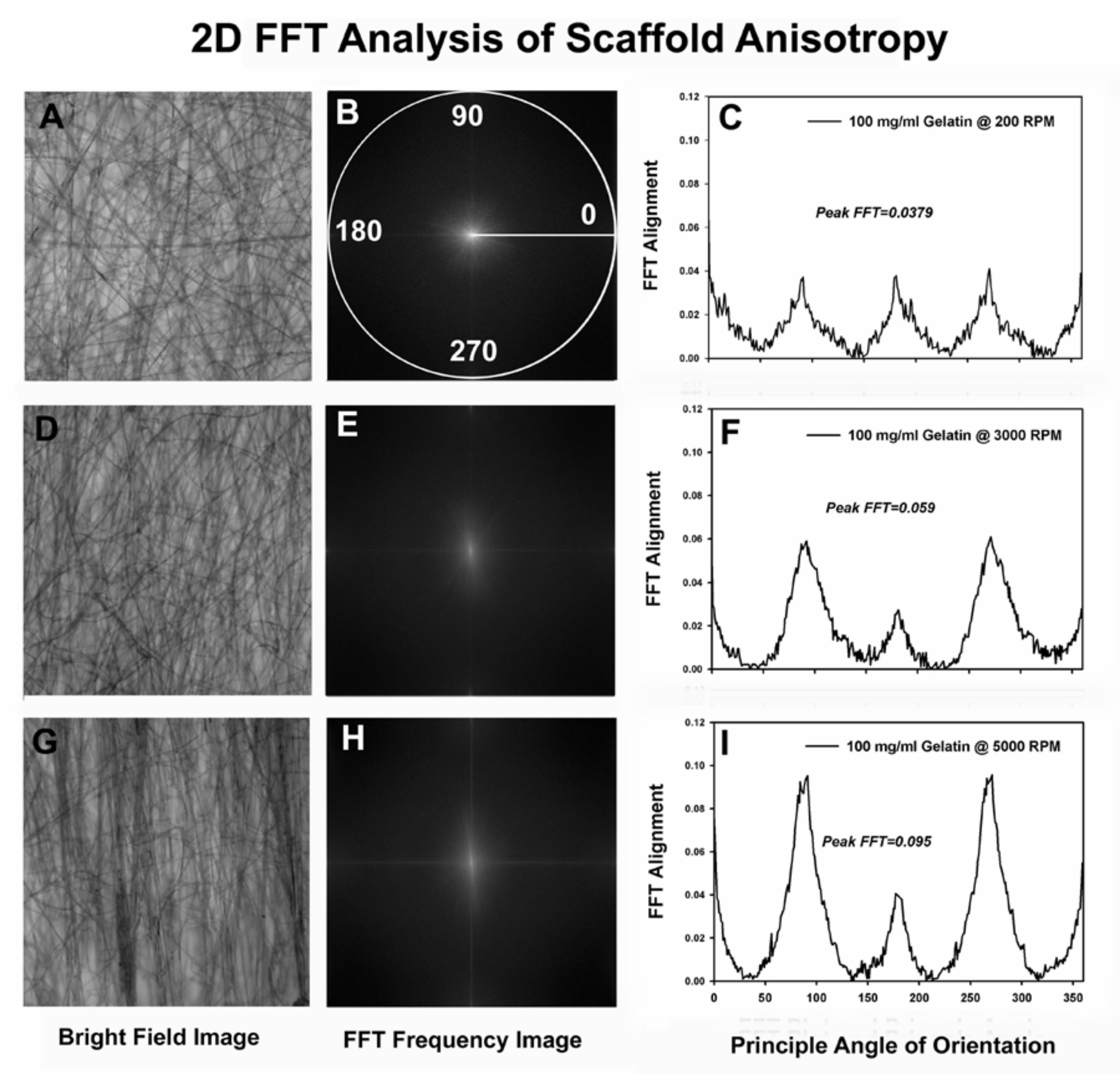

Figure 3.1 A-I. 2D FFT analysis of scaffold anisotropy. Bright field images of representative electrospun scaffolds (A,D,G). ImageJ frequency plots (B,E,H) and 2D FFT alignment plots (C,F,I) for the corresponding bright field images. Note that peak shape and height in the 2D FFT alignment plot report the relative degree of alignment present while the peak position reports the principal axis of orientation for the fiber field.

Normalization and Edge Noise. Normalization is necessary to account for differences in sample thickness, camera performance, operator preference for contrast/brightness, and other variables that impact sample illumination at the time of image capture. The end result of this process is to place data generated from a variety of images onto a common scale. Figure 3.2 illustrates and provides a validation of the normalization process. The raw 2D FFT alignment plots generated from a series of 5 brightfield microscopic images of a single sample are depicted in figure 3.2 A. Each image contained the same field of fibers but was captured at varying light intensities. The shape of the data trace for each alignment plot is similar in nature; however, the summed pixel intensity values generated from the radial summation step varies considerably for each image. Images taken with greater light intensity at image capture have, on average, higher pixel values and are displaced upwards on the Y axis. Figure 3.2 B illustrates this same set of data after normalization; the 2D FFT alignment plots for the images overlap and report a common 2D FFT alignment value (approximately 0.06 units at 90°). These results indicate that the 2D FFT approach can be applied to images captured over a wide range of conditions. However, note as light intensity increases, the relative amount of optical noise present in a brightfield microscopic image also will increase. Detector noise functions in an inverse fashion. As light intensity is decreased and detector gain is increased to generate an image, electronic noise begins to be incorporated into the data set. Noise from either source (optical and/or electronic) can introduce artifacts into a data image and adversely impact the 2D FFT process.

Under ideal conditions, normalization will place each of the four baseline values of the 2D FFT alignment plot in contact with X axis (compare Figure 3.2 A before normalization with Figure 3.2 B after normalization). If the normalization factor is too large, the calculated alignment value will be underreported (because the baseline values of the alignment plot are displaced below the X axis). Conversely, if the factor is not large enough, the alignment value will be exaggerated (because the plot is displaced upward on the Y axis like the plots illustrated in figure 3.2 A).

Figure 3.2 C provides an example of normalization. Columns A and B represent the radial summation data as exported from ImageJ into an Excel spreadsheet (for brevity only the first 130° of data are displayed, the complete set will contain 360° of data). A candidate normalization factor can often be selected by copying the original radial summation data set (Figure 3.2 C, column B) into a new column and sorting this duplicate column in ascending order (Figure 3.2 C, column F). In the illustrated example, the pixel intensity value that resides in the 12th position of the sorted pixel intensity column was selected as the normalization factor (Figure 3.2 C column F: 106666.26). Once a candidate normalizing factor has been chosen, the pixel intensity value for each angle in the original radial summation data set (Figure 3.2 C, column B) is divided by this value (Figure 3.2 C, Column C). We prefer to rescale the alignment data by subtracting 1 from the output of this manipulation (Figure 3.2 C, column D - 1 = column E). To generate our version of the final alignment plot, the normalized 2D FFT alignment values (Figure 3.2 C, column E) are plotted against the angle of acquisition (Figure 3.2 C, column A).

Normalization is tolerant to a degree of error; small deviations around the “perfect value” will not overtly corrupt the alignment plot. Uneven sample illumination at the time of image capture will manifest itself at this point in the process. The baseline values of an alignment plot generated from an image captured under these conditions cannot be uniformly rectified with the X axis; the data trace fails to parallel the X axis. It may be necessary to re-capture the original data image under these circumstances; if this option is not available it may be possible to apply a rolling filter to the existing image to correct the defect (see ImageJ software, select: Process menu, Subtract background, for additional strategies and discussion see also reference 116).

Edge effects can and will add spurious information to the peaks of an alignment plot. The contribution of this of type of noise to a 2D FFT image will be most pronounced in a data set containing aligned fibers that are arrayed at approximately 45° with respect to the border of the image. The 2D FFT function replicates the data image and assembles the duplicate images into a series of “tiles” that resemble a parquet floor. The intersection of fiber edges at the interface of the “tiles” in this parquet floor produces the bulk of edge noise. Edge noise is usually obvious and can be easily discarded by visual inspection of the plotted data. Figure 3.2 B provides an example of a normalized 2D FFT alignment plot containing a corrected (edge noise removed) and uncorrected (edge noise not removed) peak. The corrected peak (seen at 90°) has a 2D FFT alignment value of approximately 0.065 units, whereas the uncorrected peak (seen at 270°) has a 2D FFT alignment value of approximately 0.10 units. Edge noise is usually very distinctive and produces a sharp, prominent spike in the alignment plot. In figure 3.3 D a discrete set of lines (that divide this image into 4 quadrants) is present in the frequency plot. When a radial summation is applied to a frequency plot containing this artifact, the resulting 2D FFT alignment plot will contain a large spike (as illustrated in Figure 3.2 B).

The overall 2D FFT alignment value for a scaffold is determined by visually inspecting and selecting the maximal value from the peak of the alignment plot. A highly aligned scaffold imaged by brightfield microscopy will produce a 2D FFT alignment value of approximately 0.12 units on our scale; for the same fiber field a confocal image will generally produce a slightly higher value (see reference 14 for examples).

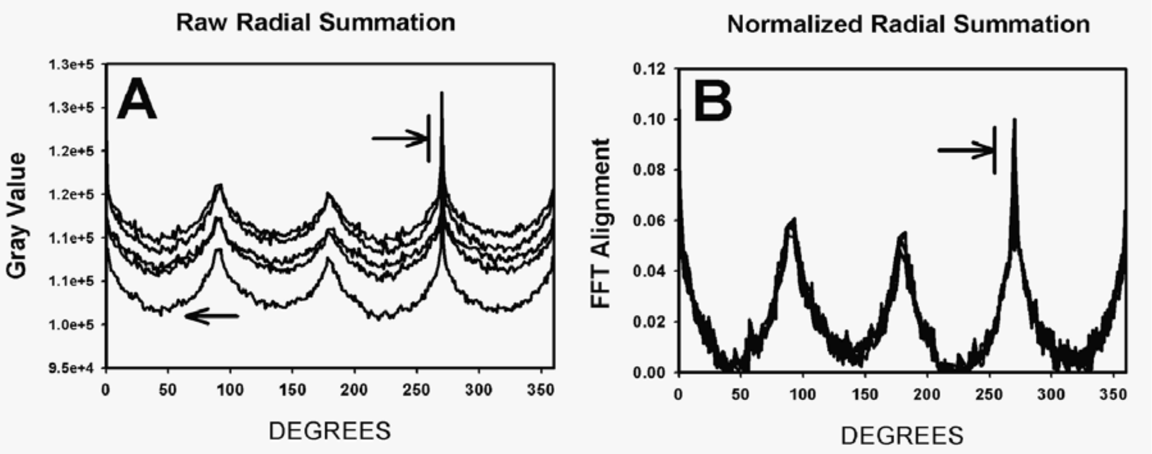

C

A. Angle of Acquisition	B. Pixel Intensity	C. Backgound Subtract	D. Intensity / Background	E. FFT Alignment		F. Sorted Pixel Intensity
0	112323.00	**106666.26**	1.0530	0.0530		105972.28
1	111537.34	106666.26	1.0457	0.0457		106361.15
2	111423.70	106666.26	1.0446	0.0446		106405.56
3	110492.16	106666.26	1.0359	0.0359		106414.61
4	110523.30	106666.26	1.0362	0.0362		106424.50
5	110204.74	106666.26	1.0332	0.0332		106502.50
6	110556.63	106666.26	1.0365	0.0365		106545.52
7	109768.86	106666.26	1.0291	0.0291		106550.01
8	110421.84	106666.26	1.0352	0.0352		106550.30
9	110086.47	106666.26	1.0321	0.0321		106613.32
10	109250.09	106666.26	1.0242	0.0242		106646.27
11	109227.61	106666.26	1.0240	0.0240		106651.67
12	108745.84	106666.26	1.0195	0.0195		**106666.26**
13	108941.67	106666.26	1.0213	0.0213		106670.34

Figure 3.2 A-C. Panel A illustrates the alignment plots for a series of 5 photographs taken of the same fiber field at varying light intensities. As the average light intensity used to capture an image increases the uncorrected alignment plot is displayed upward on the y-axis. The arrow in A denotes a spurious peak associated with edge noise. The arrow at the base of the alignment plot (A) denotes the lower regions of the trace that should be brought in contact with the x-axis during normalization. Panel B illustrates the data depicted in panel A after normalization. The arrow in panel B again denotes edge noise, note: normalization does not remove this spurious noise. This noise is visually removed from the data set. Actual alignment value is denoted by the line at the top of the peak present at approximately 90°. Panel C illustrates the normalization process. See text for complete description

2D FFT Frequency Plot. Model scaffolds were manipulated into varying patterns and imaged to demonstrate how scaffold structure modulates the output of the 2D FFT function and to illustrate how alignment information is encoded and reported by the frequency plot (Figure 3.3). First, consider a model scaffold composed of straight fibers that have been arrayed into a fan shaped pattern (Figure 3.3 A). If the frequency plot is rotated 90° prior to inspection, the high frequency pixels present in this plot will be arrayed into a pattern that mimics the fan-shaped array of fibers that were present in the original data image. These high frequency pixels are generated by the fiber edges, the banded pattern that is evident reflects the spacing of the fibers (Figure 3.3 B). Information concerning fiber spacing is usually lost when a “real” scaffold is processed by the 2D FFT approach. The fibers of an electrospun scaffold are rarely uniformly spaced and they overlap, curve and pass in and out of the plane of focus. The generated 2D FFT alignment plot of the fan array is noisy and continually changing to report the different angles of orientation that occur across the fiber field. Since there is no specific orientation present, no favored polarity will be detected and the 2D FFT alignment value for this model scaffold will be small (Figure 3.3 M, arrayed fan plot).

The random model scaffold illustrated in figure 3.3 C is composed of curving fibers and likely contains as many fiber edges as the fan shaped model scaffold (Figure 3.3 A). The pixel values that correspond to these edges must undergo constant fluctuations to map the curving trajectory of the fibers present in the spatial domain. The frequency plot of this scaffold contains a cluster of low frequency pixels near the origin with the high frequency pixels dispersed in a symmetrical pattern about the origin (Figure

3.3 D). There is no evidence of a preferential orientation or distribution to these pixels, and the 2D FFT alignment plot generated from this data is a smooth trace containing 4 small, symmetrical peaks (Figure 3.3 M, random fiber plot).

A field of aligned, slightly undulating fibers (which more closely resembles the fibers of an aligned electrospun scaffold, Figure 3.3 E) produce high frequency pixels that are preferentially distributed along the vertical axis of the frequency plot (once the plot has been rotated 90°, Figure 3.3 F). The 2D FFT alignment plot of this scaffold (Figure 3.3 M, vertical aligned wavy plot) contains distinct peaks at 90 and 270° (2D FFT alignment value of 0.06 units) and much smaller peaks at 180 and 360° (2D FFT alignment value of 0.02 units). The larger peaks report the principle axis of alignment while the smaller peaks correspond to background information, noise and edge effects (Figure 3.3 M).

The effect of fiber alignment on the concentration of high frequency pixels along a specific axis in the frequency plot is easily demonstrated using a field of fibers that are straight and arranged in parallel (Figure 3.3 G, H and M). In order to generate a spatial map of the vertical edges of these fibers, the pixels of the data image must undergo regular transitions along the horizontal axis in the original data image. The 2D FFT reports this condition as a preferential distribution of high frequency information and the resulting frequency plot contains pixels that are distributed along a narrowly defined axis. When summed, these high frequency pixels produce a characteristic trace on the 2D FFT alignment plot. The alignment peaks are narrow and sharply delineated, indicating nearly uniform fiber alignment (Figure 3.3 M, vertical aligned fiber plot). If a fraction of the fiber population is oriented off the principal axis of orientation the 2D FFT process will produce a broader alignment peak or a peak with a shoulder.

As noted in the previous sections, edge effects and background noise (and detector noise) can “spill over” and obscure data in the 2D FFT frequency and alignment plots. This noise effect is quite pronounced in a model scaffold containing aligned fibers that are arrayed approximately 45° with respect to the edges of the image (Figure 3.3 I, arrow in J indicates noise). Noise of this nature can be greatly diminished by placing a grayscale window mask over the fiber field prior to analysis (Figure 3.3 K, arrow in L indicates the reduced noise). The unmasked image produces a 2D FFT alignment plot with artifacts in the guise of small peaks on either side of the alignment peaks (Figure 3.3 N, arrows). Processing the image with a window mask removes this spurious information without altering the height of the alignment peaks (i.e. 2D FFT alignment value, Figure 3.3 N). Although this type of mask can be useful in many applications, it reduces the total surface area available for analysis. In the illustrated example the spurious peaks are small with respect to the alignment peak; in an electrospun scaffold the artifacts produced by edge noise and the data encoding alignment will produce peaks of similar magnitude.

High resolution microscopy can detect and report considerable variation in pixel intensity across a single fiber. This type of spatial information can add high frequency noise to the 2D FFT frequency plot, partially masking alignment data. SEM images of electrospun scaffolds, where information and variations in contrast are resolved across the diameter of individual fibers, are particularly susceptible to producing this form of interference. One solution that can be applied to reducing this type of interference is to use the Back Scatter mode to capture the images. This imaging mode produces less contrast across the individual fibers than conventional imaging modes. High resolution pixel noise also can be reduced by passing a Gaussian filter across the original data image prior to 2D FFT analysis. This treatment reduces pixel variation and smoothes the data set. Conventional smoothing filters should be avoided; these filters can artificially induce polarity into a data set. Reducing pixel density at the time of image capture or in a digital image prior to 2D FFT processing also can be used to reduce high frequency noise. In practice, images should be captured at the same resolution under similar conditions.

Threshold filters that compress and re-scale data to produce images composed exclusively of black and white pixels have utility in the processing of SEM images. Any use of a Masking filter, Gaussian filter, rolling ball filter, Threshold filter, or manipulation of pixel density should be uniformly applied to each image in a data set that is to be compared.

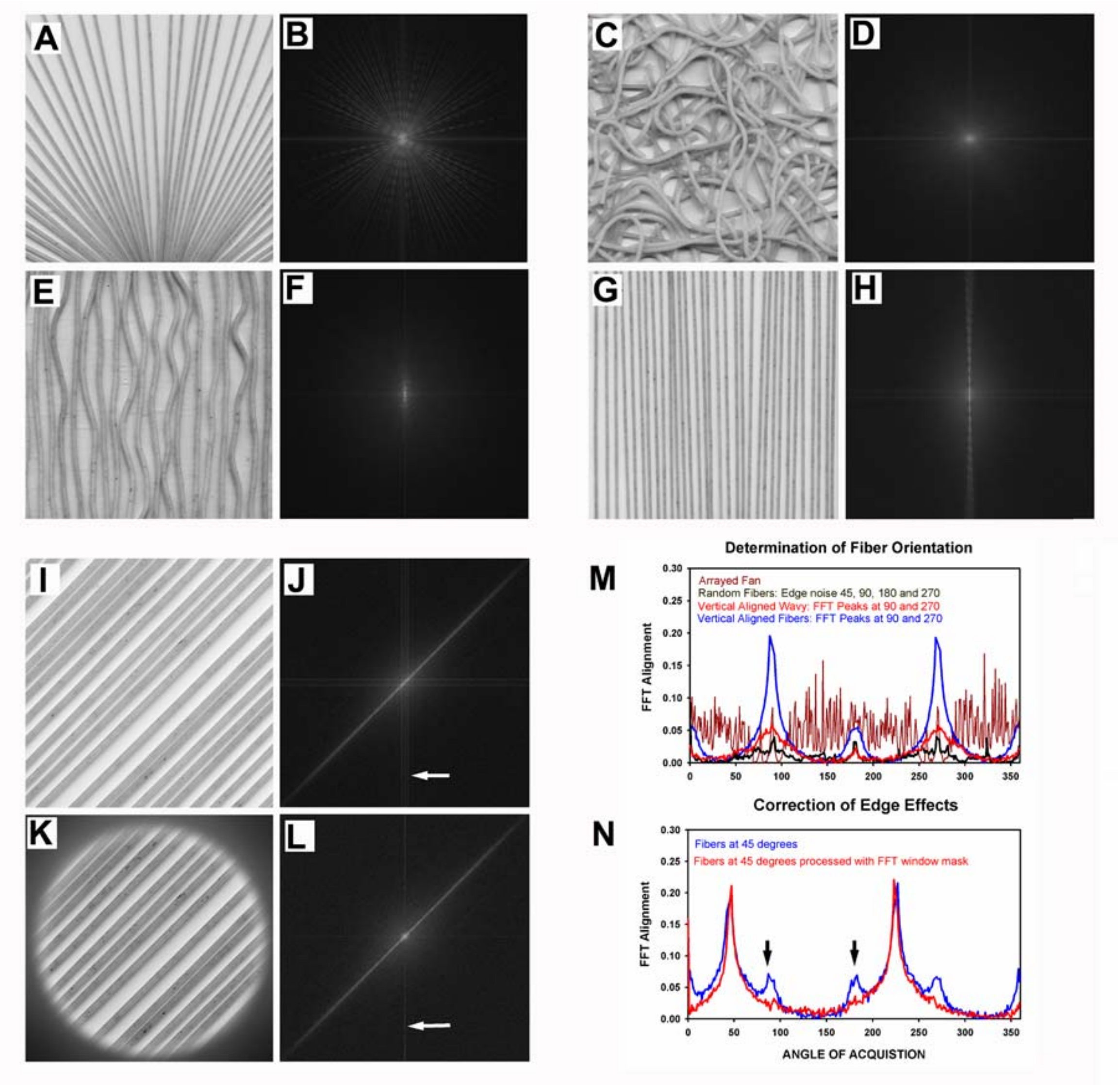

Figure 3.3 A-N. Frequency plots generated from model scaffolds. Images of the model scaffolds and corresponding frequency plots (A-H) (see text for discussion). Panels I-L demonstrate the attenuation of edge effects (arrows in J and L) in a data image through the use of a window mask. 2D FFT alignment plots generated from model scaffolds and illustrated in frequency plots (M). 2D FFT alignment plots before and after removing edge effects (N) from the images depicted in panels I-L. Arrows denote edge noise artifacts.

Dynamic Applications. The 2D FFT approach can also be used to measure other aspects of scaffold structure and performance. For example, we use 2D FFT to examine how mechanical loads impact fiber orientation in tissue-engineering scaffolds. Figure 3.4 illustrates a series of experiments demonstrating the technique. In this experiment we sequentially photographed a dry scaffold as we placed a calibrated strain across the sample. The resulting images were then be analyzed using the 2D FFT approach. The 2D FFT analysis of random scaffolds indicate that fiber alignment remains constant (Figure 3.4 A), failure occurred at a site distal to the actual domain imaged.

When a dry scaffold composed of aligned fibers was stretched in parallel with the principal axis of anisotropy there was a nominal increase in the 2D FFT alignment value prior to failure (from 0.08 to 0.11 units at 5.0% stretch, Figure 3.4 B). Applying stretch in a tangential fashion to an aligned matrix induced modest changes in the principal angle of fiber orientation prior to scaffold failure (not shown). We conclude from these experiments that strains are not uniformly distributed throughout a dry scaffold, failure (fracture) occurs at a specific site in the construct. We believe that fibers in a hydrated state would undergo far more re-alignment in response to strain than in a dry specimen.

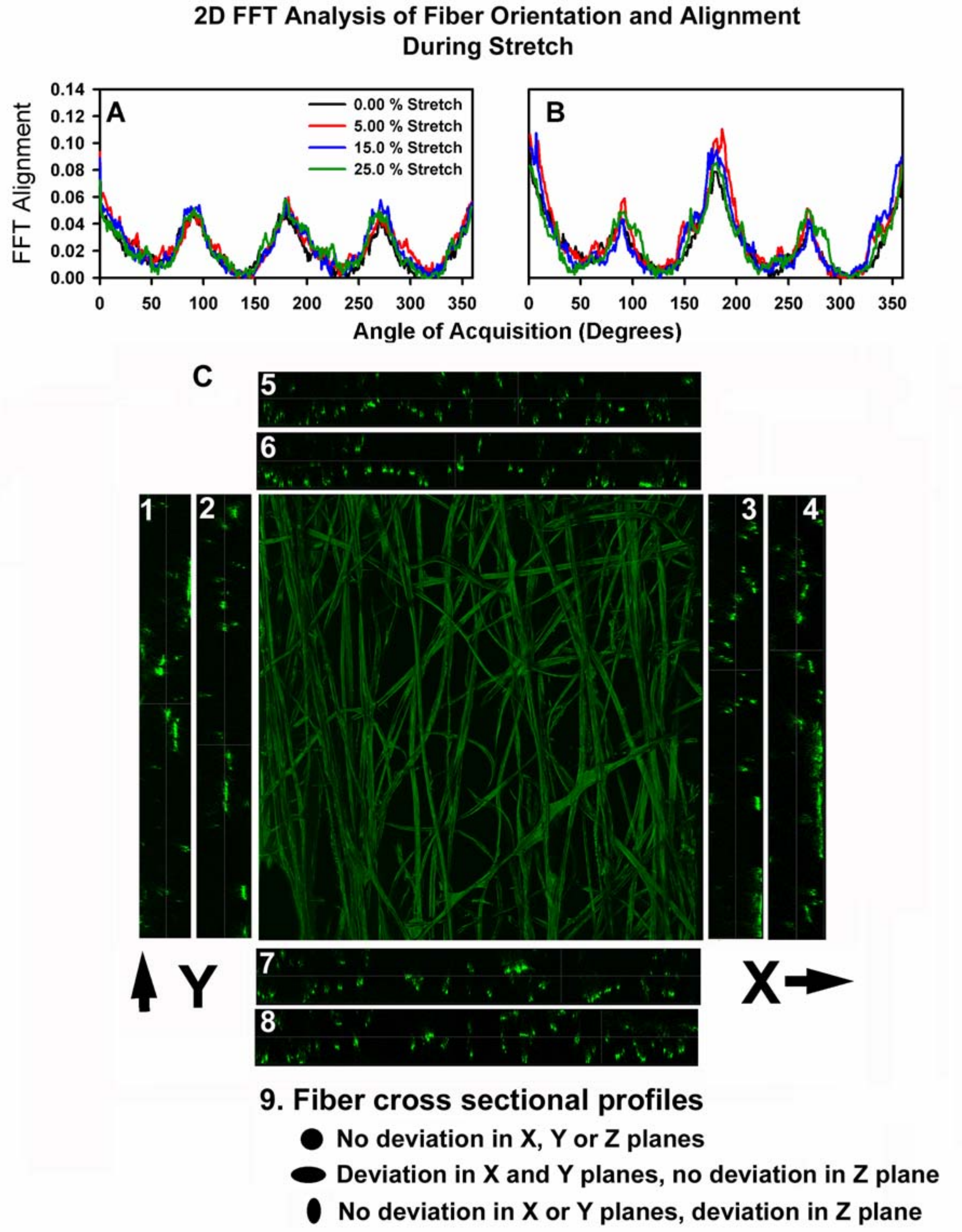
2D FFT Analysis of Fiber Orientation and Alignment During Stretch
A
B
FFT Alignment
0.00
0.02
0.04
0.06
0.08
0.10
0.12
0.14
0
50
100
150
200
250
300
350
Angle of Acquisition (Degrees)
0.00 % Stretch
5.00 % Stretch
15.0 % Stretch
25.0 % Stretch
C
1
2
3
4
5
6
7
8
Y
X
9. Fiber cross sectional profiles
● No deviation in X, Y or Z planes
⬬ Deviation in X and Y planes, no deviation in Z plane
⬮ No deviation in X or Y planes, deviation in Z plane

Figure 3.4 A-C. Use of the 2D FFT in dynamic applications and laser confocal microscopy. (A) 2D FFT alignment plot of a random scaffold at 0, 5, 15 and 25% stretch. Fibers of a dry, random scaffold do not undergo re-distribution in response to applied strain. (B) 2D FFT alignment plot of a partially aligned scaffold at 0, 5, 15 and 25% stretch. A nominal change in fiber alignment was detected in this sample at 5% stretch. (C) Confocal data set compiled as an average projection. Subsections 1-4: cross-sections imaged in the y-orientation (i.e., y-z planes). Subsections 5-8: cross-sections imaged in the x-orientation (i.e., x-z planes). Subsection 9: illustrates theoretical cross-sectional profiles observed when fibers traverse an optical plane (note: simultaneous deviations in x, y, and z planes are not illustrated).

Future Directions. Electrospun fibers appear to deposit as discrete layers onto the target mandrel. To further modulate the material and biological properties of an electrospun scaffold, we are interested in developing strategies to induce more fiber entanglement in the Z direction and using 2D FFT to evaluate the trajectory of these fibers. For example, consider the confocal image presented in figure 3.4 C that is composed of fibers that are predominately arrayed along the vertical orientation of the image. Conventional 2D FFT analysis of this confocal image generates an alignment value of 0.17 units (moderately aligned for a scaffold captured by confocal imaging). It is possible to verify fiber orientation in this scaffold by surveying the confocal three-dimensional data set in cross-section. Representative cross-sections of the illustrated example in the X and Y axis reveals a higher frequency of elongated fiber profiles in the Y axis (aligned fibers cut longitudinally, Figure 3.4 C, panels 1-4) than in the X axis. This structure occurs because fibers are arrayed in parallel with the Y axis. In contrast, fiber profiles in the X axis are predominately round or oval in shape (aligned fibers cut in cross-section, Figure 3.4 C, panels 5-8). At present we are adapting our optical methods to measure the shape of the cross-sectional profiles of fiber populations in large, three dimensional confocal data sets. This information can be used to map and measure the trajectory of individual fibers in the X, Y and Z directions (Figure 3.4 C, panel 9). The cross-sectional profile of individual fibers also can theoretically be used to extrapolate fiber trajectory information using the 2D FFT function.

DISCUSSION

Electrospun materials can be uniquely tailored to specific tissue-engineering applications to mimic the physical, biological and material properties of the native extracellular matrix. For example, fiber diameter and pore dimension of a given polymer scaffold can be largely controlled by regulating the concentration of polymer (viscosity and degree of chain entanglements) present in the starting solution [14][106] and/or the electrospinning air gap, accelerating voltage [109][117][118] and/or target properties [14]. Biological activity can be manipulated by controlling fiber identity and the overall composition of the electrospun tissue engineering scaffold [15]. Growth factors and other pharmaceuticals can be selectively added to the scaffolds during and/or after the electrospinning process [119]. Material properties can be modulated by altering scaffold structure, composition, and through post-electrospinning processing events that increase fiber cross-linking [64].

The frequency plot of the 2D FFT function has been used to select, identify and measure the geometric composition of images in a broad spectrum of applications. Quantitative information concerning the orientation of objects in a data image also is encoded by this plot. By processing a digital image of an electrospun scaffold with the 2D FFT function it is possible to extract this information and use this data to assign a numerical value to the degree of fiber alignment present in the original sample [63].

The 2D FFT approach is a relatively simple technique to put into practice; however, there are clear limitations. For example, imaging modality and sample thickness must be considered prior to analysis. In brightfield microscopy samples must be thin enough to allow light to pass through the specimen. This imaging modality is most suited for samples composed of fibers arrayed in a homogenous fashion. Structures that exhibit discrete fiber layers that are engineered to display differing degrees of alignment in each layer are generally not suited for analysis by brightfield microscopy. This limitation exists because fibers out of the plane of focus can participate in generating data that is used by the 2D FFT function.

Constructs composed of complex multiple layers are better imaged by laser scanning confocal microscopy, an imaging technique that can be used to capture data from specific optical planes. For many proteins and selected synthetic polymers, images can be captured using an auto-fluorescence signal. We also have successfully used reflectance mode to capture images of scaffolds composed of biological [14] and synthetic materials [84]. This approach can be used to capture information for 30-40μm of depth in the Z direction. For more extensive penetration, markers may be incorporated into scaffolds at the time of electro-processing. If appropriate, standard immunohistochemical methods can be used to stain and image scaffolds composed of native proteins. For extremely dense or thick (i.e. in the Z direction) electrospun constructs, the use of a 2 photon confocal imagining system may be necessary. Note, as sample thickness increases, there will be increased photon scatter. Under these conditions de-convulsion analysis may be necessary to accurately construct the data set. Three dimensional confocal data files, in general, are biased in the Z direction. In cross-sectional analysis, this bias will take a round profile and elongate it into an oval profile (for an excellent discussion of image restoration and deconvolution see 120). By analogy, for a model matrix composed of round spaghetti, Z direction bias would make this pasta appear flattened and elongated like linguini when viewed in cross-section. Deconvolution corrects this bias by reshaping the point spread function, a manipulation that takes on added importance when fiber alignment in multiple dimensions is to be calculated.

While we prefer to use confocal microscopy to characterize different fiber layers, it also is possible to generate similar information by sequentially sampling a specimen during the electrospinning process. In order to conduct this type of analysis the electrospinning process must be stopped to isolate a sample of each fiber layer. The individual samples can then be imaged and processed by 2D FFT. We do not recommend this strategy on a routine basis, unless necessary. Fiber layers may delaminate as a result of drying incurred during the sampling intervals, a condition that may adversely impact sample integrity and structure.

Finally, in the analysis of fiber alignment it is critical to consider what precisely scaffold anisotropy represents to each individual application. Certainly the 2D FFT approach can be used to verify the reproducibility of the electrospinning conditions and the structure of a scaffold. However, for most applications, some external measure of anisotropy or scaffold performance is usually necessary to calibrate the 2D FFT alignment value. For example, our principle objective has been to identify how fiber diameter and varying degrees of fiber alignment interact to modulate the material properties of an electrospun material [14][63][106]. The stress and strain properties of an idealized scaffold composed of random elements should be identical regardless of the testing angle. These material properties can be expected to develop directional bias and vary as increasing degrees of anisotropy are introduced into the matrix. We have used these characteristic properties to calibrate our 2D FFT alignment values. In our laboratories, an archival image of each scaffold is captured and processed for 2D FFT analysis. The scaffold is then subjected to materials testing in the parallel and perpendicular orientations and analyzed using stress at failure [63]. In conventional materials testing this material property appears track most closely with incremental changes in fiber alignment.

Applications in which the central objective is to promote the expression of a specific cell phenotype or provide a guidance cue may require a different external measure of performance. For example, we have examined how scaffold anisotropy can be used to promote neurite outgrowth in specific directions. This body of work suggests that electrospun scaffolds do not have to be composed of uniformly aligned arrays of fibers to direct the growth of neurons along a predefined axis [84]. Some yet to be defined threshold of alignment is necessary to achieve this objective, a result that has direct implications in the fabrication of nerve guides and other tissue engineered products designed to direct cell phenotype.

The 2D FFT approach has several advantages, notably, software is readily available, easy to implement and very little specialized equipment is needed to generate objective measurements of alignment. A variety of different imaging modalities, including brightfield, laser scanning confocal and scanning electron microscopy, can be used to capture data for analysis. The technique is adaptable and we demonstrated that it can be used quantify dynamic changes in fiber alignment in response to mechanical loads. By coupling the 2D FFT approach with laser scanning confocal microscopy it is possible to generate alignment data in three dimensions and/or within specific optical planes. Notably, the non-destructive nature of the 2D FFT approach makes it possible to measure fiber alignment in a specific sample and subsequently use that scaffold in a tissue-engineering application.

CHAPTER 4 Control of Fiber Alignment in Electrospun Scaffolds

Preface: The following manuscript appeared in Biomaterials, 2006, volume 27, pages 5524-5534 [14]. The work included demonstrates the effect of fiber diameter and mandrel speed on the induction of anisotropy in electrospun scaffolds. Additionally, the use of the fast Fourier transform as a tool for measuring the degree of alignment in a scaffold is described. The ability to closely control and measure fiber alignment is crucial for the production of a scaffold that recapitulates the structure of the native extracellular matrix. Additional details regarding the effect of electrospinning voltage and air gap distance on the initiation of scaffold anisotropy can be found in Appendix A.

Modulation of Anisotropy in Electrospun Tissue-Engineering Scaffolds: Analysis of Fiber Alignment by the Fast Fourier Transform

CE Ayres[1], GL Bowlin[1], SC Henderson[2], LT Taylor[1], J Shultz[3], J Alexander[4], TA Telemeco[5] and DG Simpson[2]

[1]Department of Biomedical Engineering
Virginia Commonwealth University
Richmond, VA 23284

[2]Department of Anatomy and Neurobiology
Virginia Commonwealth University
Richmond, VA 23298

[3]Department of Biochemistry
Virginia Commonwealth University
Richmond, VA 23298

[4]Department of Neurobiology
University of Chicago
Chicago, IL 60637

[5]Division of Physical Therapy
Shenandoah University
Winchester, VA 22601

ABSTRACT

We describe the use of the fast Fourier transform (FFT) in the measurement of anisotropy in electrospun scaffolds of gelatin as a function of the starting conditions. In electrospinning, fiber alignment and overall scaffold anisotropy can be manipulated by controlling the motion of the collecting mandrel with respect to the source electrospinning solution. By using FFT to assign relative alignment values to an electrospun matrix it is possible to systematically evaluate how different processing variables impact the structure and material properties of a scaffold. Gelatin was suspended at varying concentrations (80, 100, 130 and 150 mg/ml) and electrospun from 2,2,2 trifluoroethanol onto rotating mandrels (200-7000 RPM). At each starting concentration, fiber diameter remained constant over a wide range of mandrel RPM. Scaffold anisotropy developed as a function of fiber diameter and mandrel RPM. The induction of varying degrees of anisotropy imparted distinctive material properties to the electrospun scaffolds. The FFT is a rapid method for evaluating fiber alignment in tissue engineering materials.

INTRODUCTION

The native extracellular matrix (ECM) is comprised of a complex network of structural and regulatory proteins that are arrayed into a fibrous matrix [121]. The fibers that make-up the backbone of this elaborate network exhibit distinctive, and often times, regional, variations in identity, cross-sectional diameter and polarity. For example, the ECM of the dermis can be subdivided into two discrete sub-compartments: a deep reticular layer and a superficial papillary layer. The reticular compartment is occupied by large diameter fibers of Type I collagen and elastin that are distributed into large-scale random bundles. Conversely, the superficial papillary layer of the skin contains small diameter fibers of Type III collagen and elastin that exhibit a modest degree of anisotropy. This fibrous network defines the bulk material properties of the dermis. However, the three dimensional architecture and composition of the dermal ECM also functions to store and communicate phenotypic signals to the cellular compartment of the skin. These signals modulate cell function during normal hemostatsis and also play a central role in modulating the remodeling events that transpire during the wound healing process. The multifunctional nature of the native ECM must be recognized and replicated to varying degrees in the design and fabrication of tissue-engineering scaffolds.

We believe that electrospinning can be used to produce tissue-engineering scaffolds that recapitulate key structural features of the native extracellular matrix (ECM) [15]. This non-mechanical processing strategy can be used to selectively fabricate sub-micron to micron diameter fibers from a variety of synthetic polymers

[78][106][122][123] and natural proteins [13][15][61][62][65][124]. Fiber diameter and pore dimension can be regulated in the electrospinning process by controlling the composition of the electrospinning solvent and the identity, degree of chain entanglements, and concentration of the starting polymer [117]. Fiber alignment can be manipulated by controlling the motion of the collecting mandrel with respect to the source electrospinning suspension [61][106][110] and/or through electric field effects [109]. Conventional morphometric techniques are typically used to characterize the basic physical properties of electrospun scaffolds [13][15][110][122].

We believe that efforts to produce clinically relevant tissue-engineering scaffolds, using the electrospinning process, can benefit from strategies that objectively measure and assign a value to fiber anisotropy. Varying the degree of fiber anisotropy present in an electrospun scaffold can be expected to impart unique material properties to the construct. Fiber anisotropy also may represent a source of guidance cues that can be exploited to regulate cell phenotype, cell distribution and the macroscopic properties of an engineered tissue.

Laser scattering has been used to evaluate fiber alignment in valve leaflets [111][112]. This elegant technique can be used to resolve information at the individual fiber scale. However, intensive data analysis is necessary to map the large-scale structural properties of a sample. We, and other authors, have used representative scanning electron micrographs to demonstrate fiber alignment in electrospun materials [13][105][106][109][110]. Unfortunately, this approach is highly subjective and is restricted to generating data sampled from the superficial surfaces of the constructs. In this study, we use digital brightfield and confocal microscopy to capture images of electrospun scaffolds and demonstrate the use of the fast Fourier transform (FFT) to measure fiber alignment in the scaffolds. Our approach has several advantages; it is rapid, non-destructive and can be used to rapidly integrate alignment data over a relatively large area.

MATERIALS AND METHODS

Electrospinning. Reagents were purchased from Sigma Aldrich (St. Louis, MO) unless noted. Gelatin was suspended in 2,2,2 trifluoroethanol (TFE) for 48 hr prior to electrospinning. This time interval was determined empirically. In preliminary experimentation, gelatin was suspended for 12, 24, 48 or 96 hr in TFE. The 48 hr time point produced the most consistent fiber diameters (not shown). Starting concentrations of 80, 100, 130 and 150 mg/ml TFE were prepared. Electrospinning suspensions were loaded into a 20 ml Becton Davis syringe capped with an 18 gauge blunt tipped needle. Samples were electrospun at 22 kV onto a stainless steel rectangular mandrel (70 mm x 10 mm x 5 mm) across an air gap of 20 cm.

The positive output lead of a high voltage supply (Spellman CZE1000R; Spellman High Voltage Electronics Corporation) was attached by an alligator clip to the blunt end needle. A Harvard perfusion pump was used to meter the delivery of the electrospinning suspensions to the electric field. The rate of solvent/polymer delivery was set at the maximal rate that did not induce dripping from the tip of the syringe. Starting concentrations of 80, 100, 130 and 150 mg/ml were delivered at rates of 12, 20, 21 and 35 ml/hr, respectively. The target mandrel was regulated to rotate at varying revolutions per minute (RPM) including: 200 (we chose to use a nominal degree of rotation in our controls to facilitate fabrication of scaffolds for materials testing, which assumes a uniform scaffold thickness), 1000, 2000, 3000, 4000, 5000, 6000 and 7000 RPM. A digital stroboscope (Shimpo Instruments DT3-11A) was used to continuously monitor the

RPM of the target mandrel. Samples were stored in a desiccation chamber prior to analysis.

Viscosity Measurements. Gelatin/TFE solutions were suspended for 24 and 48 hr at varying concentrations. Viscosity measurements were conducted with a Brookfield RVDV-III Ultra programmable rheometer using a small sample adapter and spindle (SC4-21). Prior to all measurements, the rheometer was calibrated using a viscosity standard fluid that was allowed to equilibrate for 30 min before an initial viscosity reading was recorded.

Scanning Electron Microscopy. Average fiber diameters and average pore areas were determined from samples processed for conventional Scanning Electron Microscopy (SEM, Jeol JSM-820). Dry, unfixed electrospun materials were sputter coated and images were captured on Polaroid film, digitized via a flatbed scanner and analyzed with NIH ImageTool (UTHSCSA version 3). All measurements were calibrated from size bars incorporated into the SEM images at the time of capture.

Average fiber diameter was determined from measurements taken perpendicular to the long axis of the fibers (25 measurements per field). Average pore area (a measure of porosity) was determined by measuring the area encompassed by adjacent fibers (at least 25 measurements per field). N=3 from independent experiments conducted at different time points. Data sets consisting of average fiber diameter and average pore area were screened by two-way ANOVA and tested for the effects of the starting concentration and mandrel RPM, P<0.01. A Tukey test was used for *Post Hoc* analysis; significance was defined at P<0.05.

Light Microscopy. All imaging and materials testing was conducted with dry, unfixed samples. This approach was selected to allow us to make direct comparisons between the different analytical approaches described in this study. For light microscopy, dry sheets of electrospun gelatin were cut into 10 mm diameter disks using a circular biopsy punch. Samples were imaged with a Nikon TE300 microscope equipped with a Nikon DXM 1200 digital camera. Images (3840 x 3072 pixels) were captured with a 20X (0.40 n.a.) brightfield objective lens, resulting in pixel dimensions of 0.17 x 0.18 μm.

FFT. The FFT was used to characterize fiber alignment as a function of electrospinning conditions. The FFT function converts information present in an original data image from “real” space into mathematically defined “frequency” space [125]. The resulting FFT output image contains grayscale pixels that are distributed in a pattern that reflects the degree of fiber alignment present in the original data image. As subjectively judged from SEM images, a representative FFT analysis of a “random” matrix and an “aligned” matrix are presented in figure 4.1. The FFT of an original data image containing random fibers (Figure 4.1 A) generates an output image containing pixels distributed in a symmetrical, circular shape (Figure 4.1 B). This distribution occurs because the frequency at which specific pixel intensities occur in the data image is theoretically identical in any direction. In contrast, the FFT of a data image containing aligned fibers (Figure 4.1 D) results in an output image containing pixels distributed in a non-random, elliptical distribution (Figure 4.1 E). This distribution occurs because the pixel intensities are preferentially distributed with a specific orientation.

A graphical depiction of the FFT frequency distribution can be generated by placing a circular projection on the FFT output image and conducting a radial summation of the pixel intensities for each degree between 0 and 360^0, in 1^0 increments. For example, data corresponding to 0^0 in figure 4.1 C was obtained by summing the pixel intensities encountered along that specific radius in the FFT output image depicted in figure 4.1 B. The summed value of the pixel intensity was then plotted as a function of the degree and in this example provided a value of approximately 0.02 at 0^0. A similar analysis at 100^0 in figure 4.1 E generates a value of approximately 0.16. In our analysis the pixel intensities were summed along each degree and then plotted between 0 and 180^0 (the FFT is symmetric about the horizontal axis so a pixel summation to 360^0 is unnecessary). In all images, the FFT data set has been rotated 90^0 to correct for the mathematical transformation inherent to this type of analysis, allowing the principal axis of orientation to be directly determined from the position of the peak in the intensity plot. The amount of alignment present in the original data image is reflected by the height and overall shape of the peak present in this plot (Figure 4.1 C and F).

For our analysis, digitized SEM images and brightfield light microscopic images were converted to 8-bit grayscale TIF files. SEM images were cropped to 1024 x 1024 pixels and brightfield images were cropped to 2048 x 2048 pixels. Images were processed with ImageJ software (NIH, http://rsb.info.nih.gov/ij) supported by an oval profile plug-in (authored by William O'Connnell). All FFT data was normalized to a baseline value of 0 and plotted in arbitrary units, allowing different data sets to be directly compared.

Confocal Laser Scanning Microscopy. To enhance confocal imaging TFE/gelatin suspensions were supplemented with 1µl/ml CellTracker CM-DiI (Invitrogen, USA) and electrospun as described ("random"=80 mg/ml gelatin @ 4000 RPM or "aligned"=130 mg/ml gelatin @ 4000 RPM). Confocal images can be captured using auto-fluorescence, however, when working with small diameter fibers this signal is inadequate for image acquisition. Electrospun scaffolds were mounted onto microscope slides; registry marks were incorporated onto the surface of the cover slips. The samples were imaged by brightfield (widefield) microscopy, photographed and processed for FFT analysis of alignment as described above. These same scaffolds were then imaged by confocal microscopy using the registry marks to identify the regions captured by brightfield microscopy. Samples were imaged with a Leica TCS-SP2 AOBS confocal laser scanning microscope.

The random matrix depicted in figure 4.4 D was imaged with a 40X (1.25 n.a.) oil immersion lens. Total surface area measured 185 x 185 µm and the total depth in the Z direction was 10 µm sampled at intervals of 0.162 µm. The Voxel dimensions for this image are 0.09 x 0.09 x 0.16 µm. The aligned matrix depicted in figure 4.4 F was imaged with a 20X (0.70 n.a.) dry objective lens. Total surface area measured 750 x 750 µm and the total depth in the Z direction was 25 µm sampled at intervals of 0.36 µm. The Voxel dimensions for this image are 0.36 x 0.36 x 0.36 µm. The pinhole was optimized for all images to the Airy disk. The 514 nm laser line was used to illuminate the samples and images were collected with a scan resolution of 2048 x 2048 pixels and saved as TIF files. Confocal 3-dimensional data sets were compiled as average intensity and maximum intensity projections and processed by FFT. These data were then compared to the FFT alignment values derived from the brightfield (widefield) data sets. Representative cross-sections in the confocal data sets were calculated and projected along the X and Y orientations (*i.e.* XZ and YZ digital slices).

Materials Testing. Uniaxial materials testing was conducted on dumbbell shaped samples of electrospun gelatin with a Bionix 200 Mechanical Testing Systems instrument equipped with a 50N load cell (MTS Systems Corp, Eden Prairie, MN). Samples were 2.67 mm wide with a gauge length of 11.25 mm. Specimen thickness was determined with a Mitutoyo IP54 digital micrometer (Mitutoyo American Corp; Aurora, IL). Dog bone shaped samples were used to control for grip effects and the geometry of the samples to be tested. Samples were tested in the parallel (*i.e.* in the direction of mandrel rotation) and perpendicular orientations (*i.e.* at 90^0 to the direction of mandrel rotation) to the point of failure at an extension rate of 10 mm/min. Data sets were screened by one-way ANOVA ($P<0.01$) to test for the effects of mandrel RPM on material properties. Samples that passed normality and equal variance were subjected to pairwise multiple comparisons (Tukey test, $P<0.05$).

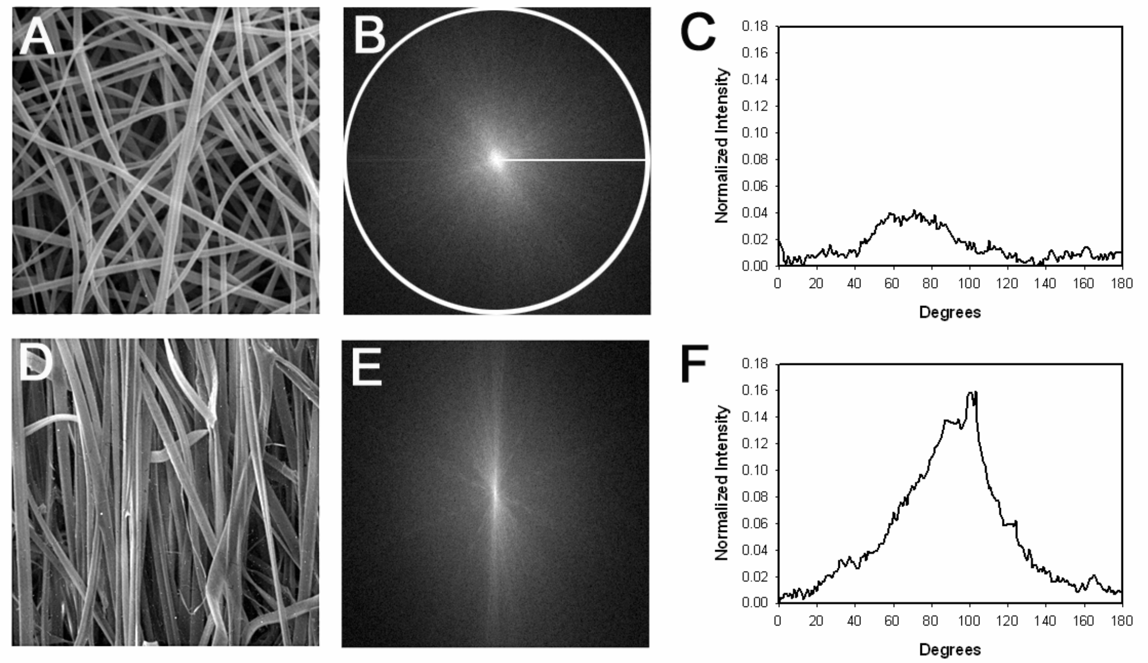

Figure 4.1 A-F. Representative SEM images of a random matrix (A) and an aligned matrix (D). FFT output images (B and E) and radial projection (B). Pixel intensity plots against the angle of acquisition for a random matrix (C) and an aligned matrix (F). Note the distinctive peak produced by the image containing aligned information (F).

RESULTS

Fiber Diameter and Pore Area. Average fiber diameters and average pore areas in electrospun samples were determined as a function of starting electrospinning conditions. Under base line conditions (*i.e.* mandrel RPM=200) 80 mg/ml suspensions produced scaffolds composed of 0.29 ± 0.1 μm diameter fibers with pore areas of 0.49 ± 0.7 μm^2; 100 mg/ml suspensions produced 2.90 ± 1.2 μm diameter fibers with pore areas of 67.60 ± 53.0 μm^2; 130 mg/ml suspensions produced 2.80 ± 1.0 μm diameter fibers with pore areas of 95.00 ± 80.0 μm^2; and 150 mg/ml suspensions produced 9.10 ± 2.6 μm diameter fibers with pore areas of 301.00 ± 224.0 μm^2. Fibers produced from the 80, 100 and 130 mg/ml suspensions had a rounded cross-sectional profile. The 150 mg/ml suspensions produced fibers with a ribbon-like profile. This conformation is believed to develop from the production of a thin walled, hollow fiber that collapses as solvent evaporates [118][126]. We note that this phenomenon can potentially increase average cross-sectional fiber diameters when samples are measured by SEM.

Screening the morphometric data sets detected three classes of scaffolds composed of distinct fibers and pore areas ($P<0.001$). These classes consisted of scaffolds produced from: I) 80 mg/ml suspensions containing fibers with cross-sectional diameters of less than 1 μm and pore areas of less than 1 μm^2, II) 100 and 130 mg/ml suspensions containing fibers with cross-sectional diameters between 1 and 5 μm and pore areas ranging between 20 and 100 μm^2 and III) 150 mg/ml suspensions containing fibers with cross-sectional diameters greater than 5 μm and pore areas greater than 100 $μm^2$ (Figure 4.2 A and D).

We were unable to definitively resolve the nature of the relationships that exist between starting concentration, solution viscosity and fiber diameter. Regression analysis examining average fiber diameter as a function of gelatin concentration using a linear model generated a R^2 value of 0.54 and a second order model gave a R^2 value of 0.56 (Figure 4.2 B, inset). Linear regression analysis examining how solution viscosity varied as a function of gelatin concentration provided a R^2 value of 0.98, fitting a second order function to these data produced a R^2 value of 0.99 (Figure 4.2 C, inset).

Impact of Mandrel Rotation. To determine how the rotation of a rectangular grounded mandrel affects scaffold structure, we varied the mandrel speed from 200 to 6000 RPM in 1000 RPM increments. With one exception, fiber diameter was not regulated by mandrel RPM. ANOVA testing and *post hoc* analysis of scaffolds produced from the 80 mg/ml suspension sets indicated that fibers deposited onto a grounded target rotating at 2000 RPM were, on average, larger than fibers collected at 200 RPM ($P<0.05$). Mandrel RPM did not alter average fiber diameter in scaffolds produced from suspension concentrations of 100, 130 or 150 mg/ml under any of the conditions assayed (Figure 4.2 A).

Mandrel RPM had a more pronounced impact on average pore area (Figure 4.2 D). In scaffolds electrospun from the 80 mg/ml suspensions, average pore area increased when collected at 2000 and 6000 RPM versus those collected at 200 RPM ($P<0.05$). For scaffolds produced from the 100 and 130 mg/ml suspensions, average pore area decreased at all mandrel RPMs with respect to 200 RPM ($P<0.05$). In scaffolds electrospun from 150 mg/ml suspensions, average pore area decreased in the 5000 and 6000 RPM treatment groups with respect to 200 RPM ($P<0.05$). These data suggest that under specific conditions fiber packing is more efficient as mandrel RPM is increased, a result that is consistent with the induction of increased fiber alignment.

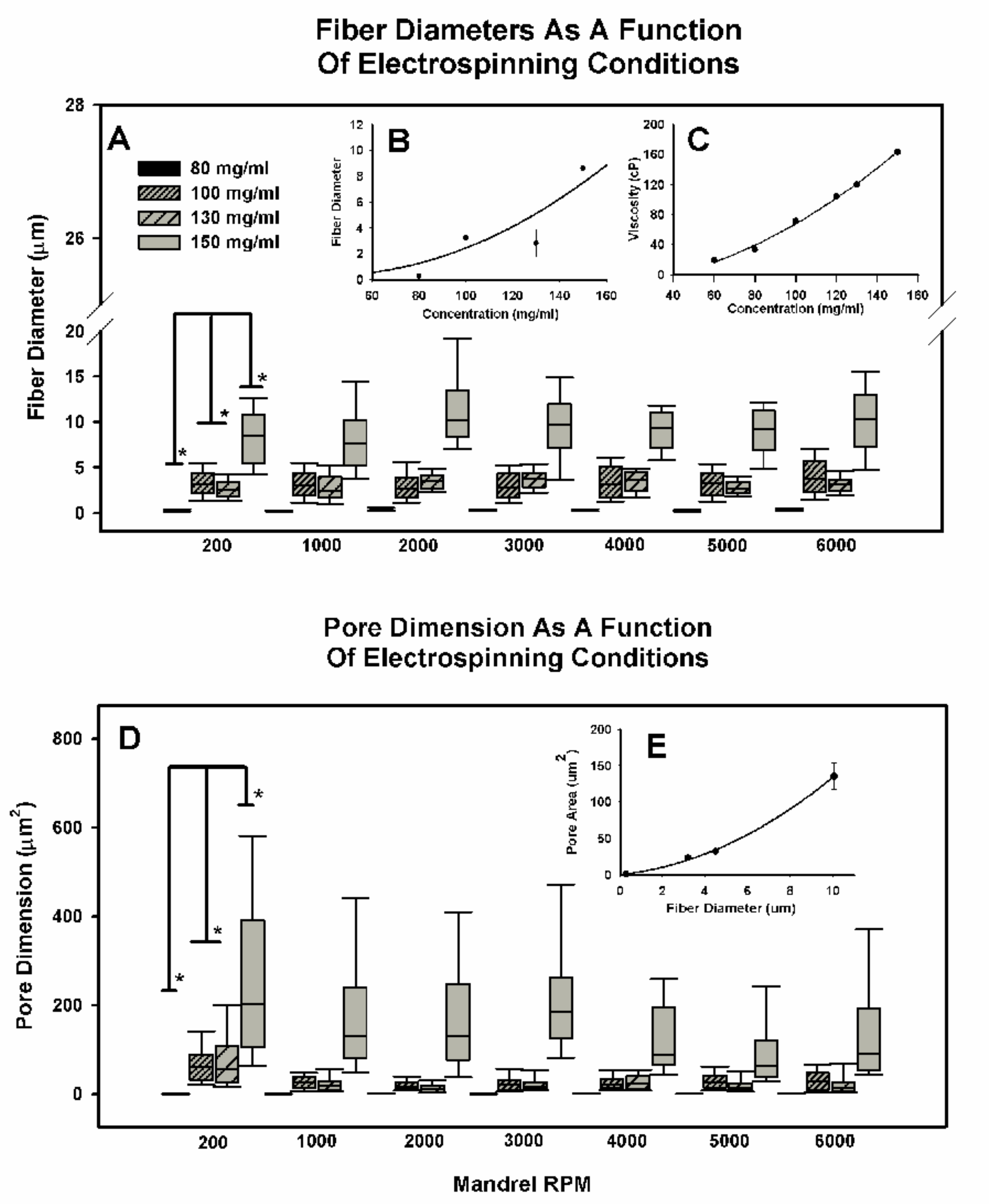

Fiber Diameters As A Function Of Electrospinning Conditions
A
80 mg/ml
100 mg/ml
130 mg/ml
150 mg/ml
Fiber Diameter (μm)
28
26
20
15
10
5
0
*
*
*
B
Fiber Diameter
12
10
8
6
4
2
0
60
80
100
120
140
160
Concentration (mg/ml)
C
Viscosity (cP)
200
160
120
80
40
0
40
60
80
100
120
140
160
Concentration (mg/ml)
200
1000
2000
3000
4000
5000
6000
Pore Dimension As A Function Of Electrospinning Conditions
D
Pore Dimension (μm^2)
800
600
400
200
0
*
*
*
E
Pore Area (um^2)
200
150
100
50
0
0
2
4
6
8
10
Fiber Diameter (um)
200
1000
2000
3000
4000
5000
6000
Mandrel RPM

Figure 4.2 A-E. Fiber diameter (A) and pore area (D) as a function of mandrel RPM. Bars at 200 RPM indicate three classes of fibers (A) and pore areas (D) detected by statistical analysis ($P<0.001$). Inset (B), 2nd order modeling of fiber diameter as a function of starting concentration at 200 RPM, $R^2=0.56$. Inset (C), regression analysis of the relationship between starting concentration and solution viscosity, 1st order $R^2=0.98$, 2nd order $R^2=0.99$ (depicted). Inset (E), 1st order modeling of pore area as a function of fiber diameter at 200 RPM, $R^2=0.33$. Error bars B and E = ± standard deviation.

Fiber Alignment and Scaffold Anisotropy as Judged by FFT. We used FFT analysis of brightfield images to characterize scaffold anisotropy and assign a numerical value to fiber alignment. For this type of analysis, the degree of fiber alignment in a data image is reported by the height and shape of the peak generated by the FFT plot (Figure 4.1). The higher the peak, the more precisely aligned the fibers are along a single axis of orientation. Gelatin electrospun from a starting concentration of 80 mg/ml did not exhibit overt evidence of alignment at any mandrel RPM. The normalized intensity values (or FFT alignment value) of these scaffolds did not exceed 0.05 arbitrary units (Figure 4.3 A) for any of the conditions assayed and the total area under the curve remained less than 2.10 arbitrary units (Figure 4.3 E).

Statistical analysis indicates that scaffolds produced from 100 and 130 mg/ml suspensions have similar fiber diameters and pore areas. However, FFT analysis indicates subtle differences may exist to distinguish these two treatment groups. FFT alignment values for scaffolds prepared from the 100 mg/ml suspensions sequentially increased as a function of mandrel RPM (Figure 4.3 B and E). At 1000 RPM the alignment value was approximately 0.02 units for these scaffolds and peaked at 0.08 units in samples collected at 6000 RPM. In contrast, alignment values assigned to scaffolds produced from the 130 mg/ml suspensions were similar in nature and exceeded 0.08 for samples collected at 1000, 2000, 3000, 4000, and 5000 RPM (Figure 4.3 C and E). These data are consistent with our conclusions that pore size decreases with respect to controls in these samples, when mandrel RPM is greater than 1000, as a consequence of increased fiber alignment (and packing efficiency, see Figure 4.2).

Scaffolds electrospun from starting concentrations of 150 mg/ml produced FFT alignment values of 0.08 units at 200 RPM (Figure 4.3 D). This FFT alignment value exceeded the values observed for all of the scaffolds prepared from the 80 mg/ml suspensions and most of the 100 mg/ml suspensions. These results may explain why pore size (Figure 4.2) in the 150 mg/ml samples was not markedly altered until the mandrel RPM reached 5000 RPM (Figure 4.3). These fibers already have a high degree of alignment and pack efficiently even under baseline conditions.

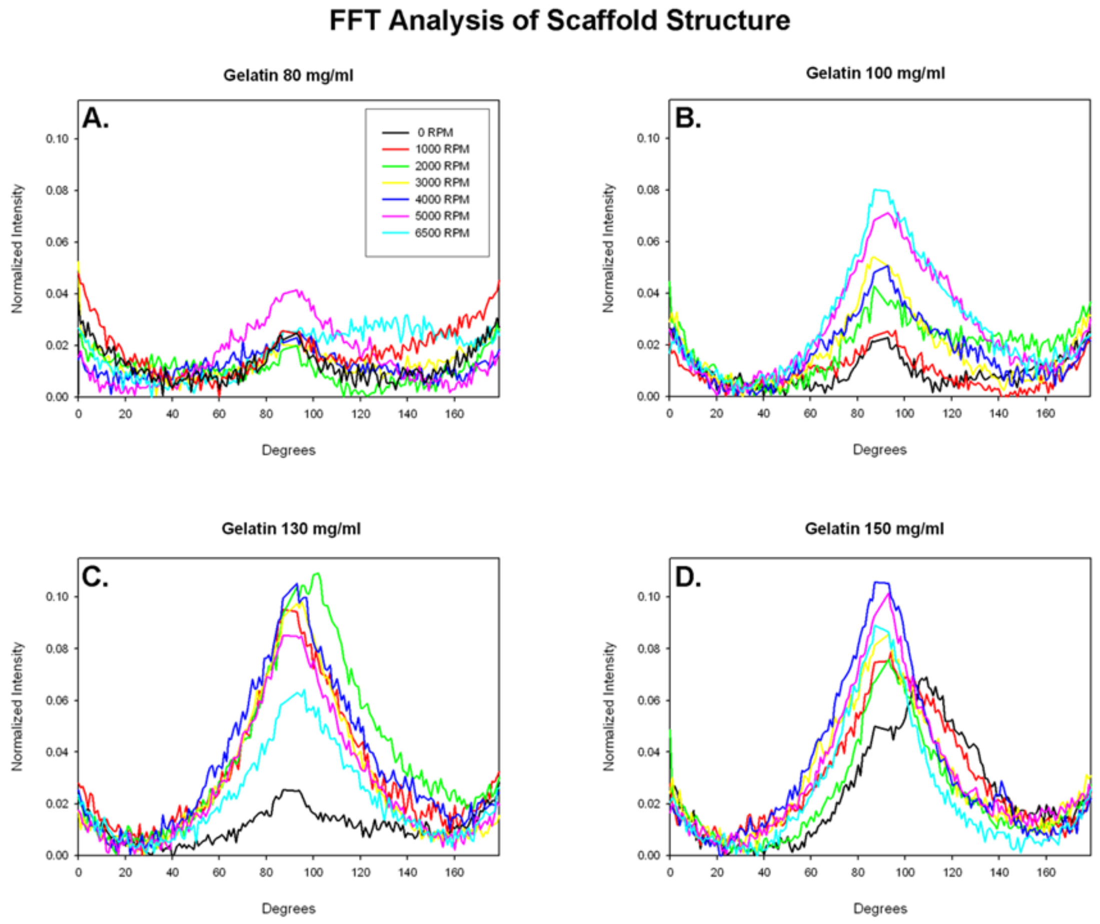

E.

Area Under the Curve				
RPM	***80 mg/ml***	***100 mg/ml***	***130 mg/ml***	***150 mg/ml***
0	1.06	0.98	1.37	3.64
1000	1.23	1.13	4.93	4.52
2000	0.71	2.38	6.10	3.38
3000	0.96	2.38	4.76	4.45
4000	1.24	2.49	5.65	5.24
5000	2.05	3.95	4.43	4.74
6000	1.63	4.20	3.30	3.73

Figure 4.3 A-E. FFT analysis of scaffold structure as a function of mandrel RPM. Scaffolds from suspensions of 80 mg/ml (A), 100 mg/ml (B), 130 mg/ml (C) and 150 mg/ml (D). Total area under the curve for frequency plots (E).

Effects of Optical Noise and Image Magnification on FFT Analysis. Images captured by brightfield (widefield) microscopy contain considerable information from outside the image plane (Z direction) and have limited resolution in the XY plane. For example, scaffolds prepared from the 80 mg/ml stock concentrations contain fibers that are at, or below, the nominal limits of resolution for a 20X, 0.40 n.a. objective (XY resolution=0.278 μm). The data images captured with this lens for FFT analysis represent a surface area of 0.35 x 0.35 mm; in images cropped to 2048 x 2048 pixels, each pixel represents approximately 1.7 x 10^{-4} mm. The fibers present in brightfield images of scaffolds prepared from the 80 mg/ml suspensions are approximately 7 pixels in diameter. Using this dimension and the pixel dimensions (1.7 x 10^{-4} mm) to "measure" these structures yields a fiber diameter of 1.1 x 10^{-3} mm or about 1 μm. SEM analysis of this type of scaffold reports an average fiber diameter of 0.29 ± 0.1 μm. This discrepancy can be attributed to the observation that fibers in a dry electrospun scaffold can act like a diffraction gradient; an effect that explains why many electrospun materials have a white appearance. The "fibers" present in a brightfield image of a scaffold prepared from a suspension concentration of 80 mg/ml actually represent birefringence of sub-resolution fibers.

To characterize how imaging artifacts might affect our FFT analysis we imaged scaffolds by brightfield (widefield) and confocal microscopy. For a representative aligned scaffold (130 mg/ml @ 25 kV, 4000 RPM) the brightfield data images produced an FFT alignment value of 0.08 units (Figure 4.4 A). A confocal average-intensity Z stack projection of this same region gave an alignment value of 0.16 units and a maximum-intensity Z stack projection gave an alignment value of 0.12 units (Figure 4.4 A). The different FFT values reported by the average-intensity and maximum-intensity Z stack projections develops from the algorithms used to produce the images. An average projection removes noise by summing and averaging pixel values in a Z stack column, "smoothing" the data set. In a maximal projection, noise is retained because the maximum pixel value in a Z stack is used to produce the final image, regardless of its source (signal or noise). We conclude from these experiments that optical (as seen in light scatter in widefield images) and electronic detector noise can degrade the absolute alignment value assigned to a scaffold by FFT analysis. However, the information that is present in a brightfield image allows the FFT approach to discern relative differences in alignment across different samples.

To characterize how image resolution and the number of fibers present in a data set impacts FFT analysis we captured a series of SEM images at different magnifications from a representative aligned scaffold (130 mg/ml @ 25 kV, 4000 RPM). Analysis of these data sets indicates that FFT alignment values remain consistent over a wide range of image magnifications (Figure 4.4 B). We note the frequency plots of these data sets become increasingly noisy above 750X, an effect that we attribute to surface structures resolved on individual fibers. The confounding effects associated with this information are substantially eliminated when a threshold filter is applied to the image prior to FFT analysis (data not shown).

Information concerning the angle at which electrospun fibers traverse any given optical image plane cannot be discerned from a brightfield, SEM or projected confocal image (which is a 3-dimensional data set collapsed into a 2-dimensional projection). This information can be recovered by sequentially examining the image planes present within a 3-dimensional confocal data set. From this type of analysis we conclude that fibers in random (Figure 4.4 C and D) and aligned scaffolds (Figure 4.4 E and F) are not dispersed to any great extent in the Z direction. The fibers of these scaffolds are deposited into layers by the electrospinning process and are substantially restricted to discrete image planes. Z distribution and fiber alignment data also is encoded in the shape and relative frequency at which different cross-sectional profiles occur in a confocal data set. The fibers of a random scaffold exhibit a round or oval profile in both the YZ and XZ directions (Figure 4.4 D). In contrast, the fibers of an aligned matrix preferentially exhibit an elongated profile in the YZ plane (the principle axis of alignment present in this particular image) and a round or oval profile in the XZ plane (Figure 4.4 F). This information can theoretically be extracted from confocal images to provide a precise map of overall scaffold anisotropy in three dimensions.

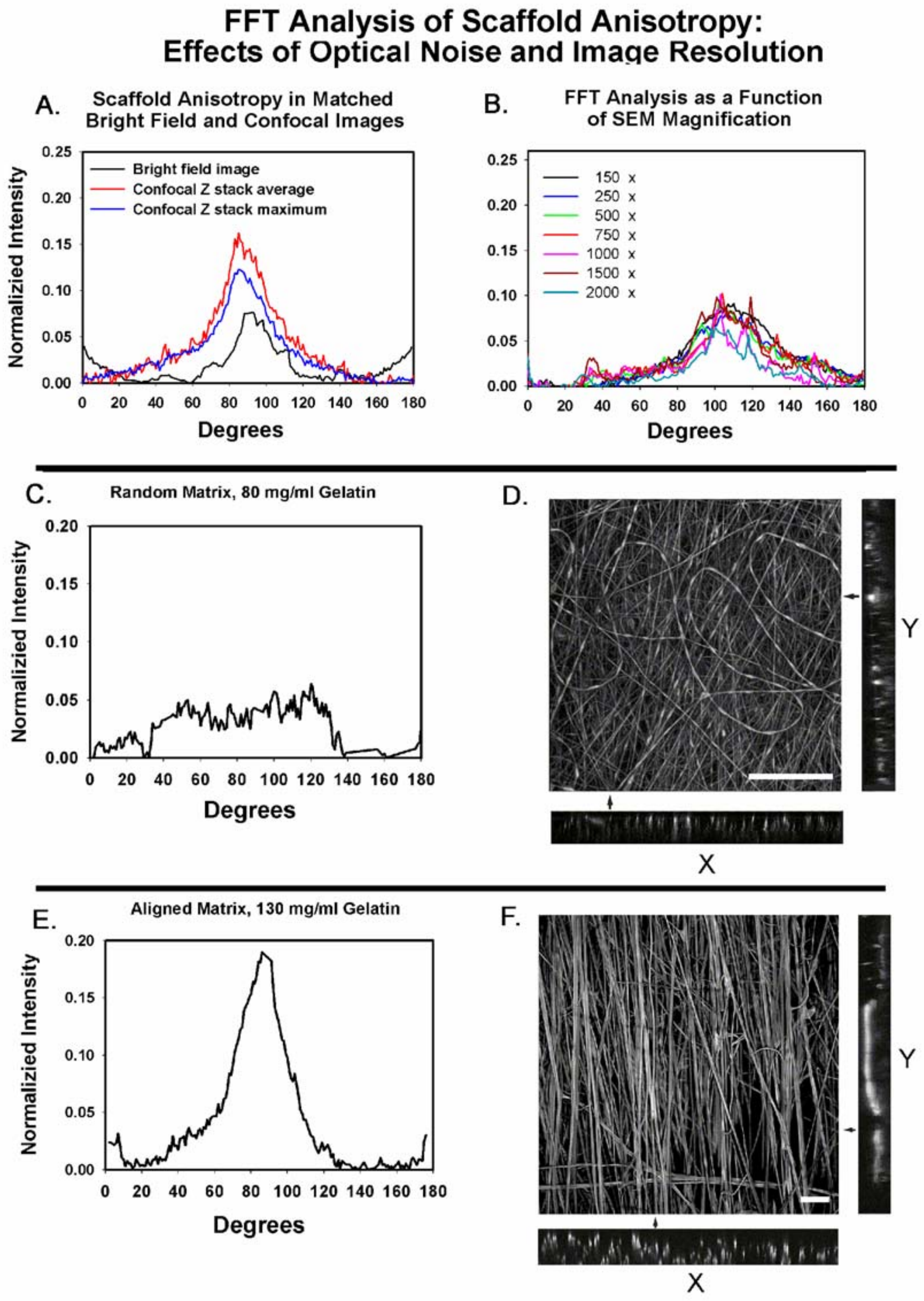
FFT Analysis of Scaffold Anisotropy:
Effects of Optical Noise and Image Resolution
A.
Scaffold Anisotropy in Matched Bright Field and Confocal Images
Normalizied Intensity
0.25
0.20
0.15
0.10
0.05
0.00
Bright field image
Confocal Z stack average
Confocal Z stack maximum
0
20
40
60
80
100
120
140
160
180
Degrees
B.
FFT Analysis as a Function of SEM Magnification
150 x
250 x
500 x
750 x
1000 x
1500 x
2000 x
Degrees
C.
Random Matrix, 80 mg/ml Gelatin
Normalizied Intensity
Degrees
D.
Y
X
E.
Aligned Matrix, 130 mg/ml Gelatin
Normalizied Intensity
Degrees
F.
Y
X

Figure 4.4 A-F. FFT analysis of brightfield, confocal Z-stack average and confocal Z-stack maximum projections of similar image fields (A). FFT analysis of SEM images as a function of SEM magnification (B). Cross sectional analysis of random (C and D) and aligned (E and F) electrospun scaffolds. Scale Bar D = 5 μm, F = 10 μm.

Materials Testing. To scale how FFT alignment values might correlate with scaffold anisotropy we conducted materials testing. Anisotropic materials can be expected to have stress and strain profiles that change as a function of the angle by which a test load is placed across the material. For an ideal and completely random matrix, stress (and strain) at failure in the parallel and the perpendicular orientations (with respect to the direction of mandrel rotation) should be identical. The ratio of the parallel to the perpendicular stress (or strain) will be equal to 1 for this type of scaffold.

For scaffolds electrospun from a concentration of 80 mg/ml and collected at 200 RPM, the ratio of average stress at failure in the parallel and perpendicular orientations was 0.86; the ratio of the average strain at failure under these conditions was 1.3 (Figure 4.5 A and B). An analysis of absolute stress at failure for the parallel and perpendicular orientations for scaffolds collected at 2000, 4000, and 6000 RPM failed to detect any statistical differences in the data sets (Figure 4.5 C and D). This lack of directional bias is consistent with a structure composed of random elements.

For scaffolds electrospun from 100 mg/ml suspensions the ratio of the average stress at failure in the parallel and perpendicular orientations increased modestly and sequentially as a function of mandrel RPM (Figure 4.5 A). At low RPM (200 and 2000) peak stress was higher in the perpendicular orientation ($P<0.05$). As RPM increased, peak stress became increasingly biased in the parallel orientation ($P<0.02$) (Figure 4.5 A and C). The ratio of peak strains at failure in the parallel and perpendicular orientations decreased (Figure 4.5 B). However, statistical analysis of the absolute values for these data sets failed to detect any directional bias in the strain properties of these scaffolds (Figure 4.5 B and D).

Scaffolds electrospun from the 130 mg/ml suspensions exhibited evidence of anisotropy under all of the conditions that we tested ($P<0.03$, Figure 4.5 A and C), indicating that a degree of alignment is induced even at nominal mandrel RPM. There was a distinct change in the ratio of the peak stresses (Figure 4.5 A) and the ratio of the peak strains at failure (Figure 4.5 B) between 4000 and 6000 RPM. Scaffolds prepared from the 150 mg/ml suspensions exhibited poor structural integrity under the electrospinning conditions used in this study and were damaged during removal from the mandrel. As a result, the material properties of these scaffolds were not tested.

In summary, the materials testing data suggests that an FFT alignment value of 0.05 units or greater corresponds to the evolution of scaffold anisotropy. Scaffolds that exceed this alignment value exhibit an orientation bias in materials testing. In contrast, scaffolds with FFT values below this threshold appear to be random in nature. The use of a strain extensometer to determine the strain properties of a soft tissue is a less than ideal approach; the weight of the testing apparatus can distort the resulting strain values. Given the results of our study and the potential technical limitations in measuring strain we believe the measured stress properties of an electrospun scaffold more accurately reflect the anisotropic properties of these materials. In our experiments the stress measurements are less susceptible to instrument induced error.

Material Properties of Electrospun Gelatin

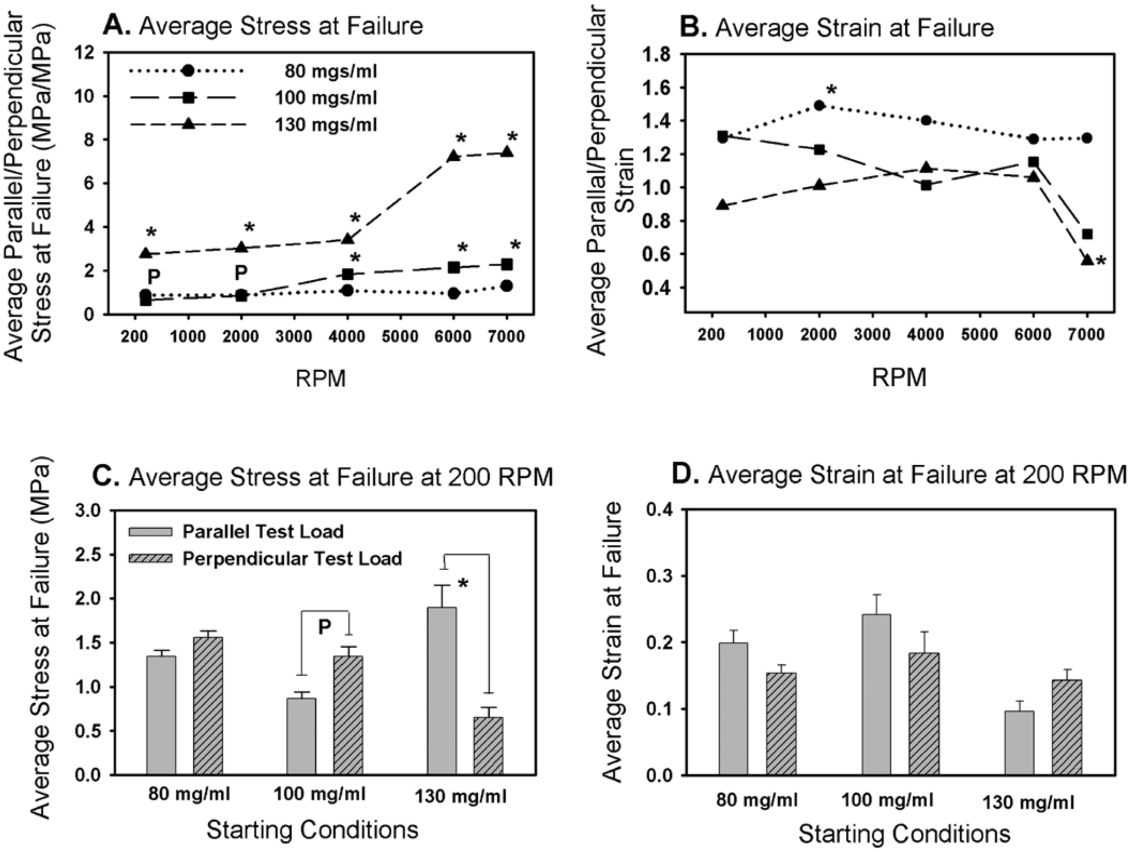

E

	Stress (MPa)					
	80 mg/ml		**100 mg/ml**		**130 mg/ml**	
RPM	*Parallel*	*Perpendicular*	*Parallel*	*Perpendicular*	*Parallel*	*Perpendicular*
200	1.3	1.6	0.90	1.3	2.1	0.65
2000	1.6	1.7	0.86	1.0	2.0	0.66
4000	1.5	1.4	1.7	0.92	1.6	0.49
6000	1.3	1.4	2.3	1.0	2.7	0.40
7000	1.3	1.0	2.0	0.90	1.7	0.23

F

	Strain					
	80 mg/ml		**100 mg/ml**		**130 mg/ml**	
RPM	*Parallel*	*Perpendicular*	*Parallel*	*Perpendicular*	*Parallel*	*Perpendicular*
200	0.20	0.15	0.24	0.18	0.09	0.11
2000	0.25	0.17	0.15	0.12	0.16	0.16
4000	0.20	0.16	0.18	0.26	0.09	0.08
6000	0.20	0.17	0.13	0.10	0.17	0.17
7000	0.19	0.15	0.19	0.24	0.09	0.16

Figure 4.5 A-F. Material properties as a function of mandrel rotation. Ratio (in the parallel to perpendicular orientations) of stress (A) and strain (B) at failure. Average stress (C) and strain (D) at failure in scaffolds deposited at 200 RPM. * = bias in the parallel orientation, P = bias in the perpendicular orientation ($P<0.05$). Error bars = ± standard error. Table E=average stress values, F=average strain values as a function of starting concentration and direction of testing.

DISCUSSION

Fiber Diameter and Pore Area. We have examined how starting conditions regulate fiber diameter, pore area and the material properties of electrospun gelatin. Scaffolds were prepared from starting concentrations of 80, 100, 130 and 150 mg gelatin/ml TFE; this represents the range of conditions that produced useful scaffolds. At starting concentrations of less than 80 mg/ml, scaffolds of gelatin are composed of 200 - 300 nm diameter fibers, exhibit poor structural integrity and are difficult to manually manipulate [15]. Conversely, scaffolds electrospun from stock concentrations containing 150 mg/ml gelatin, or greater, retain solvent and are difficult to recover for analysis.

In our experiments fiber diameter did not vary as a simple linear function of the starting concentration of gelatin (Figure 4.2 B). There are several potential explanations to account for this result. Theoretically, the viscosity of the starting solution/suspension is the variable most closely linked to fiber cross-sectional diameter in the electrospinning process [118][126-128]. However, viscosity evolves from properties that are intrinsic to a specific solvent system and the identity, concentration and extent of polymer chain entanglements (and the degree of solubility of a given polymer) present at the onset of electrospinning. Viscosity is further modulated by ambient conditions (temperature, humidity *etc*.). These fundamental variables are coupled with the rate of polymer delivery to the electric field, the ionic composition of the solution/suspension, and the electrospinning voltage to regulate the stability of the Taylor cone, the trajectory of the charged jet and the dimensions of the developing fiber. We suspect there is a mismatch between one of these coupled electrospinning parameters; multiple charged jets have been observed to develop and episodically collapse when electrospinning from our 100 mg/ml suspensions. Removing either the 100 or 130 mg/ml data sets dramatically improves our regression analysis results when we examine how fiber diameter varies as a function of starting concentration or viscosity. Removing the 100 mg/ml data provides a first-order R^2 value of 0.68 and a second-order R^2 value of 0.86; removing the 130 mg/ml data generates a first-order R^2 value of 0.75. We believe that a re-assessment of data sets generated with other polymer systems may reveal similar discontinuities in the theoretical relationships that exist between fiber diameter and solution viscosity (a variable that has not been commonly reported) [106].

Mandrel Rotation. For each starting concentration, fiber diameter remained constant over a wide range of mandrel RPM (Figure 4.2). If the mandrel acted like a spool, and scaffold alignment was induced by fiber winding, average fiber diameter would be expected to decrease as a function of mandrel RPM. This thinning effect has been observed in electrospinning systems where a rotating disk mandrel with a high surface velocity is used as a target [110].

Fiber Alignment and Scaffold Anisotropy. As judged from this preliminary study, the FFT can be used to predict scaffold anisotropy over a wide range of imaging conditions. It is important to note, however, that because electrospinning produces sub-micron fibers that are often below the resolution of a light microscope objective, images of these fibers are generated through birefringence. Although our data suggests this type of image produces useful FFT data, the effects of image resolution on FFT output should be calibrated and verified by high-resolution analysis using confocal microscopy and/or SEM (see Figure 4.4). SEM images are clearly amenable to analysis by FFT, but this approach must assume a uniform distribution of fibers throughout the cross-sectional diameter of the scaffold. We are continuing to explore the limits of FFT analysis in the characterization of scaffold structure.

Routine microscopic examination of our scaffolds identified evidence of preferential fiber alignment under a variety of different electrospinning conditions (*e.g.* Figure 4.3). FFT alignment values of greater than 0.05 units were correlated with the onset of directional bias in the material properties (Figure 4.5). Scaffolds that did not meet this criterion failed to exhibit overt visual evidence of anisotropy or the stress/strain values normally expected of a material composed of aligned elements. The correlation between the materials testing data and the degree of scaffold anisotropy, as determined by FFT, indicate that our optical measurements can be used to predict scaffold alignment on a relatively large scale (*i.e.* alignment is not just a local phenomena detected by FFT analysis).

CONCLUSION

Anisotropy in an electrospun scaffold develops from a complex set of variables. A surprising degree of anisotropy can be present in an electrospun scaffold composed of relatively large diameter fibers that have been collected at modest rates of mandrel rotation. These results clearly demonstrate that it is necessary to take into account the relative degree of fiber alignment present in an electrospun material when attempting to compare the material properties of constructs composed of different fiber diameters. Our data also underscore the central role that macroscopic architectural features can play in regulating the material properties of the native ECM. Additional experimentation will be necessary to determine if more subtle changes in FFT alignment values can be correlated with the evolution of specific material properties and/or features that can control cell phenotype in an electrospun tissue-engineering scaffold. By tailoring scaffold anisotropy in an electrospun material it may be possible to provide contact guidance cues to cells and more closely mimic the material properties of native structures [129][130]. FFT analysis is a potentially valuable method for quantifying alignment, confirming the reproducibility of nano-manufacturing processes and examining the biological consequences of scaffold structure.

CHAPTER 5 Modulation of Material Properties in Electrospun Scaffolds

Preface: The following manuscript appeared in Acta Biomaterialia, 2007, volume 3, pages 651-661 [63]. The work included demonstrates how changes in fiber diameter, scaffold architecture and angle of testing modulate the material properties of an electrospun scaffold. The fast Fourier transform was used to measure the relative fiber alignment in the scaffolds. These experiments were conducted as an extension of the manuscript included in chapter 4 in order to better understand the role fiber alignment plays in establishing the material properties of an electrospun scaffold. These results are critical to the understanding of how structure and architecture contribute to the overall properties of a scaffold; understanding and characterizing these elements is crucial for the facilitation of native extracellular matrix recapitulation.

Incremental Changes in Anisotropy Induce Incremental Changes in the Material Properties of Electrospun Scaffolds

CE Ayres[1], GL Bowlin[1], R Pizinger[3], LT Taylor[1], CA Keen[3] and DG Simpson[2]

[1]Department of Biomedical Engineering
Virginia Commonwealth University
Richmond, VA 23284

[2]Department of Anatomy and Neurobiology
Virginia Commonwealth University
Richmond, VA 23298

[3]School of Medicine
Virginia Commonwealth University
Richmond, VA 23298

ABSTRACT

Electrospinning can be used to selectively process a variety of natural and synthetic polymers into highly porous scaffolds composed of nano-to-micron diameter fibers. This process shows great potential as a gateway to the development of physiologically relevant tissue engineering scaffolds. In this study we examine how incremental changes in fiber alignment modulate the material properties of a model scaffold. We prepared electrospun scaffolds of gelatin composed of varying fiber diameters and degrees of anisotropy. The scaffolds were cut into a series of dumbbell shaped samples in the longitudinal, perpendicular and transverse orientations and the relative degree of fiber alignment, as measured by the fast Fourier transform (FFT) method, was determined for each sample. We measured peak stress, peak strain and the modulus of elasticity as function of fiber diameter and scaffold anisotropy. Fiber alignment was the variable most closely associated with the regulation of peak stress, peak strain and modulus of elasticity. Incremental changes, as judged by the FFT method, in the proportion of fibers that were aligned along a specific axis induced incremental changes in peak stress in the model scaffolds. These results underscore the critical role that scaffold anisotropy plays in establishing the material properties of an electrospun tissue engineering scaffold and the native extracellular matrix.

INTRODUCTION

The electrospinning process shows great potential as a gateway for the development and fabrication of physiologically relevant tissue engineering scaffolds [15][66][131]. A variety of native proteins [13][61][62], synthetic polymers [105][106][110] and blends of native and synthetic materials [43] can be selectively processed and electrospun into highly porous scaffolds composed of small diameter fibers. The physical, biochemical, biological and material properties of this unique class of materials can be regulated at several sites in the production process. Physical properties, including fiber diameter and pore dimension, can be regulated by controlling the composition of the electrospinning solvent and the identity, concentration, and/or degree of chain entanglements (viscosity) present in the starting polymer(s) [117][118]. The structural profile of the selected materials can even be modulated after the completion of the electrospinning process through nanofiber self-assembly events [132]. The biochemical profile of scaffolds can be manipulated through the addition of soluble growth factors [130] and other pharmaceuticals [119][133] during and/or after the electrospinning process. Biological properties can be further tailored to specific applications by controlling fiber identity and alignment.

Emerging evidence suggests that fiber alignment and overall scaffold anisotropy play a critical role in determining the material properties of electrospun materials [14][106][108]. However, efforts to examine how scaffold material properties develop as a function of these characteristics have been limited; developing an objective, quantitative measure of fiber alignment is a challenging task. In previous studies we adapted and used the fast Fourier transform (FFT) to measure the relative degree of fiber alignment present in an electrospun scaffold [14][83]. We observed distinct material properties as scaffold anisotropy reached a critical threshold and here we extend our preliminary observations to more precisely define this threshold. In this study we examine how fiber diameter and specific degrees of fiber alignment, as determined by the FFT method, interact with the testing angle to dictate the material properties of an electrospun scaffold.

To explore how fiber alignment regulates material properties, calfskin gelatin scaffolds of varying fiber diameters are electrospun onto a rectangular, grounded mandrel. Differing degrees of fiber alignment can be induced by rotating the mandrel at a constant rate between 0 and 6000 RPM [119]. Scaffolds are cut into dumbbell shaped samples (for materials testing purposes) in the longitudinal, perpendicular or transverse orientations. From these samples the relative degree of fiber alignment, as measured by the FFT method, is determined. The samples are then tested to failure using a materials testing machine. From the data it appears that fiber alignment is the variable most closely associated with changes in scaffold material properties, increasing the proportion of fibers aligned along a specific axis induces incremental changes in peak stress. These results emphasize the central role that scaffold anisotropy plays in determining the material properties of the native extracellular matrix and engineered scaffolds.

MATERIALS AND METHODS

Electrospinning. Reagents were purchased from Sigma Aldrich (St. Louis, MO) unless noted. Gelatin was suspended (120, 150 and 180 mg/ml) and agitated in 2,2,2 trifluoroethanol (TFE) for 24 hr. Electrospinning suspensions were loaded into a 20 ml Becton Dickinson syringe capped with an 18 gauge blunt tipped needle. The air gap distance between the source suspension and the grounded mandrel was set to 20 cm. A Harvard perfusion pump was used to meter the delivery of the electrospinning suspensions to the electric field. The positive output lead of a high voltage supply (Spellman CZE1000R; Spellman High Voltage Electronics Corporation) was attached by an alligator clip to the blunt tipped needle. For a detailed schematic of the electrospinning system, see reference 13. Electrospinning was conducted at an accelerating voltage of 25 kV. The rate of solvent/polymer delivery was set at the maximal rate that did not induce dripping from the tip of the syringe. A stainless steel rectangular mandrel (75 x 20 x 6 mm) was used as a grounded target.

The target mandrel was regulated to rotate between 0 to 6000 RPM to induce varying degrees of alignment in the electrospun scaffolds. A digital stroboscope (Shimpo Instruments DT3-11A) was used to continuously monitor the RPM of the target mandrel. Under the conditions of this study, fiber diameter remained constant over the range of mandrel RPM used to collect the scaffolds (not shown, see reference 14). Samples were stored in a desiccation chamber to limit hydration prior to analysis.

Scanning Electron Microscopy. Average fiber diameter was determined from samples processed for conventional Scanning Electron Microscopy (SEM, Jeol JSM-820). Dry, unfixed electrospun scaffolds were sputter coated with gold for imaging. SEM images were captured on Polaroid film, digitized via a flatbed scanner and analyzed with NIH ImageTool (UTHSCSA version 3). Average fiber diameter was determined from measurements taken perpendicular to the long axis of the fibers within representative microscopic fields (25 measurements per field). All measurements were calibrated from size bars incorporated into the SEM images at the time of capture (N=3 from independent experiments).

Light Microscopy. The scaffolds were imaged using a Nikon TE300 microscope equipped with a Nikon DXM 1200 digital camera. Bright Field images (3840 x 3072 pixels) were captured with a 20X 0.40 n.a. brightfield objective lens. All images were archived as .TIF files.

FFT. As described in detail in a previous study, the FFT was used to evaluate relative fiber alignment in electrospun scaffolds [14]. For a complete description of this method see reference 83. The FFT function converts information present in an optical data image from a “real” domain into a mathematically defined “frequency” domain. The resulting FFT output image contains grayscale pixels that are distributed in a pattern that reflects the degree of fiber alignment present in the original data image. A graphical depiction of the FFT frequency distribution is generated by placing an oval projection on the FFT output image and conducting a radial summation of the pixel intensities for each angle between 0 and 360°, in one degree increments. The pixel intensities are summed along each radius and then plotted as a function of the angle of acquisition (position of the radial projection on the oval profile), usually between 0 and 180° (FFT data is symmetric so a pixel summation to 360° is unnecessary). The degree of alignment present in the original data image is reflected by the height and overall shape of the peak present in this plot. The position of the peak on the plot reports the principal axis of alignment.

For analysis, grayscale, 8-bit .TIF brightfield microscopic images were cropped to 2048 x 2048 pixels. FFT analysis was conducted using ImageJ software (NIH, http://rsb.info.nih.gov/ij) supported by an oval profile plug-in (authored by William O'Connnell). The FFT data was normalized to a baseline value of 0 and plotted in arbitrary units ranging from 0 to 0.1.

Materials Testing. After FFT analysis, samples were subjected to materials testing using a Bionix 200 Mechanical Testing Systems instrument equipped with a 50 N load cell (MTS Systems Corp, Eden Prairie, MN). Scaffolds were removed from the target mandrel and laid flat to maximize surface area for sample cutting. Samples were cut into a series of dumbbell shaped samples (2.67 mm wide with a gauge length of 7.49 mm). Samples were cut in three orientations: longitudinal (the length of the sample cut parallel to the direction of mandrel rotation), perpendicular (the length of the sample cut perpendicular to the direction of mandrel rotation) and transverse (the length of the sample cut at a 45^0 angle to the direction of mandrel rotation). Each scaffold was large enough to produce a minimum of 4 samples in each of the three orientations. Each specimen was assigned a unique serial number to allow for tracking. Specimen thickness was determined with a Mitutoyo IP54 digital micrometer (Mitutoyo American Corp; Aurora, IL). Scaffolds were tested to failure using an extension rate of 10 mm/min to evaluate the stress, strain and modulus of elasticity as a function of electrospinning condition (e.g. starting concentration), average fiber diameter and relative fiber alignment (as reported by FFT analysis).

Statistical Evaluation. One-way ANOVA was used to screen the morphometric fiber diameter data sets. A Tukey test was used in the *post hoc* analysis of these data sets. Two-way ANOVA was used to screen for the effects of fiber diameter, testing angle (i.e. longitudinal, perpendicular and transverse) and interactions between these variables. Two-way ANOVA was also used to screen for the effects of fiber orientation, testing angle and interactions between these variables. For this analysis (see Figures 5.6 and 5.7) data was sorted by the angle of testing (*i.e.* longitudinal, perpendicular and transverse) and then by the FFT alignment value. The alignment values for each individual scaffold were rounded down and the data sets were binned in 0.01 FFT units (Figure 5.5 A-C). The binned data sets were then analyzed to examine how the degree of alignment and angle of testing impact scaffold material properties. A Tukey Test was also used in the *post hoc* analysis of these data sets. For all pairwise comparisons, significance was defined at $P<0.05$. Actual P values are presented in Table 5.2, Tables I-III. Total N=12-18 samples for each fiber diameter and orientation.

RESULTS

Fiber Characterization. Screening the morphometric data sets indicated that three distinct classes of fibers were generated from the different starting concentrations of gelatin ($P<0.001$). Representative SEM images are illustrated in Figure 5.1. The average cross-sectional fiber diameter of each scaffold increased two-fold with every 30 mg/ml increase in starting concentration. Starting concentrations of 120, 150 and 180 mg/ml produced average cross-sectional fiber diameters of 1.59, 3.46 and 6.93 μm, respectively. The interrelatedness of starting concentration, suspension viscosity and average fiber diameter in our electrospinning system is documented in Figure 5.1 D-F. Fiber diameter remained constant over all mandrel RPM used in this study.

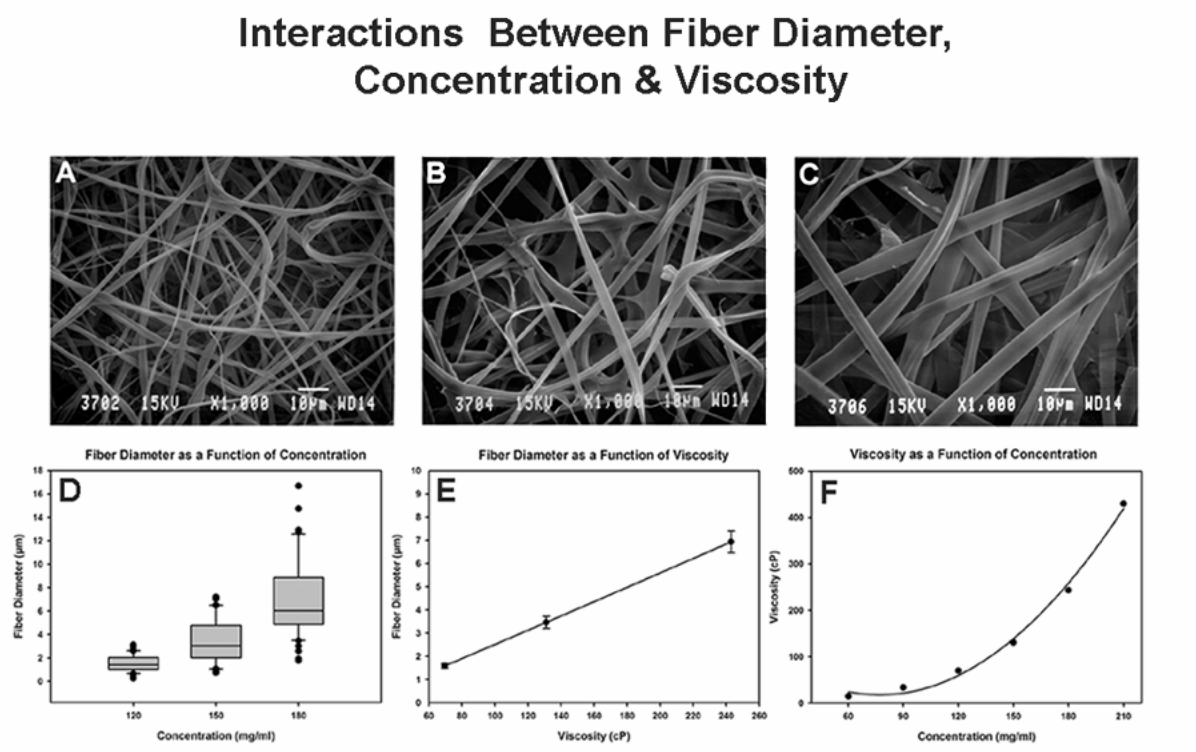

Figure 5.1 A-F. Scanning electron micrographs of scaffolds produced from starting concentrations of 120 (A), 150 (B) and 180 mg/ml (C). Interactions between fiber diameter, concentration and viscosity: fiber diameter as a function of concentration (D), fiber diameter as a function of viscosity (E) and viscosity as a function of concentration (F).

Material Properties: Longitudinal Orientation. The material properties of the electrospun scaffolds are summarized in Figures 5.2-5.5. The samples were sorted and plotted solely by the angle at which the scaffolds were tested (i.e. longitudinal, perpendicular or transverse). The data sets include material properties of scaffolds composed of all fiber diameters as a function of the FFT alignment value.

Samples cut and tested in the longitudinal orientation exhibited increased levels of peak stress as a function of increasing FFT alignment value (Figure 5.2 A). In addition, a distinct change in material properties occurred at an FFT alignment value of approximately 0.05 units. Specific peak stress values for different conditions are summarized in Table 5.1, Table I. Peak strain was highly variable over the FFT values that we examined and no relationship was evident between the peak strain and the FFT alignment value (Figure 5.2 B & Table 5.1, Table II). Analogous to the peak stress for this test group, the modulus of elasticity increased as a function of the FFT alignment value (Figure 5.2 C, Table 5.1 Table III).

Material Properties: Perpendicular Orientation. Samples cut and tested in the perpendicular orientation exhibited lower and more uniform peak stress values than scaffolds tested in the longitudinal orientation (compare Figures 5.2 A with Figure 5.3 A, Table 5.1 Table I). Peak strain values were similar to those reported for the longitudinal test group (compare Figures 5.2 B and 5.3 B, Table 5.1 Table II). The modulus of elasticity exhibited a modest decrease as a function of increasing FFT alignment value (Figure 5.3 C, Table 5.1 Table III).

Material Properties: Transverse Orientation. Samples cut and tested in the transverse orientation exhibited material properties that were similar to the material properties of the perpendicular samples (compare Figures 5.3 and 5.4). Peak stress values were comparable for all samples tested across all FFT alignment values (Figure 5.4 A, Table 5.1, Table III). Peak strain values (Figure 5.4 B) and the modulus of elasticity (Figure 5.4 C) were similar to those of samples tested in the perpendicular orientation (Table 5.1 Table III).

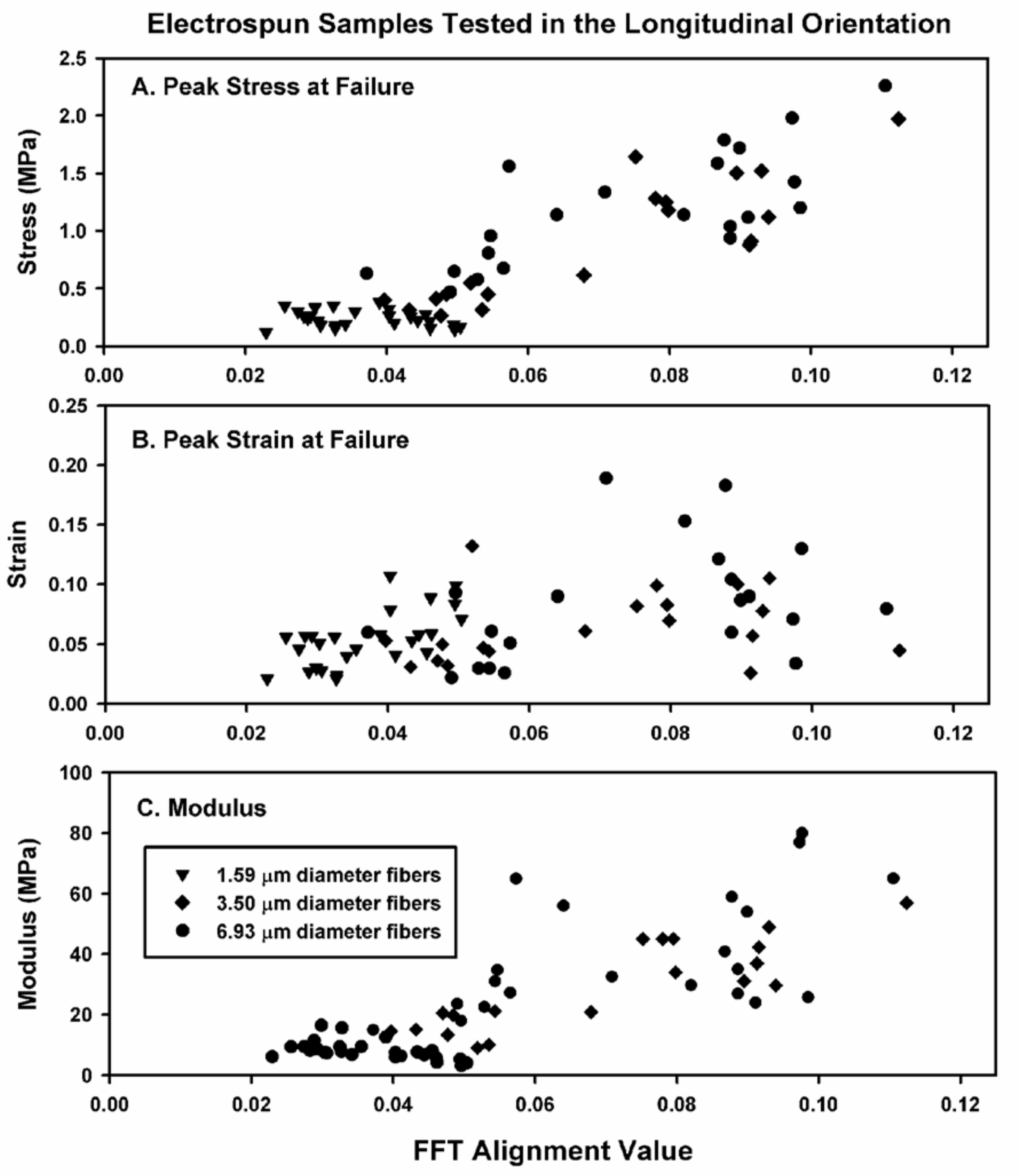

Figure 5.2 A-C. Summary of the peak stress (A), peak strain (B) and modulus of elasticity (C) as a function of the absolute FFT alignment value for each electrospun scaffold tested in the longitudinal orientation. Linear regression analysis for the FFT alignment value and the peak stress (R^2=0.760), peak strain (R^2=0.194) and modulus of elasticity (R^2=0.233). Subdividing and analyzing the data by average fiber diameter did not alter the results (not shown).

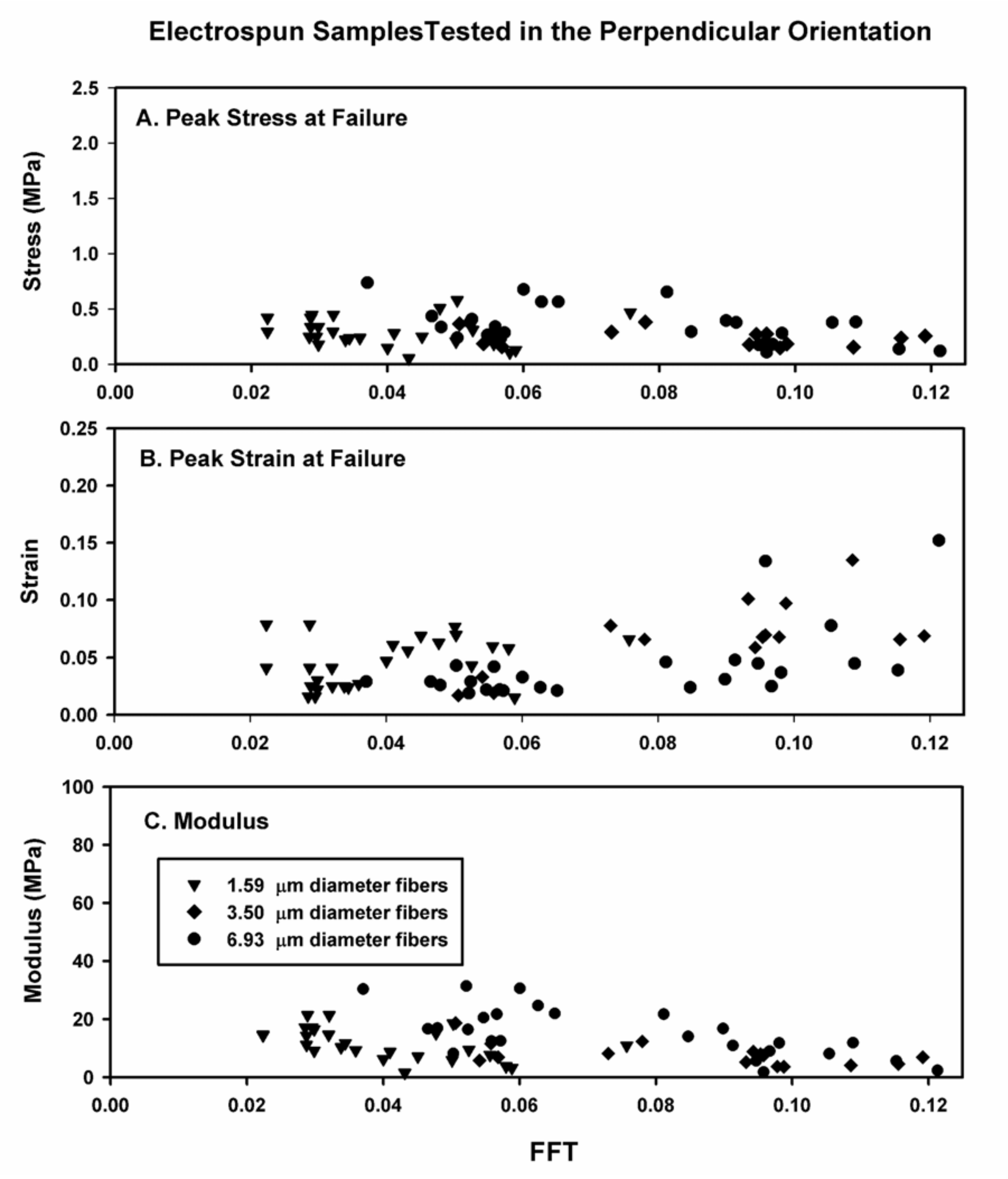

Figure 5.3 A-C. Summary of the peak stress (A), peak strain (B) and modulus of elasticity (C) as a function of the absolute FFT alignment value for each electrospun scaffold tested in the perpendicular orientation. Linear regression analysis for the FFT alignment value and the peak stress (R^2=0.048), peak strain (R^2=0.288) and modulus of elasticity (R^2=0.185). Subdividing and analyzing the data by average fiber diameter did not alter the results (not shown).

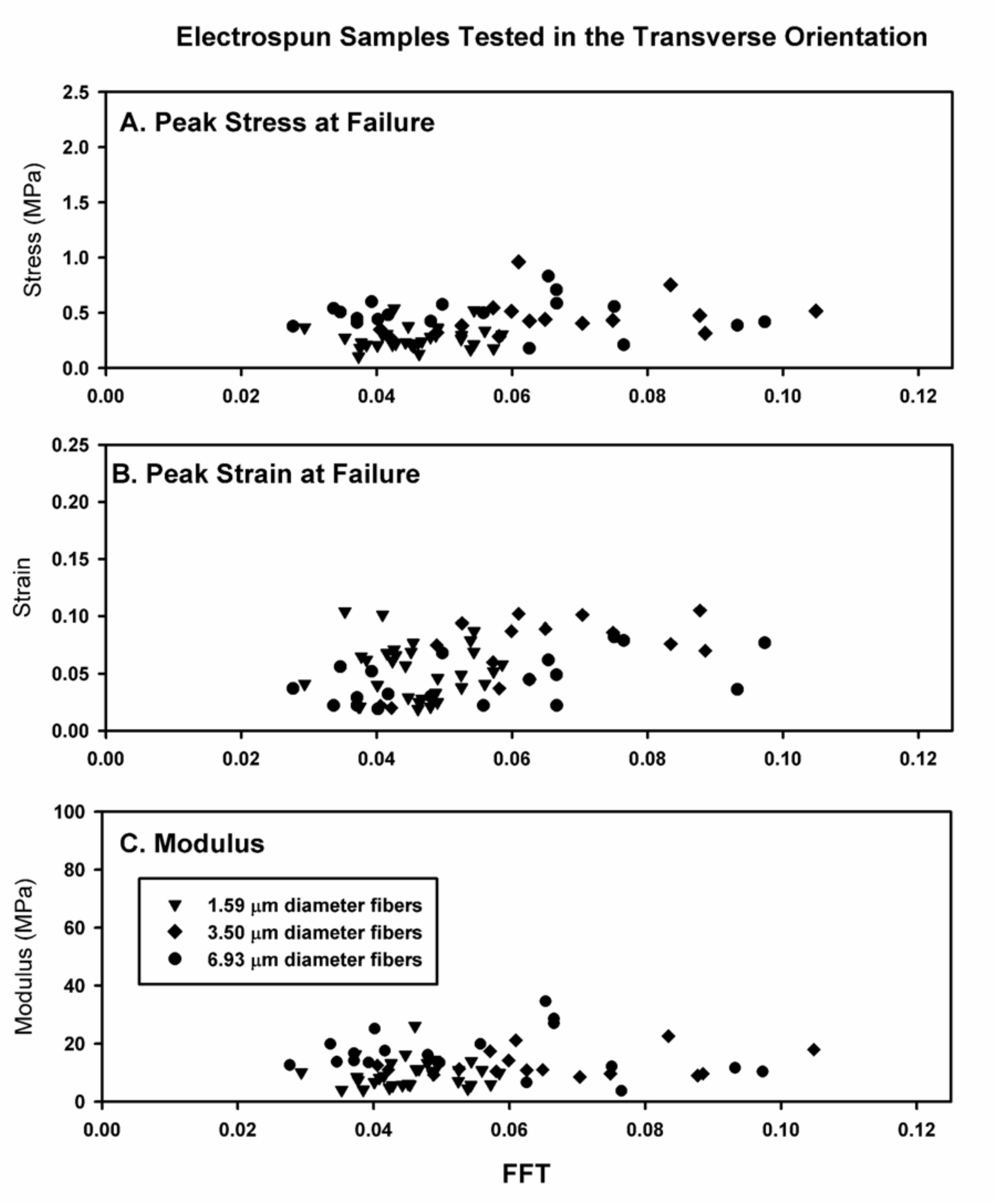

Figure 5.4 A-C. Summary of the peak stress (A), peak strain (B) and modulus of elasticity (C) as a function of the absolute FFT alignment value for each electrospun scaffold tested in the transverse orientation. Linear regression analysis for the FFT alignment value and the peak stress (R^2=0.080), peak strain (R^2=0. 198) and modulus of elasticity (R^2=0.149). Subdividing and analyzing the data by average fiber diameter did not alter the results (not shown).

Table I. Peak stress	Maximum Peak Stress	Average Peak Stress	Average Peak Stress FFT<0.05	Average Peak Stress FFT>0.05
TESTING ORIENTATION				
Longitudinal	1.90 MPa	0.72 MPa	0.29 MPa	1.14 MPa
Perpendicular	0.74 MPa	0.30 MPa	0.32 MPa	0.29MPa
Transverse	0.96 MPa	0.38 MPa	0.32 MPa	0.43 MPa

Table II. Peak strain	Maximum Peak Strain	Average Peak Strain	Average Peak Strain FFT<0.05	Average Peak Strain FFT>0.05
TESTING ORIENTATION				
Longitudinal	0.19	0.07	0.05	0.08
Perpendicular	0.15	0.05	0.04	0.06
Transverse	0.11	0.06	0.05	0.09

Table III. Modulus	Maximum Modulus	Average Modulus	Average Modulus FFT<0.05	Average Modulus FFT>0.05
TESTING ORIENTATION				
Longitudinal	80.00 MPa	9.33 MPa	10.50 MPa	37.40 MPa
Perpendicular	31.40 MPa	12.01 MPa	12.01 MPa	11.09 MPa
Transverse	34.58 MPa	12.44 MPa	11.76 MPa	13.24 MPa

Table 5.1. Summary of materials testing data presented in Figures 2, 3 and 4.

Intermediate Summary. Initial examination of these data sets suggested that the calculated material properties of an electrospun scaffold may be governed by a complex interaction between fiber size (cross sectional diameter), degree of alignment present (FFT alignment value) and angle of testing (longitudinal, perpendicular or transverse). Next, we systematically examined how each of these variables modulated the peak stress of an electrospun scaffold. We elected to concentrate on peak stress because it is most closely associated with the evolution of anisotropy in an electrospun scaffold [14].

Effects of Fiber Diameter and Testing Angle. Analysis of fiber diameter and angle of testing indicated that peak stress increased as a function of fiber diameter (Figure 5.5 A, $P<0.006$) and varied as a function of testing angle (Figure 5.5 B, $P<0.039$). Peak stress was highest in scaffolds tested in the longitudinal orientation, intermediate in scaffolds tested in the transverse orientation and lowest in scaffolds tested in the perpendicular orientation.

Under specific conditions, the 2-way ANOVA detected interactions between fiber diameter and angle of testing ($P<0.001$). There was no directional bias in scaffolds prepared from the 120 mg/ml starting concentrations (average fiber diameter = 1.59 μm). This result is consistent with scaffolds composed of randomly oriented fibers; peak stress (and strain) should be uniform in each direction. Scaffolds prepared from the 150 mg/ml starting concentrations (average fiber diameter = 3.46 μm) exhibited three distinct patterns of stress as a function of the testing angle (Figure 5.5 C, $P<0.002$). The scaffolds prepared from the 180 mg/ml concentrations (average fiber diameter = 6.93 μm) exhibited higher peak stresses in the longitudinal orientation than in the transverse and perpendicular orientations (Figure 5.5 C, $P<0.001$). Samples from this suspension tested in the perpendicular and transverse orientations could not be distinguished from one another.

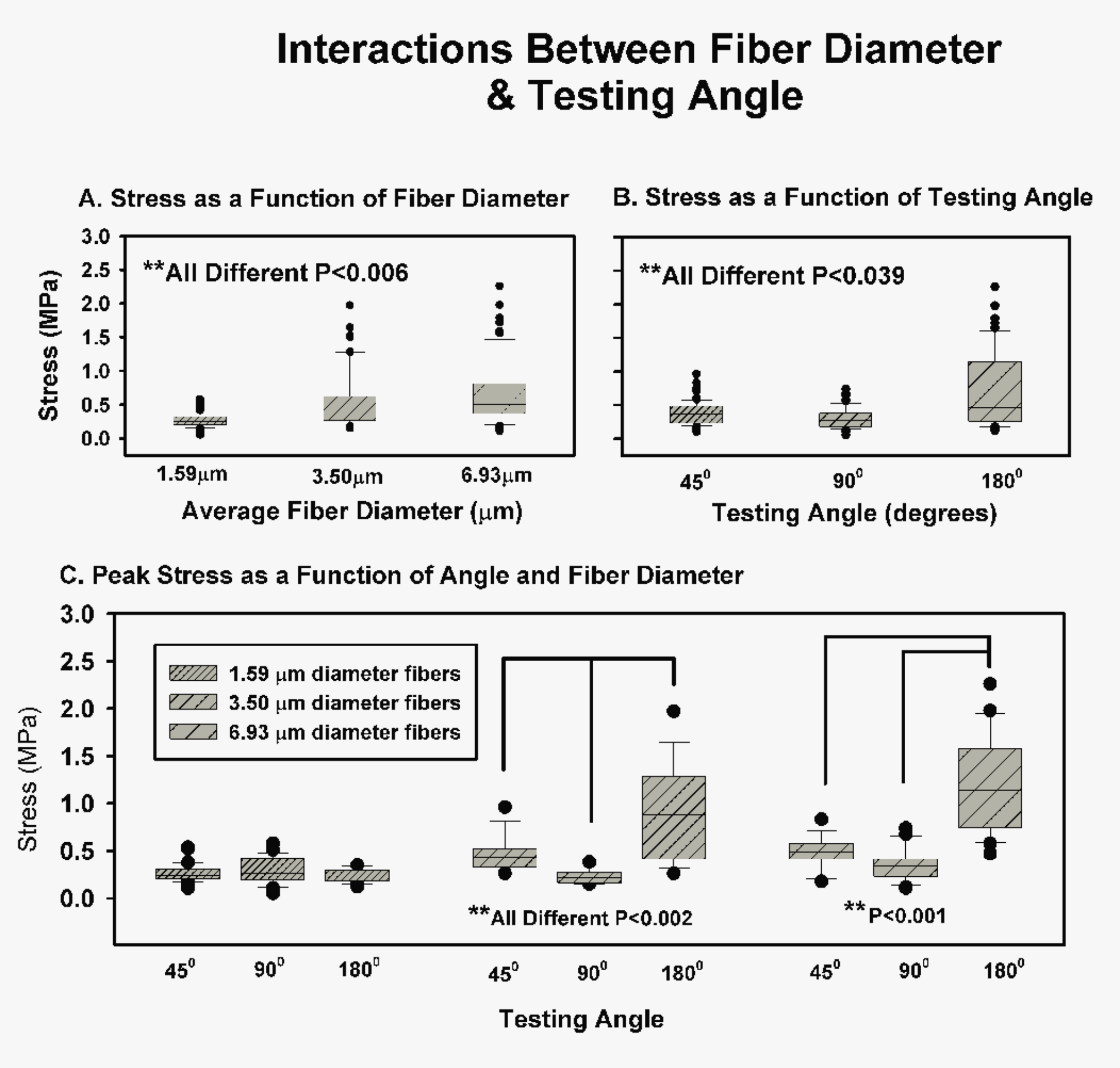

Figure 5.5 A-C. Contributions of fiber diameter (A), testing angle (B) and interactions between these variables in the determination of peak stress (C). Scaffolds composed of different fiber diameters (A, P<0.006) and examined at different testing angles (B, P<0.039) had unique peak stress properties. Specific interactions existed between these variables in scaffolds composed of 2.27 μm and 4.68 μm diameter fibers (C). All data ± S.E.

Effects of Fiber Alignment and Testing Angle. Analysis of fiber alignment and angle of testing indicated that peak stress was greater in the longitudinal orientation with respect to the perpendicular and transverse orientations (P<0.001), which were indistinguishable from each other (Figure 5.6 A-C). An interaction between the binned FFT alignment value and the angle of testing was also detected (P<0.001). These interactions were primarily evident in the longitudinal test samples.

Samples exhibiting FFT alignment values of less than 0.05 units did not exhibit evidence of directional bias in materials testing. The peak stress of the scaffolds at each angle of testing and binned between 0.02 and 0.04 units was identical (Figure 5.6 A & Table 5.2, Table I). These results are consistent with a material composed of random elements. Statistical analysis suggests that anisotropic material properties begin to develop in the longitudinal test group at a binned FFT alignment value of 0.05 units. This value also marks the threshold where the peak stress of the longitudinal test group diverges and can be distinguished from the peak stress present in the perpendicular and transverse test groups (P<0.05). Beyond this threshold, detectable changes in peak stress developed as a function of 1-2 bins in the longitudinal test group (Table 5.2. Table I).

Peak strain values as a function of the binned FFT alignment value are summarized in Figure 5.6 B and Table 5.2, Table II. Examining the effects of angle of testing in terms of the binned FFT alignment value indicated that peak strain was different across each of the three test groups (longitudinal vs. perpendicular vs. transverse; P<0.001). An interaction between the FFT alignment value and the angle of testing was also present in this analysis (P<0.001). In addition, there were specific interactions within each of the test groups as a function of FFT alignment value (Table 5.2, Table II). However, differences across the FFT alignment values for peak strain were less consistent than for the peak stress values for the same test groups.

The modulus of elasticity values as a function of the binned FFT alignment value are summarized in Figure 5.6 C and Table 5.2, Table III. Examining the effects of angle of testing in terms of the binned FFT alignment value indicated that the modulus of elasticity in the longitudinal orientation was different from the perpendicular and transverse orientations ($P<0.001$), which were statistically indistinguishable from each other. Evidence of the transition from a random to anisotropic material occurred between a binned FFT alignment value of 0.05 and 0.06 units. As with peak strain, the modulus of elasticity of the longitudinal test samples diverged from the perpendicular and transverse test samples at a binned FFT value of 0.05 units ($P<0.05$). Interactions between the binned FFT alignment value and orientation of testing were also present ($P<0.001$). Changes in the modulus of elasticity for longitudinal test samples were detectable over 4-5 bins (Table 5.2, Table III). Limited interactions between the FFT value and testing angle were detected in the perpendicular test groups and none were evident in the transverse test groups (Table 5.2, Table III).

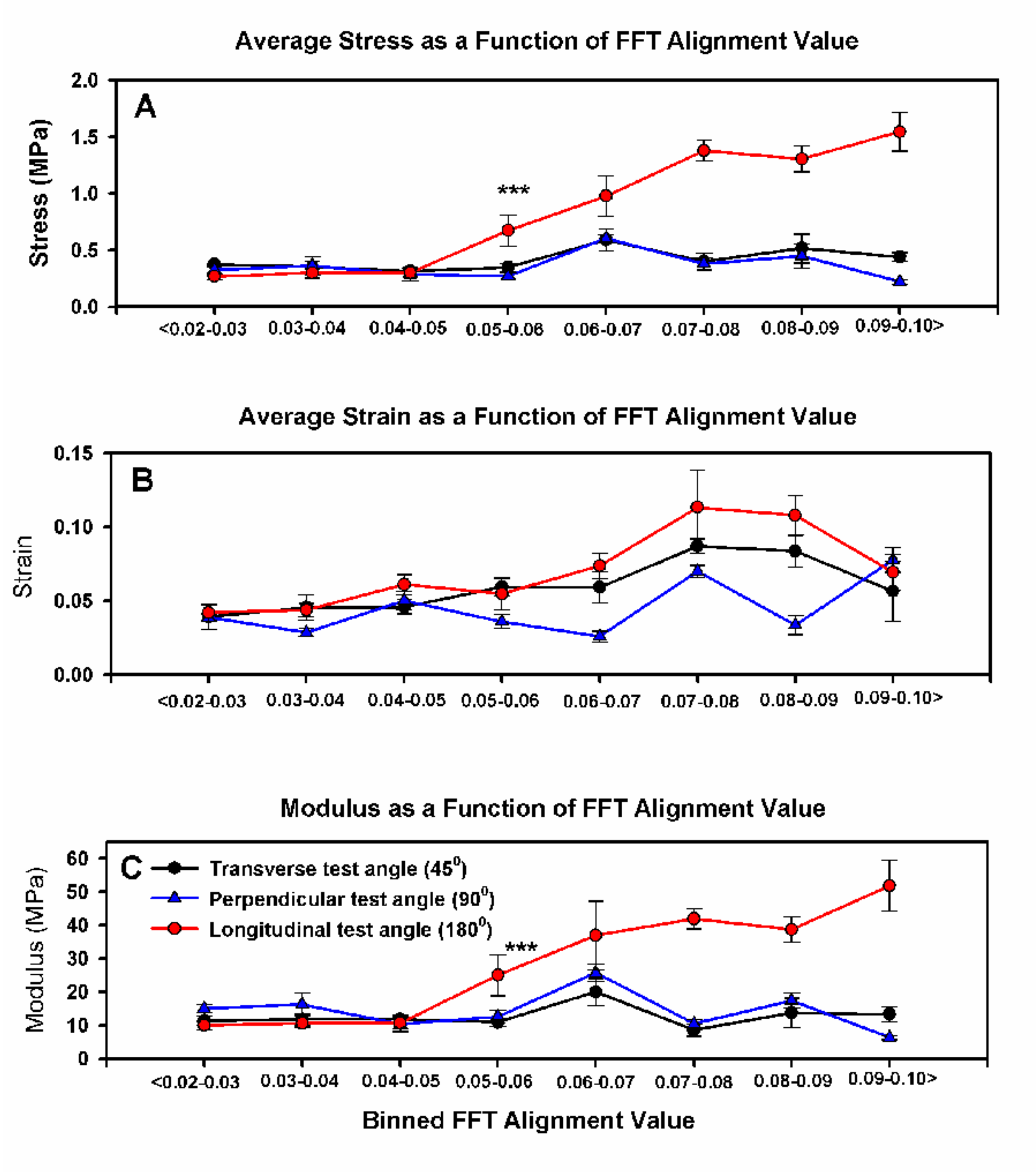
Average Stress as a Function of FFT Alignment Value
A
Stress (MPa)
2.0
1.5
1.0
0.5
0.0
***
<0.02-0.03
0.03-0.04
0.04-0.05
0.05-0.06
0.06-0.07
0.07-0.08
0.08-0.09
0.09-0.10>
Average Strain as a Function of FFT Alignment Value
B
Strain
0.15
0.10
0.05
0.00
<0.02-0.03
0.03-0.04
0.04-0.05
0.05-0.06
0.06-0.07
0.07-0.08
0.08-0.09
0.09-0.10>
Modulus as a Function of FFT Alignment Value
C
Transverse test angle (45⁰)
Perpendicular test angle (90⁰)
Longitudinal test angle (180⁰)
***
Modulus (MPa)
60
50
40
30
20
10
0
<0.02-0.03
0.03-0.04
0.04-0.05
0.05-0.06
0.06-0.07
0.07-0.08
0.08-0.09
0.09-0.10>
Binned FFT Alignment Value

Figure 5.6 A-C. Impact of testing angle on the peak stress (A), peak strain (B) and modulus of elasticity (C) as a function of FFT alignment value. From the peak stress data we conclude: 1) onset of anisotropy begins at FFT values greater than 0.05 units, 2) scaffolds tested in the transverse orientation are isotropic with scaffolds tested in the perpendicular orientation and 3) peak stress of longitudinal samples changes incrementally in 1-2 FFT alignment units. Asterisks in A and B indicate the onset of anisotropic properties within the longitudinal samples and the divergence of these samples from the perpendicular and longitudinal test groups. See Figure 6 for a complete breakdown of the statistical analysis. All data ± S.E.

Table I. Stress as a function of FFT alignment value

Longitudinal FFT	0.02	0.03	0.04	0.05	0.06	0.07	0.08	0.09	0.10
0.10	$P<0.001$	$P<0.001$	$P<0.001$	$P<0.001$	$P<0.001$	$P<0.001$	$P<0.001$	$P<0.001$	***NA***
0.09	$P<0.001$	$P<0.001$	$P<0.001$	$P<0.001$	No	No	No	***NA***	
0.08	$P<0.001$	$P<0.001$	$P<0.001$	$P<0.001$	$P<0.024$	No	***NA***		
0.07	$P<0.001$	$P<0.001$	$P<0.001$	$P<0.001$	No	***NA***			
0.06	$P<0.002$	$P<0.003$	$P<0.002$	No	***NA***				
0.05	$P<0.006$	$P<0.006$	**$P<0.001^{*}$**	***NA***					
0.04	No	No	***NA***						
0.03	No	***NA***							
0.02	***NA***								

Perpendicular FFT	0.09
0.06	$P<0.048$

Transverse FFT	0.04
0.06	$P<0.022$

Table II. Strain as a function of FFT alignment value

Longitudinal FFT	0.02	0.03	0.04	0.05	0.06	0.07	0.08	0.09	0.10
0.08	$P<0.001$	$P<0.001$	$P<0.001$	$P<0.001$	No	No	No	No	***NA***
0.07	$P<0.002$	$P<0.001$	$P<0.037$	$P<0.019$	No	No	No	***NA***	

Perpendicular FFT	0.02	0.03	0.04	0.05	0.06	0.07	0.08	0.09	0.10
0.10	$P<0.002$	$P<0.001$	No	$P<0.001$	$P<0.011$	No	$P<0.045$	No	***NA***

Transverse FFT	0.02	0.03	0.04	0.05	0.06	0.07	0.08	0.09	0.10
0.10	$P<0.001$	$P<0.001$	$P<0.001$	$P<0.001$	$P<0.001$	$P<0.001$	$P<0.001$	$P<0.001$	***NA***

Table III. Modulus as a function of FFT alignment value

Longitudinal FFT	0.02	0.03	0.04	0.05	0.06	0.07	0.08	0.09	0.10
0.10	$P<0.008$	$P<0.005$	$P<0.001$	$P<0.035$	No	No	No	No	***NA***
0.09	No	No	$P<0.009$	No	No	No	No	***NA***	
0.08	$P<0.039$	$P<0.018$	$P<0.001$	No	No	No	***NA***		
0.07	No	No	No	No	No	***NA***			
0.06	$P<0.001$	$P<0.001$	$P<0.001$	$P<0.003$	***NA***				

Perpendicular FFT	0.02	0.03	0.04	0.05	0.06	0.07	0.08	0.09	0.10
0.10	No	No	No	No	$P<0.015$	No	No	No	***NA***
0.09	No	No	No	No	$P<0.023$	No	No	***NA***	

Table 5.2. Summary of statistical analysis for data presented in Figure 5: peak stress (Table I), peak strain (Table II) and modulus of elasticity (Table III). Asterisk in Table I denotes the putative threshold where scaffold anisotropy begins to impact material properties.

DISCUSSION

In this study we examined how fiber diameter, scaffold architecture and angle of testing interact to modulate the material properties of an electrospun scaffold. The results of these experiments provide support for two distinct conclusions. First, within limits, fiber diameter does not appear to play a ***direct*** role in governing the material properties of an electrospun scaffold. Second, optical FFT alignment values of greater than 0.05 units must be achieved before any evidence of directional bias in materials testing can be detected. Once this FFT alignment threshold was been surpassed, incremental changes in scaffold anisotropy resulted in incremental changes in peak stress as a function of 1-2 FFT alignment bins when scaffolds are tested in the longitudinal orientation.

Average fiber diameter and the degree to which a population of fibers are aligned along a given axis represent properties that are intrinsic to the three dimensional architecture and structure of an electrospun scaffold. The angle at which a test load is applied across a scaffold is independent of, and extrinsic to, the structural characteristics of that particular sample. The material properties of an idealized scaffold composed of random elements can be expected to be identical regardless of the angle of testing (orientation of the test load with respect to mandrel rotation). Under these circumstances, the material properties should vary as a function of polymer identity and potentially the diameter, density, and tortuosity of the fibers in the scaffold, as well as the degree to which the constituent fibers are entangled (and/or solvent welded) with one another. The calculated material properties of a scaffold should only vary as a function of the angle of testing if a substantial percentage of the fibers are aligned along a unique axis [108]. A consideration of scaffold anisotropy represents a critical design feature in the fabrication of blood vessels, ligaments and other tissues that may be subject to uniaxial mechanical loads.

On first pass, statistical evaluation of our data sets indicated that fiber diameter represents an underlying variable that defines scaffold material properties (Figure 5.5 A). However, we argue that fiber diameter plays a relatively minor and indirect role in determining the material properties observed in our gelatin-based scaffolds. To support this conclusion we cite experiments in which we independently examined how the angle of testing (Figure 5.5 B: in the context of fiber diameter, ignoring the contributions of alignment) and fiber alignment (Figure 7: in the context of the testing angle, ignoring the contributions of fiber diameter) regulate scaffold material properties. Data presented in Figure 5.5 B indicate that peak stress varies as a function of the testing angle. This effect was only present in a specific subset of the data. Evidence of directional bias was absent in scaffolds prepared from the 120 mg/ml starting concentrations under all conditions and was present in scaffolds prepared from the 150 and 180 mg/ml starting concentrations under selected conditions (Figure 5.5 C).

Experiments presented in Figure 5.6 A provide an explanation for the previously stated results. In these experiments the peak stress in scaffolds with FFT alignment values of less than 0.05 units, regardless of fiber diameter, did not exhibit any evidence of directional bias in materials testing. This data range includes samples prepared from each of the starting concentrations and contains scaffolds composed of all fiber diameters.

Peak stress at failure was similar in each of the three orientations (longitudinal, perpendicular and transverse) tested in this subset of samples. Since these scaffolds exhibit no evidence of directional bias in materials testing they are, by definition, composed of random elements. This result makes it possible to discount the potential contributions of scaffold architecture (*e.g.* preferential fiber alignment) and provides direct evidence that fiber diameter does not play a crucial role in determining peak stress.

Scaffolds produced from the 120 mg/ml solutions are composed of fibers less than 2.0 µm in diameter. Consistent with our previous work [133], we were unable to produce any scaffolds from this treatment group with a FFT alignment value of greater than 0.05 units (Figures 5.2-5.4). The charged electrospinning jet produced by a low viscosity starting solution (*e.g.* 120 mg/ml) has a highly erratic path within the air gap, leading to the deposition of fibers along many different orientations when they collide with the target mandrel [117][118]. Thus, it is very difficult to induce alignment in a scaffold composed of small diameter fibers. Extremely high rates of mandrel rotation [110], more sophisticated collecting mandrels and/or the use of AC electrospinning potentials [109] must be used to induce anisotropy in this type of scaffold.

Directional bias in materials testing was evident in scaffolds that had FFT alignment values of 0.05 units and greater. On our arbitrary FFT alignment scale, this value appears to represent a threshold where a sufficient fraction of fibers have become aligned along a common axis to induce directional bias in materials testing. Once this threshold was reached, peak stress underwent incremental increases as function of 1-2 FFT alignment bins in the longitudinal test groups (again regardless of fiber diameter).

The data sets that exceed the 0.05 FFT alignment value are populated with scaffolds derived from the 150 and 180 mg/ml starting solutions (scaffold composed of fibers >3.0 μm in diameter). In conventional electrospinning systems fiber diameter is primarily determined by polymer concentration, the viscosity of the starting solutions and the degree of chain entanglements that are present at the onset of processing. Within limits, manipulating these parameters to increase the mass of the charged electrospinning jet induces the formation of progressively larger diameter fibers (Figure 5.1). In addition, increasing the mass of the charged jet increases its inertia, a condition that tends to dampen the amplitude of the whipping motions typically observed during fiber formation in the electrospinning air gap. This dampening effect makes it possible to induce fiber alignment at progressively lower mandrel RPM as a function of increasing fiber diameter [14]. We contend that the statistical treatment of the data presented in Figure 5.5 A indirectly documents the evolution of fiber alignment in selected data sets. We conclude from these results that it is the evolution of fiber alignment as a consequence of the fundamental characteristics of the electrospinning process, not fiber diameter, which plays a central role in modulating the material properties of our model scaffolds.

CONCLUSION

We were able to detect incremental changes in peak stress as a function of 1-2 FFT alignment bins (Figure 5.6 A), suggesting that data generated from this sampling technique can represent a sensitive measure of fiber alignment. Incremental changes in the FFT alignment value were correlated with incremental changes in peak stress at failure. From our results, it is evident that scaffold anisotropy plays a central role in determining the material properties of a fibrous matrix. However, a determination of how mechanical loads are distributed across the individual fibers of an electrospun matrix has yet to be developed. Conventional materials testing cannot be used establish the extent to which the populations of fibers undergo re-arrangement in response to an applied load. At present we are examining this issue by using real time changes in 2D FFT alignment values in scaffolds subjected to different loading conditions [83].

CHAPTER 6 Investigation of Dermal Fibroblast Adhesion

Preface: The following manuscript was in the process of being submitted for review at Biomaterials at the time this document was prepared. As a result this chapter may not fully reflect the content of the final published manuscript. The included work investigates differences in cellular processes (adhesion, proliferation and migration) of human dermal fibroblasts in response to denatured collagen-based scaffolds. Additionally, the unmasking and availability of possible RGD binding sites through collagen denaturation is explored. The exposure of normally hidden sites (cryptic sites) binding sites following tissue injury (or protein denaturation) can act as a signaling cue for cells, indicating that the presence of degraded proteins in a tissue-engineering scaffold may be advantageous.

Investigation of Dermal Fibroblast Adhesion on Denatured Electrospun Materials

CE Ayres[1], GL Bowlin[1], DG Simpson[2]

[1]Department of Biomedical Engineering
Virginia Commonwealth University
Richmond, VA 23284

[2]Department of Anatomy and Neurobiology
Virginia Commonwealth University
Richmond, VA 23298

ABSTRACT

In this study, we developed a series of novel assays for the systematic evaluation of protein structure in an effort to examine how the chemical and physical composition of the local microenvironment and the unmasking of possible RGD sensitive binding sites through collagen denaturation, independent of scaffold architecture and porosity, impacts cellular processes. We cultured human dermal fibroblasts on electrospun nylon coated with a variety of non-denatured and thermally denatured collagen-based proteins, as well as recovered electrospun collagen and gelatin (in an effort to examine if the electrospinning process degrades the collagen α chain). Differences in adhesion, proliferation and migration between collagen-based proteins were exhibited. Adhesion inhibition assays using a cyclic RGD peptide demonstrated no change in cell adhesion on non-denatured proteins and a significant drop in cell adhesion on thermally denatured proteins. Based on gel analysis and the results of our functional assays we conclude that collagen α chain structure is not directly altered by the electrospinning process. Overall, the exposure or unmasking of RGD binding sites through the denaturation of collagen proteins represents an important insight into the wound healing paradigm; if tissue injury causes collagen protein degradation, exposure of RGD binding sites to a cell may represent a signaling cue that is necessary for wound resolution.

INTRODUCTION

The extracellular matrix (ECM) functions to define the three-dimensional architecture of tissues and organs and is engaged in a complicated relationship with the cellular elements that populate the surrounding environment. Biochemical and mechanical events can induce changes in the local microenvironment that modulate the composition and architecture of the ECM. In turn, these changes in the ECM can regulate the phenotype and functional properties of the cellular compartment [44][134]. Communication between the cell and ECM molecules influences various cellular processes, such as adhesion, proliferation, differentiation, migration and apoptosis, as well as growth factor and cytokine modulation.

Collagen, a protein native to the ECM, is a natural choice for use in tissue engineering scaffolds. This protein is abundant in mammals and acts as the major structural protein in skin, bones and tendons [67][135]. It has long been used as a biomaterial and in many applications it has proven to be highly biocompatible and readily resorbable [42][136]. Unfortunately, native collagen molecules can undergo changes in response to the conditions used to isolate and or prepare this natural biomaterial for use in a tissue engineering applications. For example, thermal denaturation of collagen breaks the triple helix of the protein into random coils [15]. This change in structure can have profound structural and functional consequences. The loss of the collagen triple helix greatly reduces the mechanical properties of this protein species. Denaturated collagen, (gelatin) can directly modulate the phenotypic profile of the resident cells present in the interstitium, fibroblasts exhibit up-regulated synthesis and degradation of matrix constituents when exposed to this material [17][67][136].

During the many stages of wound repair, cells must adhere to matrix molecules and undergo various levels of migration, proliferation and differentiation [137]. These processes are modulated by a variety of cell surface receptors and specifically by binding events mediated by integrins. Many integrins bind to ECM molecules through a tripeptide sequence, Arg-Gly-Asp (RGD) [138]. Previous research has suggested that the denaturation of collagen proteins exposes previously masked RGD binding sites, thus altering the normal profile of adhesion sites available for binding [138]. Arguably, the cells present within a wound bed have been primed to respond to the profile of matrix components present in that environment. Many tissue engineering scaffolds used in wound healing applications use matrix constituents designed to mimic the native, un-injured extracellular matrix constituents. If tissue injury (or protein denaturation) divulges these binding sites and acts to signal cells to remodel a matrix, the presence of degraded proteins in a tissue engineering scaffold may be advantageous.

Electrospinning has been used to fabricate a variety of native polymers [13][61][62], synthetic polymers [65][110] and blends of native and synthetic polymers [43][66] into highly porous tissue engineering scaffolds composed of nano-to-micron scale diameter fibers [117], a size that approaches the fiber diameters observed in the native extracellular matrix [41]. Electrospinning appears to impart unique, and somewhat controversial, properties to the collagen molecule. From a structural standpoint, we have reported that fibers of electrospun collagen resemble the tertiary structure of the native fibril and exhibit the 67 nm banding pattern typical of this natural biopolymer [13][15]. However, it is clear that processing conditions, and undoubtedly other variables, can greatly alter the physical and material properties of this class of materials [89]. In part this may contribute to the variability of electrospun collagen; the 67 nm banding pattern is not always uniformly present in scaffolds that are nominally identified as a collagen-based material [97].

To date there has not been a systematic investigation designed to characterize how the procedures used to isolate and purify collagen might impact its functional profile at a molecular level. In this study we describe a battery of assays examining how various degrees of thermal denaturation impact collagen function in adhesion, migration and proliferation. We then use the results of these experiments as a barometer to investigate how the electrospinning process might alter collagen function. To separate the fiber forming properties of different protein fractions from the underlying functional consequences of different processing variables we have coated the fibers of electrospun nylon scaffolds with these different protein fractions. These electrospun nylon scaffolds are composed of 1-1.5 μm diameter fibers that have a high surface area and protein binding capacity. By using these charged nylon fibers as a scaffold backbone we can present cells with a microenvironment that has consistent pore dimensions, fiber sizes and material properties. In this study, we cultured human dermal fibroblasts on electrospun nylon coated with a variety of non-denatured and thermally denatured collagen-based proteins in an effort to examine how the chemical composition of the local microenvironment and the unmasking of possible RGD binding sites through collagen denaturation, independent of scaffold architecture and porosity, impacts cellular processes.

MATERIALS AND METHODS

Collagen Preparation. Calfskin corium (Lampire Biologics, Pipersville, PA) was cut into 1 mm² blocks, stirred for 24 hr in acetic acid (0.5M) and blended. All subsequent collagen processing was conducted at 4^0C. The extracted calfskin was filtered through cheesecloth and centrifuged at 10,000G for 12 hr. The supernatant was recovered and dialyzed against ice-cold, ultra pure 18 MΩ-cm water. Final collagen isolates were frozen and lyophilized. Representative collagen fractions used in thermal denaturation experiments were set aside prior to lyopholization and stored at 4^0C until needed.

Soluble collagen fractions were left unheated (C) or thermally denatured at 50 (C50), 60 (C60), 70 (C70) or 80°C (C80) for 1 hr. Other collagen-based materials used for experimentation were produced from commercially purchased gelatin (Sigma, 75 or 225 bloom) and Vitrogen (Cohesion Technologies, Type I collagen) by diluting and dissolving these proteins into ice-cold 18 MΩ-cm water at a concentration of 1.5 mg/ml.

Electrospinning. We used electrospun scaffolds of charged nylon (Ambion) as a solid phase support to characterize how different degrees of heat denaturation impacts collagen function. This approach makes it possible to dissociate the fiber forming properties of a particular protein fraction from the underlying functional consequences of different processing variables. All reagents were purchased from Sigma Aldrich (St. Louis, MO) unless noted.

Positively charged nylon membrane was suspended at 100 mg/ml in 1,1,1,3,3,3-hexafluoro-2-propanol (HFIP) and solubilized under agitation for 12 hr. Solutions were loaded into a 10 ml syringe capped with a blunt end needle [60]. The syringe was then placed into a syringe pump and delivered to the electric field at a rate of 13 ml/hr. The positive output lead of a high voltage power supply (Spellman CZE1000R; Spellman High Voltage Electronics Corporation) was attached with an alligator clip to the blunt end needle and a charged to 23 kV. Scaffolds were electrospun onto a cylindrically shaped stainless steel grounded target (1 in diameter, 5.75 in long) placed 15 cm from the needle tip. The mandrel was set to rotate at approximately 500 RPM to produce scaffolds composed of random elements.

Lyophilized collagen (55 mg/ml) and commercially purchased gelatin (Sigma, 225 bloom, 110 mg/ml) were suspended in HFIP and solubilized for 12 hr on a clinical rotator [13][14][89]. These concentrations were used to produce collagen and gelatin based scaffolds composed of similar fiber diameters. Solutions were electrospun onto a stainless steel rectangular mandrel (70 mm x 10 mm x 5 mm) set to rotate at 500 RPM across a 25 cm air gap. Solutions were delivered at rate of 5 ml/hr to the electric field. Electrospun samples, designated “recovered” electrospun collagen (rEC) or “recovered” electrospun gelatin (rEG), used in SDS gel analysis and cell adhesion, proliferation and migration experiments were produced by dissolving un-cross-linked electrospun scaffolds immediately after fabrication in ice-cold, 18 MΩ-cm water; final protein concentration 1.5 mg/ml.

Gel Analysis. Samples of the collagen fractions used in our experiments were diluted 1:10 in Laemmli sample buffer, final protein concentration 0.15 mg/ml. Proteins were separated by interrupted SDS gel electrophoresis using a 10% polyacrylamide gel [143]. Samples were run until the dye front reached the bottom of the stacking gel, 1 ml of Laemmli buffer supplemented with 20% β-mercaptoethanol was added to the gel and incubated for 30 min at room temperature. Samples were separated until the dye front reached within 1 cm of the bottom of the resolving gel. Gels were stained with Coomassie brilliant blue overnight, de-stained and photographed. Samples were analyzed by densitometry using NIH ImageJ software.

Cell Culture. Adult human dermal fibroblasts (HDF) were purchased from Cascade Biologics (C-013-5C). All cells were passaged 3-5 times in basal dermal fibroblast medium 106 supplemented with a low serum growth kit (Cascade Biologics, S-003-K). Proliferation and migration experiments were conducted in Medium 106 supplemented with a low serum growth kit, with or without 5 ng/ml recombinant human PDGF-AA purchased from R&D Systems (221-AA).

Adhesion Assays. Electrospun nylon scaffolds were cut into strips 1.75 in wide x 3.25 in long and immersion activated in a 20% methanol/phosphate buffered saline (PBS) solution for 20 min. Scaffolds were rinsed 3x in PBS and placed into a dot blotter manifold (Topac Model DHM-48). Each well was supplemented with 50 µl of a collagen fraction and pulled through using a vacuum pump. Scaffolds coated with 1% bovine serum albumin (BSA) were used as controls. All wells were then blocked with 100 µl of 1% BSA solution for 5 min; the solution was then pulled through the membrane. The lower chamber of the dot blotter was filled with PBS until the solution just reached the inferior surface of the electrospun nylon scaffolds. Specific fractions assayed included: control (BSA), unheated calfskin type I collagen (C), collagen fractions subjected to different degrees of heat denaturation, 75 bloom commercial gelatin (G75), 225 bloom commercial gelatin (G225), recovered electrospun collagen (rEC), recovered electrospun gelatin (rEG), Vitrogen collagen (VC) and a mixture of unheated type I collagen and collagen thermally denatured at 50° (Mix C/50). Once the nylon scaffolds were coated the vacuum outflow of the dot blotter was sealed with parafilm. Sealing the dot blotter "pressurizes" it so that media added to the dot blot wells is retained and not wicked through the electrospun scaffolds coated with the different protein fractions. This technique made it possible to use the dot blotter itself as a tissue culture dish for the short term adhesion assays. In each adhesion assay approximately 3,000 HDFs were pipetted into each well (in 100 µl of supplemented medium). Following incubation for 1 hr at 37°C, the dot blotter was inverted to remove any non-adherent cells and the scaffold was removed, rinsed in PBS and fixed in ice-cold methanol for 20 min.

Cross-linked scaffolds were rinsed 5x in a 0.5% Triton solution prepared in PBS and incubated overnight at 4°C with a goat anti-rabbit GAPDH primary antibody (Sigma G9545, 1:5000) diluted in LiCor Odyssey Blocking Buffer. Scaffolds were then rinsed 1x in Odyssey Blocking Buffer 5x in a 0.1% tween-20 solution and incubated with goat anti-rabbit IRDye 800 secondary antibody (LiCor 926-32211, 1:1000) prepared in Odyssey

Blocking Buffer for 1 hr at room temperature. Scaffolds were rinsed in Odyssey Blocking Buffer and 0.1% tween-20. Data images were captured at a line resolution of 84 µm with a Li-Cor Odyssey Imager. The gain of the instrument was set to ensure the signal associated with GAPDH staining did not saturate the detector. See Figure 6.1 A for a representative Li-Cor Odyssey adhesion image. Total N=3-5 independent assays, 3 replicates within each assay.

To determine the experimental parameters for a cyclic RGD peptide cell adhesion inhibition assay, 48 well tissue culture plates were coated with 10 µg/ml Vitrogen type I collagen (VC), laminin (L) or fibronectin (F). Next, we incubated separate aliquots of HDF (10,000 cells per treatment) for 15 min at 37°C with 0.01, 0.1 or 1 µg/ml cyclic RGD peptide (Bachem, H-2574) or 1 µg/ml control RGD peptide (Bachem, H-4088). The cells were then plated for 1 hr on the different ECM surfaces and the plates were inverted to remove any non-adherent cells and processed to image GAPDH as previously described. Electrospun scaffold adhesion experiments with the RGD peptide were conducted in the dot blotter and processed for imaging exactly as previously described. Suspended cells were incubated with 0.01, 0.1 or 1 µg/ml RGD peptide or 1 µg/ml control peptide for 15 min at 37°C and plated for 1 hr as described in the adhesion assays. Total N=1 independent assay, 3 replicates within each assay.

Adhesion assays were evaluated by densitometry using Odyssey software. A circular profile was placed over the domains used to plate the cells (green fluorescence in Figure 6.1 A). Results were collected as "Integrated Intensity" (signal-mm^2) and expressed as a function of the BSA control. Data sets were screened by one-way

ANOVA ($P<0.05$) to test for differences between treatment groups. Dunn's Method ($P<0.05$) and Mann-Whitney Rank Sum test ($P<0.001$) were used in post hoc analysis.

Migration and Proliferation Assays. Electrospun nylon scaffolds were cut into 12 mm diameter circular disks using a dermal biopsy punch. The disks were prepared for protein coating (in a sterile manner) as described, rinsed 3x in PBS and immersed overnight in 15 µg/ml protein/PBS solution using BSA, the collagen fractions C, C50 and C70, rEC, rEG, or VC type I collagen. Disks were cross-linked in 0.5% v/v glutaraldehyde prepared in ethanol for 1 hr, rinsed 3x in PBS and immersed in a 1% glycine/PBS solution overnight to block residual aldehyde groups. Disks were rinsed 3x in PBS and placed into 24 well tissue culture clusters. A sterile 6 mm diameter glass cloning ring (Corning) was placed on top of each disk. Each area encompassed by a cloning ring was plated with 4,000 HDFs in a total volume of 100 µl. The cells were left to settle for 20 min then 500 µl of media supplemented with or without PDGF was pipetted on the outside of the cloning rings. Plates were incubated at 37°C and re-fed media supplemented with or without PDGF at daily intervals. Cloning rings were removed after 24 hr of culture. Electrospun disks were recovered for analysis after 24 or 96 hr of culture. Samples were rinsed in PBS, fixed in ice-cold methanol for 20 min and processed to image GAPDH as described in the adhesion assays.

In these experiments, cell migration was defined as the change in surface area occupied by the cell population over the 24 to 96 interval of culture. These images were imported into the Odyssey Software and the total surface area occupied by the cell population was measured (mm^2). In the Odyssey software area is reported as the number of pixels multiplied by the area per pixel, initial cell plating area = 20 mm^2. Proliferation was defined as the increased fluorescence intensity of GAPDH present in the cultures per unit area of surface. Proliferation results were collected as “Integrated Intensity” (signal-mm^2) and expressed as a function of the BSA control. As with the adhesion experiments the gain of the LiCor instrument was set to ensure the signal associated with GAPDH staining did not saturate the detector. See Figure 6.1 B for a representative Li-Cor Odyssey adhesion image. Data sets were screened two-way ANOVA ($P<0.05$) to test for the impact of PDGF on cell migration and proliferation. Total N=2 independent assays, 2-3 replicates within each assay.

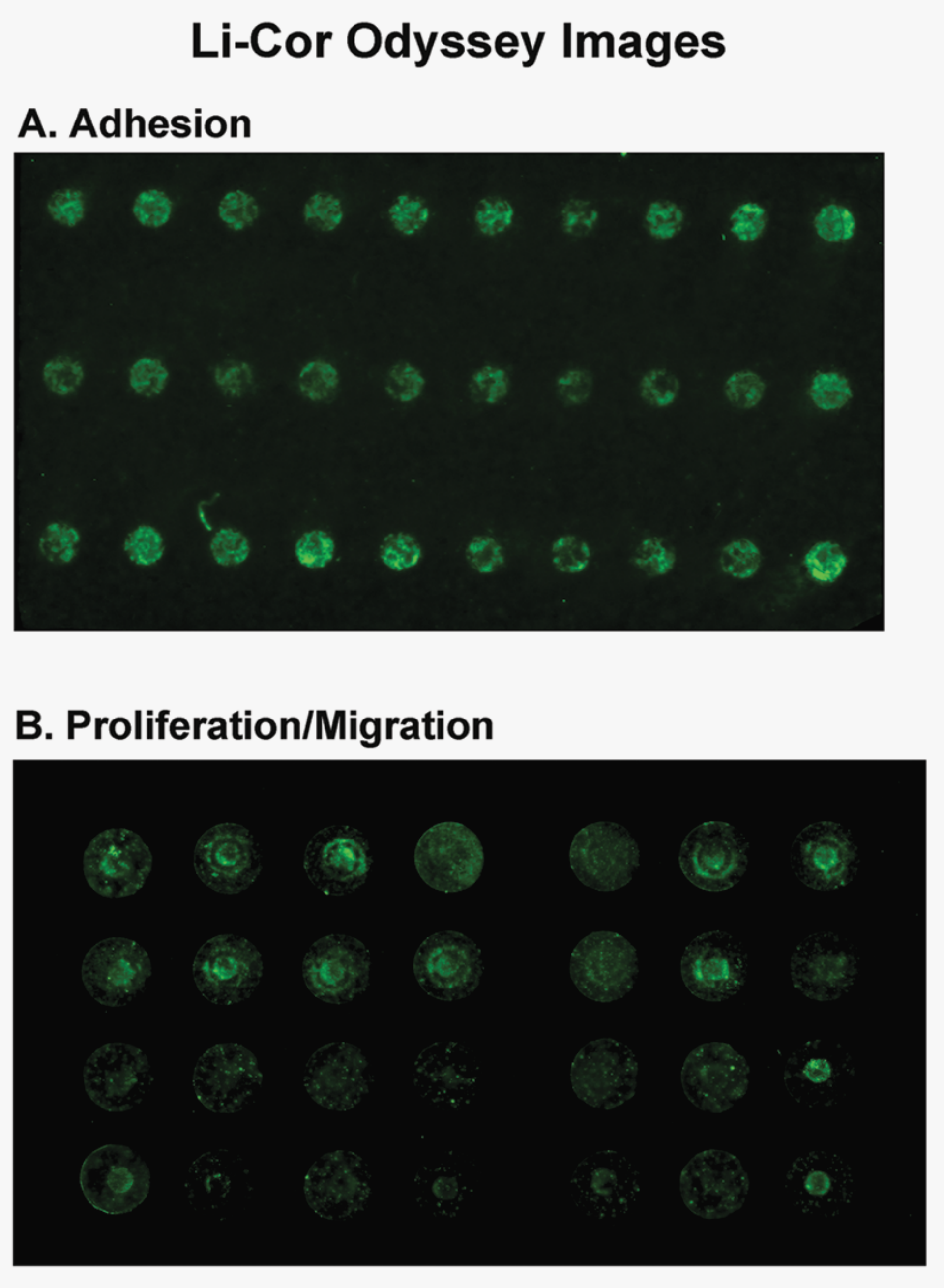

Li-Cor Odyssey Images

A. Adhesion

B. Proliferation/Migration

Figure 6.1 A-B. Representative Li-Cor Odyssey images. Cell adhesion (A) was measured with the Odyssey software by placing a circular profile (slightly larger in diameter than the size of the dot blot well) over the cell adhered area (green fluorescence). Cell proliferation (B) was measured in the same manner as adhesion and cell migration (B) was measured as the difference between the total cell area after initial plating (in the Odyssey software area is reported as the number of pixels multiplied by the area per pixel, initial area = 20 mm^2) and 96 hr (as judged by visual inspection).

Collagen Coating Characterization. To validate the protein immersion method for coating the scaffolds, electrospun nylon scaffolds were cut into 10 mm diameter disks, activated as described and coated with 15 µg protein/ml PBS solution using the collagen fractions C, C50, C60, C70, C80 or VC. Scaffolds were blocked with 1% BSA and left overnight at 4°C with a mouse anti-Collagen type I primary antibody (Sigma C2456, 1:500) prepared in Odyssey Blocking Buffer. Disks were rinsed as described and incubated with goat anti-mouse IRDye 680 secondary antibody (LiCor 926-32220, 1:1000) prepared in Odyssey Blocking Buffer for 1 hr at room temperature and rinsed. Data images were captured with a Li-Cor Odyssey Imager set at a line resolution of 84 µm. Results were collected in "Integrated Intensity" (counts-mm^2). This coating method appears to generate evenly and sufficiently coated scaffolds (Figure 6.2).

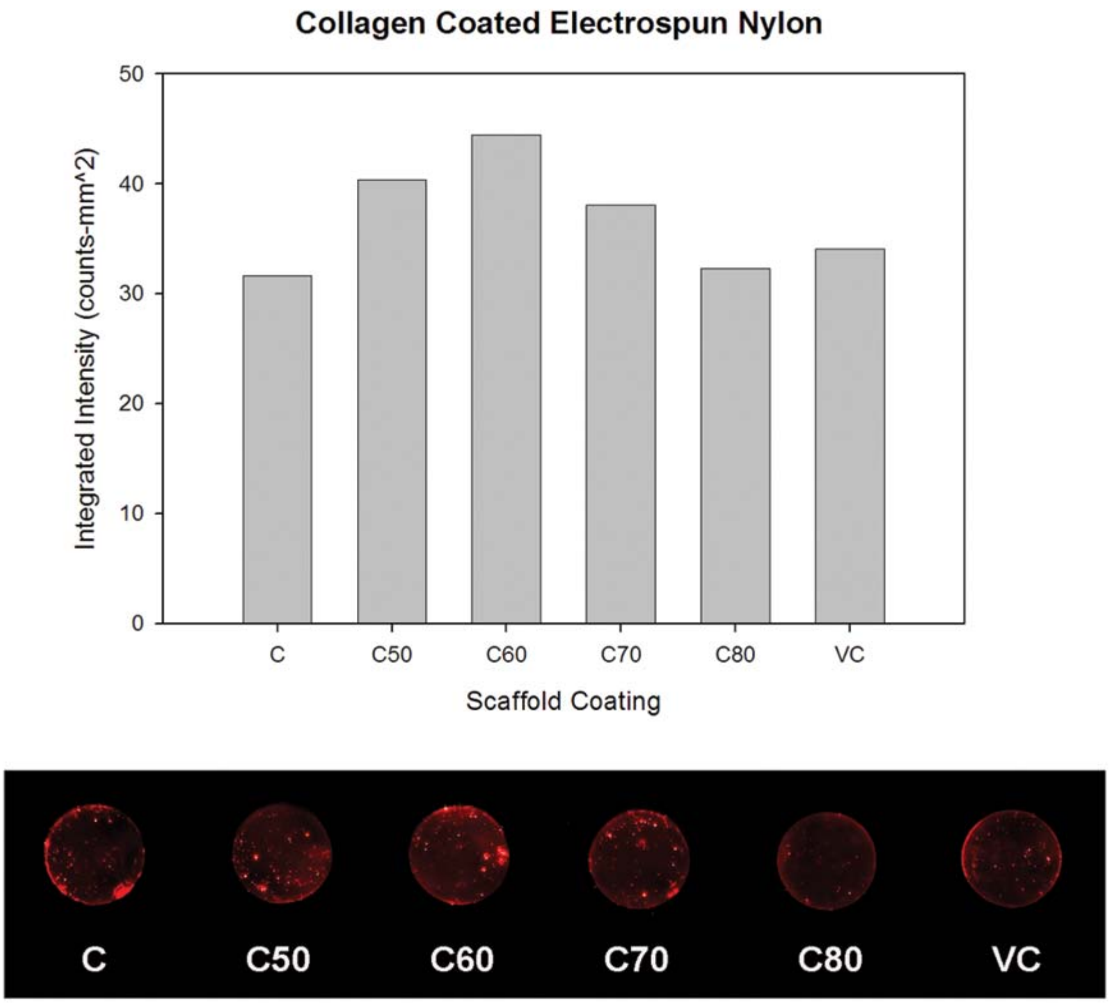

Figure 6.2. Collagen verification by Li-Cor Odyssey. Plot of integrated intensity values (top) verifies the presence of collagen on the nylon scaffolds and the similarities in terms of amount of collagen present. Li-Cor Odyssey image (bottom) of collagen coated scaffolds.

Scanning Electron Microscopy. Scaffolds were sputter coated and imaged with a Zeiss EVO 50 XVP scanning electron microscope equipped with digital image acquisition. Average fiber diameter and pore area data was determined from representative samples using NIH ImageTool (UTHSCSA version 3). All fiber diameter measurements were taken perpendicular to the long axis of electrospun fibers [14][63]. Measurements were calibrated from size bars incorporated into the SEM images at the time of capture.

Materials Testing. Electrospun nylon scaffolds were cut into dumbbell shaped samples using a die punch (2.67 mm wide, gauge length of 0.295 mm). Representative samples were immersed in a 20% methanol/PBS solution for 20 min. The thickness of each dumbbell shaped sample (dry and hydrated) was determined with a Mitutoyo IP54 digital micrometer (Mitutoyo American Corp; Aurora, IL). Dry and hydrated scaffolds were uniaxially tested to failure at an extension rate of 10 mm/min with a Bionix 200 Mechanical Testing Systems instrument (MTS Systems Corp, Eden Prairie, MN). Data sets were screened by one-way ANOVA ($P<0.001$) to test for material property variations in dry and hydrated samples. A Tukey test was used for post hoc analysis ($P<0.05$). Statistical analysis indicates that the measured stress, strain and modulus profiles are all statistically different in dry versus hydrated scaffolds (Figure 6.3).

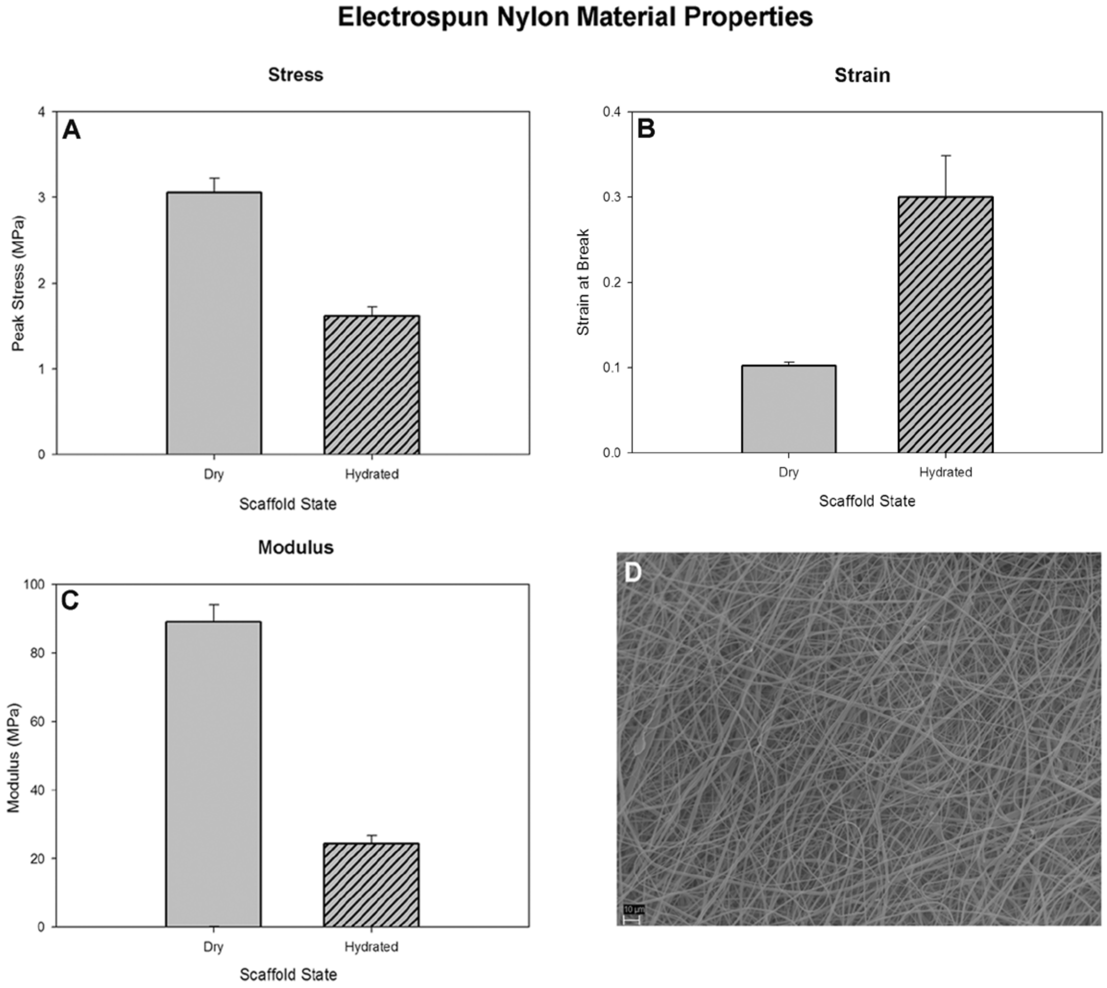

Figure 6.3 A-C. Material properties of dry or hydrated electrospun nylon scaffolds. Peak stress (A), strain (B) and modulus (C) were all statistically different in dry versus hydrated scaffolds (P<0.05). Dry nylon scaffolds reported stress, strain and modulus values of 3.06 ± 0.33 MPa, 89.03 ± 10.07 MPa, and 102 ± 0.8%, respectively. Hydrated scaffolds demonstrated stress, strain and modulus values of 1.62 ± 0.21 MPa, 24.42 ± 4.62 MPa, and 30.0 ± 0.1%, respectively. Scanning electron microscope (SEM) image of a representative nylon scaffold (D) exhibiting an average fiber size of 1.68 ± 0.54 um.

RESULTS

Preparation and Characterization of Collagen Fractions. In preliminary experiments, Vitrogen type I collagen was heated at 50°C for 0, 0.25, 0.5, 1.0, 2.0, or 4.0 hr. Densitometric analysis of the separated protein fractions revealed that nearly 50% of the collagen α chains were lost within 1 hr when exposed to 50^0C (Figure 6.4 A). Calfskin collagen was subjected to a similar analysis; we exposed representative samples of this material to 50, 60, 70, 80 or 90°C for 1 hr. These experiments demonstrate that increased temperatures rapidly accelerate the loss of the large molecular weight collagen α chains (Figure 6.4 B). Evidence of protein fragmentation was detectable at 50°C; at temperatures greater than 80°C the protein bands corresponding to the individual α chains were completely lost from the samples (Figure 6.4 B, lanes 5-7).

To examine how the electrospinning process (solvents and charging) alters α chain content we next prepared electrospun scaffolds of type I collagen or 225 bloom commercially purchased gelatin and then directly recovered the samples for SDS analysis (scaffolds were directly re-dissolved for gel electrophoresis). Equal amounts of protein were separated and as judged by densitometric analysis the protein banding patterns and α chain content in the recovered electrospun samples of calfskin collagen were similar to the control starting material (Figure 6.5, lanes 2 and 3). Protein separation analysis of different permutations of commercially procured gelatin revealed these products, as expected, exhibited extensive α chain fragmentation. The banding pattern typical of intact collagen was absent in these samples (Figure 6.5, lanes 4-6). The gelatin samples were comparable in terms of protein banding patterns and fragmentation to the calfskin collagen samples heated at 80 and 90°C for 1 hr (Figure 6.4 B, lanes 6 and 7).

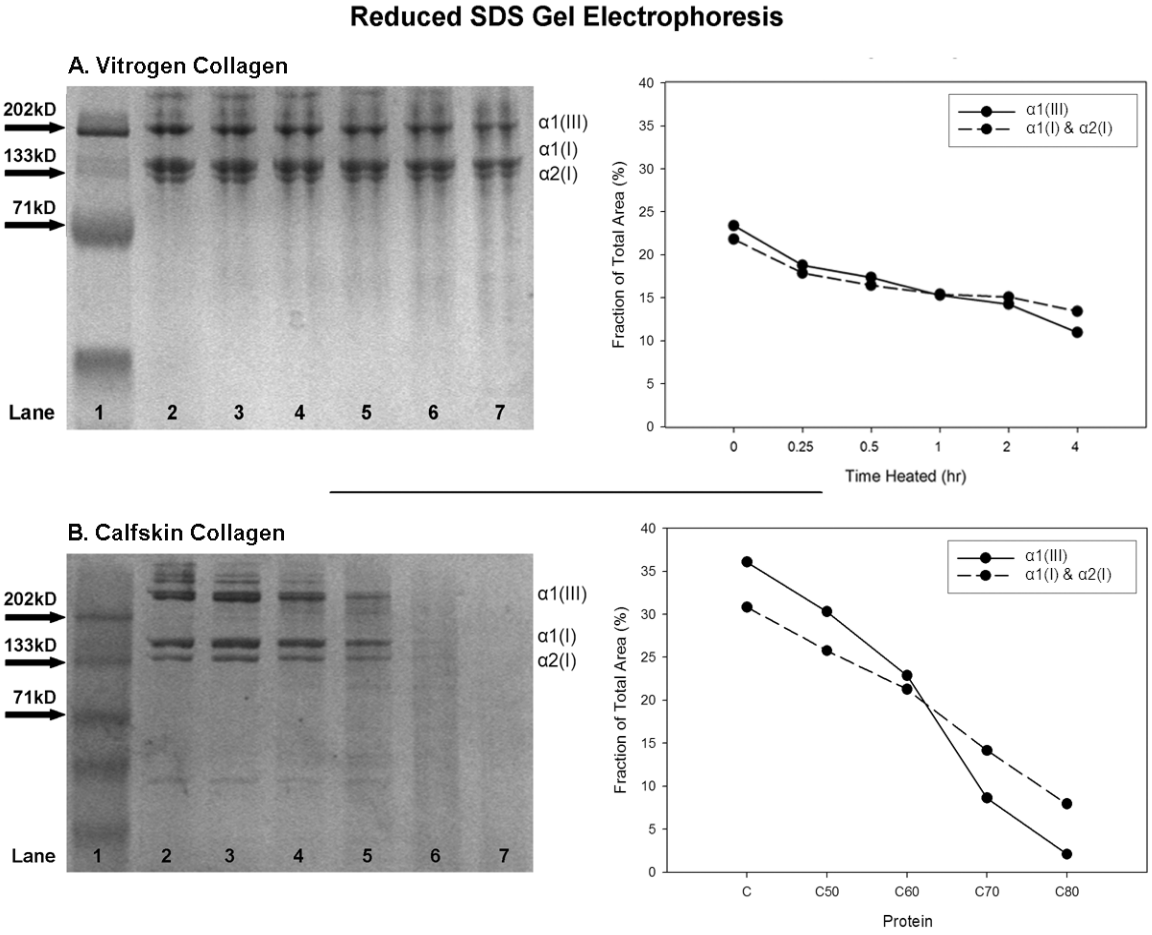

Figure 6.4 A-B. Collagen analysis by reduced SDS gel electrophoresis. Vitrogen collagen (A) heated at 50°C for varying time points and analyzed by gel electrophoresis. Gel (left), Lane 1 = molecular weight standards, Lane 2 = unheated, Lane 3 = 0.25 hr, Lane 4 = 0.5 hr, Lane 5 = 1 hr, Lane 6 = 2 hr, Lane 7 = 4 hr. Plot (right) of each protein as a fraction of total area of α1(III) or α1(I) and α2(I) of Vitrogen collagen. Protein separation analysis indicates that collagen heated for longer time points exhibit increased protein fragmentation. Calfskin collagen (B) heated to varying temperatures and analyzed by gel electrophoresis. Gel (left) Lane 1 = molecular weight standards, Lane 2 = C, Lane 3 = C50, Lane 4 = C60, Lane 5 = C70, Lane 6 = C80, Lane 7 = C90. Plot (right) of each protein as a fraction of total area of α1(III) or α1(I) and α2(I). Protein separation analysis indicates that increasing temperatures drastically decreases the presence of large molecular weight monomers.

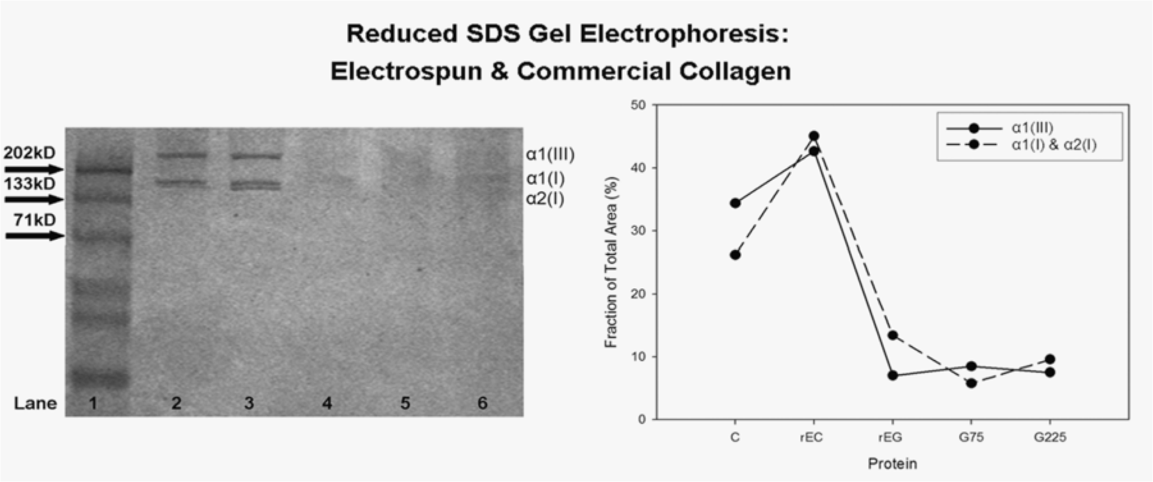

Figure 6.5. Collagen analysis by reduced SDS gel electrophoresis. Recovered electrospun collagen and commercial gelatin (B) analyzed by gel electrophoresis. Gel (left), Lane 1 = molecular weight standards, Lane 2 = C, Lane 3 = rEC, Lane 4 = rEG, Lane 5 = G75, Lane 6 = G225. Plot (right) of each protein as a fraction of total area of band 1 or bands 2 and 3. The electrospinning process does not appear to cause protein fragmentation; see C versus rEC and rEG versus G75 and G225.

HDF Adhesion. To explore how thermal denaturation of collagen α chains impacts function we next conducted adhesion assays with the different protein fractions. Overall, rates of cell adhesion were very similar in all of the thermally manipulated collagen fractions. Unheated calfskin collagen retained approximately 59% more cells when compared to the BSA control. Collagen heated at 50°C retained 33%, 60°C retained 47%, 70°C retained 66% and 80°C retained 57% more cells when compared to the control (Figure 6.6 A). One-way ANOVA failed to detect a statistically significant difference in cell adhesion between these treatment groups ($P<0.05$).

We also examined the functional profiles of a 50:50 mix of unheated collagen and collagen heated at 50°C, 75 bloom gelatin, 225 bloom gelatin, recovered electrospun collagen (calfskin), recovered electrospun gelatin (225 bloom) and Vitrogen type I collagen. The 50:50 mixture of unheated collagen and collagen heated at 50°C retained the most cells, on average 85% more cells became attached to this surface when compared to the BSA control (Figure 6.6 B). Recovered electrospun collagen also supported very high levels of cell adhesion with 64% more cells attaching to this surface. The 225 bloom gelatin (41%), Vitrogen type I collagen (35%) and recovered electrospun gelatin (26%) coated scaffolds all had similar adhesion performance. The 75 bloom gelatin (13%) coated scaffolds exhibited the lowest adhesion. One-way ANOVA, again, failed to detect a statistically significant difference in cell adhesion within these treatment groups and between all treatment groups tested ($P<0.05$).

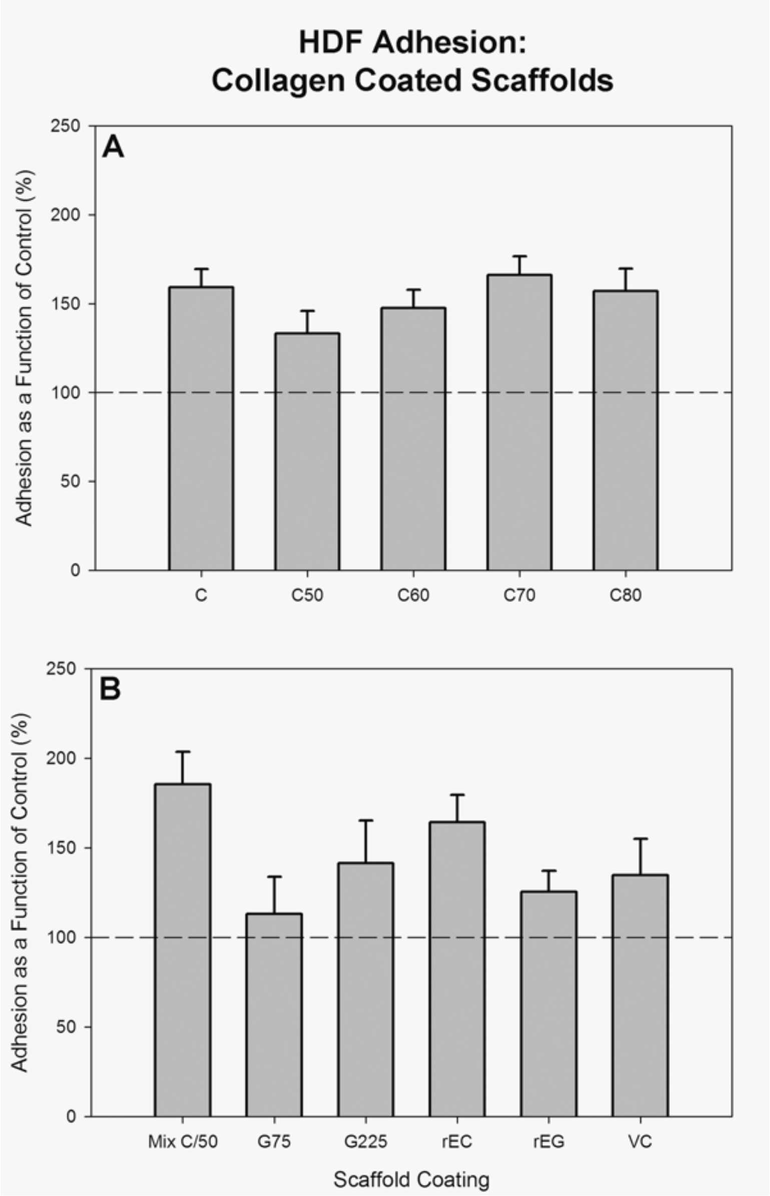

Figure 6.6 A-B. Analysis of HDF adhesion. Plot of change in cell adhesion when plated onto thermally denatured calfskin collagen (A) or collagen-based (B) coated scaffolds. Results are expressed as a function of BSA control For the thermally denatured calfskin collagen, cell adherence was lowest on scaffolds coated with C50 and highest on scaffolds coated with C70. For the collagen-based scaffolds, cell adherence was lowest on G75 and highest on scaffolds coated with Mix C/50 and rEC. Error bars are ± standard error. Note: the dashed line indicates BSA control baseline conditions.

Changes in collagen structure can uncover cryptic RGD-dependent binding sites. To determine how thermal manipulation and the electrospinning process impact the collagen molecule we next challenged HDF in adhesion assays with cyclic RGD peptides. Assays were first conducted with cells plated onto tissue culture plates coated with collagen, laminin or fibronectin. In these experiments, pre-treatment with the RGD peptide decreased total cell adhesion as a function of increasing concentration. For example, with respect to control (un-treated cultures) RGD at a concentration of 1 μg/ml suppressed adhesion by 74% on Vitrogen type I collagen, 68% on laminin and 46% on fibronectin (Figure 6.7). In addition, the control peptide appeared to have no affect on cell adhesion. Analysis by one-way ANOVA detected a statistically significant difference between Vitrogen type I collagen treated with 1 μg/ml peptide and fibronectin treated with 0.01 μg/ml peptide ($P<0.05$).

When we conducted adhesion assays with different ECM proteins prepared on electrospun fibers of nylon we observed similar results. The adhesion of cells to denatured collagens was blocked by RGD peptide challenge (Figure 6.8). Cell adhesion on collagen heated at 70^0 was suppressed up to 60% and recovered electrospun gelatin by 41%, when the cultures were challenged with 1 μg/ml peptide. Adhesion on collagen heated at 50^0C and recovered electrospun collagen were unaffected by the RGD peptides. A modest decrease in adhesion to Vitrogen type I collagen occurred in these same assays. However, we note that cells plated onto Vitrogen that had been applied to tissue culture plates were far more susceptible to RGD challenge than cells plated onto Vitrogen prepared on the electrospun nylon scaffolds. Statistical analysis by one-way ANOVA failed to detect a statistically significant difference between groups ($P<0.05$).

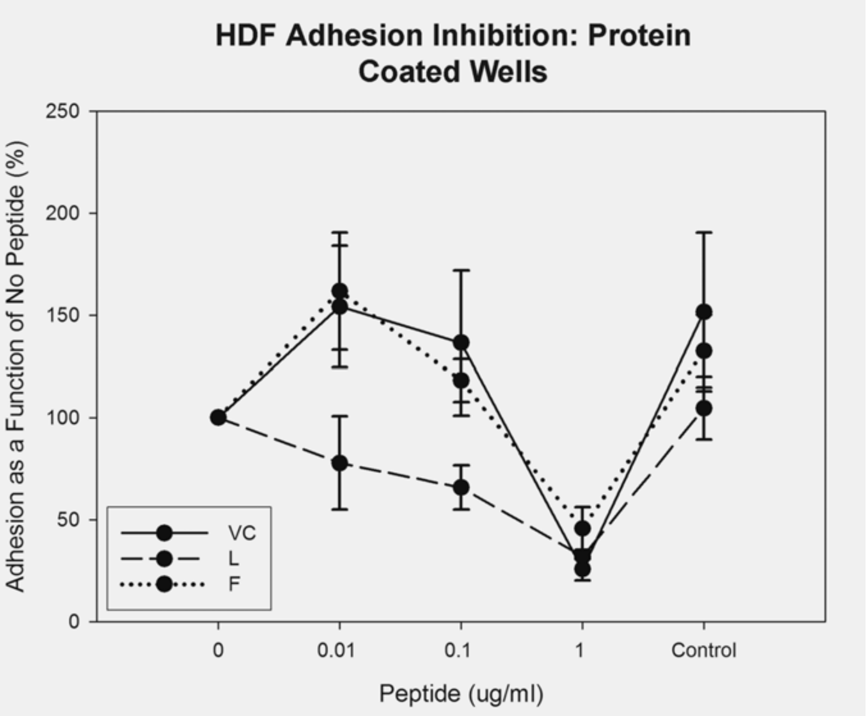

Figure 6.7. Analysis of HDF adhesion inhibition on protein coated wells. Plot of change in cell adhesion with increasing concentrations of RGD peptide. Results are expressed as a function of no peptide added. Cell adhesion was inhibited on all proteins. A statistically significant difference was detected between Vitrogen type I collagen treated with 1 μg/ml peptide and fibronectin treated with 0.01 μg/ml peptide ($P<0.05$). Error bars are ± standard error.

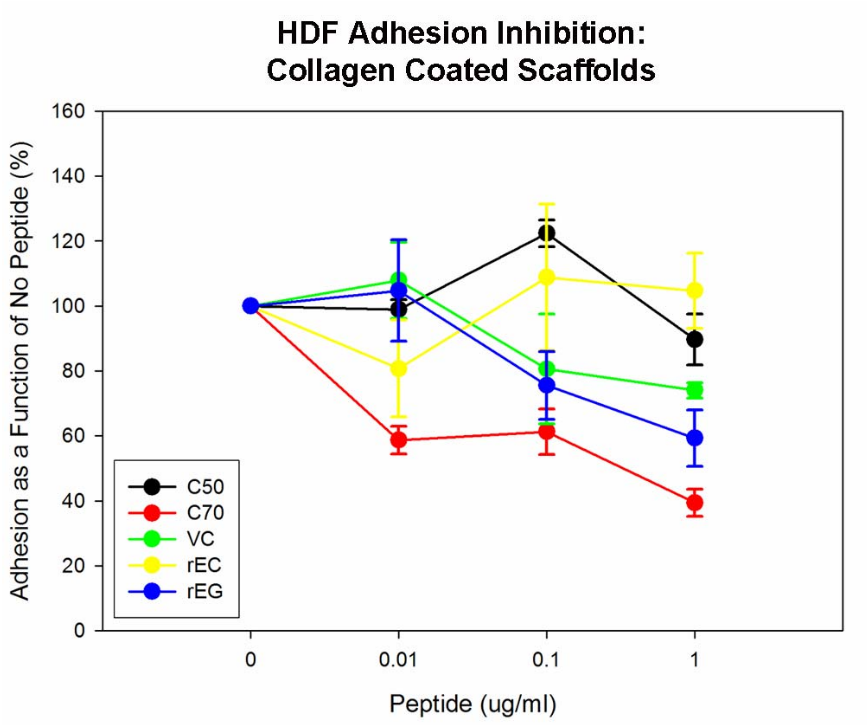

Figure 6.8. Analysis of HDF adhesion inhibition on collagen-based coated scaffolds. Plot of change in cell adhesion with increasing concentrations of RGD peptide. Results are expressed as a function of no peptide added. Denatured collagens (C70 and rEG) exhibited reduced cell adhesion while non-denatured collagens (C50 and rEC) demonstrated no change in cell adhesion, with the exception of non-denatured VC which revealed slightly reduced adhesion. No statistically significant differences were detected. Error bars are ± standard error.

HDF Migration. Migration assays were conducted on electrospun nylon scaffolds coated with control unheated collagen, collagen heated at 50°C, collagen heated at 70°C, recovered electrospun collagen, recovered electrospun gelatin or Vitrogen type I collagen. These experiments were done in the presence and absence of PDGF, a growth factor that plays a critical role in signaling the interstitial cell population during the wound healing cascade [1][84][141]. In control (cultures not treated with PDGF) the total measured cell area remained nearly unchanged over the 96 hr interval of culture with respect to baseline controls (20 mm^2) (Figure 6.9 A). Scaffolds coated the BSA control, unheated collagen and collagen heated at 50 or 70°C exhibited cell culture surface areas of 20.9 ± 2.8, 16.1 ± 1.9, 21.9 ± 2.2 and 20.5 ± 7.7 mm^2, respectively (mean ± standard deviation). Cells plated onto scaffolds coated with recovered electrospun collagen (26.0 ± 10.9 mm^2), recovered electrospun gelatin (27.7 ± 6.6 mm^2) and Vitrogen type I collagen (24.9 ± 8.1 mm^2) qualitatively occupied slightly more area. Screening these data sets with two-way ANOVA failed to detect any differences in these treatment groups.

HDFs cultures treated with PDGF typically expanded their cell area nearly two-fold with respect to the originally plated cell area (20 mm^2) (Figure 6.9 A). Scaffolds coated with control (22.8 ± 1.2 mm^2) did not notably expand cell area (109% with respect to untreated control). Scaffolds coated with unheated collagen (41.9 ± 6.9 mm^2), collagen heated at 50°C (47.9 ± 15.1 mm^2) and recovered electrospun collagen (54.8 mm^2 ± 5.1 mm^2) exhibited the largest increase in cell culture surface area in response to PDGF (261, 219 and 211%, respectively, with respect to untreated controls) (Figure 6.9 B). Collagen heated at 70°C (39.8 ± 14.0 mm^2), recovered electrospun gelatin (39.0 ± 4.2 mm^2) and

Vitrogen type I collagen (41.0 ± 14.6 mm^2) supported similar degrees of migration (and demonstrated a change of 194, 141 and 164 %, respectively, with respect to untreated controls). Analysis by two-way ANOVA detected statistically significant differences between non-PDGF and PDGF incubated scaffolds, as well as statistically significant differences between the control and recovered electrospun collagen and collagen heated at 50°C and also between the recovered electrospun collagen and recovered electrospun gelatin coated scaffolds ($P<0.05$). Overall, cultures of HDFs incubated with PDGF appear to be extremely mobile while cultures incubated without PDGF demonstrated very little movement of any kind.

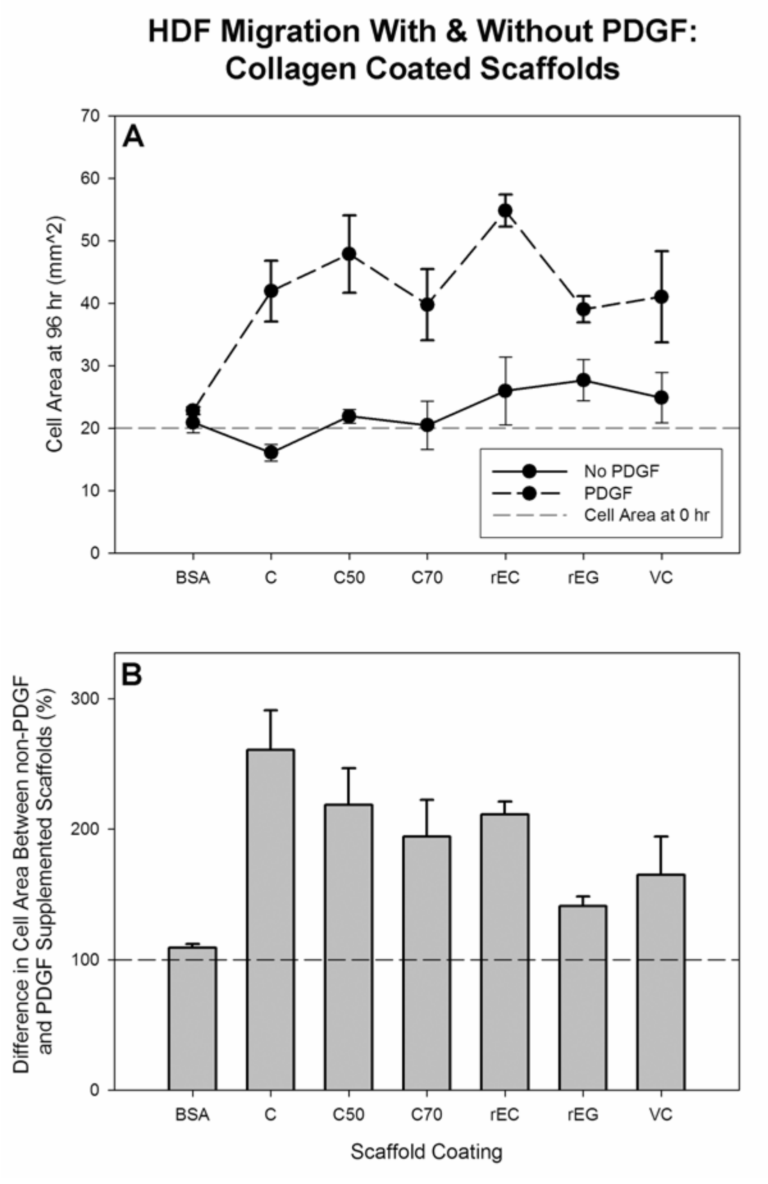
HDF Migration With & Without PDGF:
Collagen Coated Scaffolds
A
Cell Area at 96 hr (mm^2)
0
10
20
30
40
50
60
70
No PDGF
PDGF
Cell Area at 0 hr
BSA
C
C50
C70
rEC
rEG
VC
B
Difference in Cell Area Between non-PDGF and PDGF Supplemented Scaffolds (%)
0
100
200
300
BSA
C
C50
C70
rEC
rEG
VC
Scaffold Coating

Figure 6.9 A-B. Analysis of HDF migration. Plot of cell area of HDFs (A) plated onto collagen-based coated scaffolds cultured with and without PDGF. All scaffolds cultured with HDFs and incubated with media *not* supplemented with PDGF exhibited little evidence of migration across the scaffold. No statistical difference in migration area was detected between any of the coated scaffolds incubated without PDGF. All scaffolds cultured with HDFs and incubated with PDGF supplemented media demonstrated high mobility over the scaffolds, typically expanding their cell area *at least* two-fold. With respect to the untreated groups, scaffolds treated with PDGF had significantly higher mobility (B). For PDGF supplemented treatment groups, statistically significant differences were detected between the BSA and rEC and C50, as well as between rEC and rEG coated scaffolds (P<0.05). Error bars are ± standard error. Note: the dashed line in (B) denotes baseline conditions.

HDF Proliferation. Varying rates of cell migration and changes in cell number clearly play a role in dictating total cell culture surface area. To investigate how changes in cell number contribute to our results we next prepared scaffolds coated with unheated collagen, collagen heated at 50°C, collagen heated at 70°C, recovered electrospun collagen, recovered electrospun gelatin or Vitrogen type I collagen. Once again, these experiments were done in the presence or absence of PDGF. After 24 hr, cell number on all scaffolds remained unchanged in the cultures treated with control media (with respect to the BSA control) (Figure 6.10). After 96 hr all of the scaffolds incubated without PDGF, with the exception of those coated with recovered electrospun collagen or Vitrogen type I collagen, remained. With respect to change in cell number from 24 to 96 hr in the absence of PDGF, cultures plated onto unheated collagen exhibited the greatest drop in cell number (39% of controls) and cultures plated onto Vitrogen type I collagen exhibited the highest number of cells (118% of controls) (Figure 6.11 A and B). The BSA control, collagen heated at 50 or 70°C, recovered electrospun collagen and recovered electrospun gelatin exhibited essentially no change from 24 to 96 hr and yielded results of 80, 72, 89, 94 and 99%. Analysis by two-way ANOVA did not detect any statistical differences between any of the scaffolds cultured in the absence of PDGF.

The response of the cells to PDGF was highly variable and varied as a function of scaffold composition. Cell number remained constant over the first 24 hr interval of culture (Figure 6.10). However, by 96 hr, cell number increased (with respect to 24 hr) in cultures plated onto unheated collagen (180% of control), collagen heated at 50°C (233% of control), collagen heated at 70°C (146% of control) and Vitrogen type I collagen

(130% of control) (Figure 6.11 A and B). Cultures plated onto the BSA control, recovered electrospun collagen and recovered electrospun gelatin remained relatively unchanged over this same interval (96, 99 and 115% of control). Analysis by two-way ANOVA detected statistically significant differences between non-PDGF and PDGF incubated scaffolds, as well as a statistically significant difference between collagen heated at 50°C and all other treatment groups, with the exception of unheated collagen ($P<0.05$). These results again underscore the crucial role PDGF plays in guiding cell processes; both HDF migration and proliferation were greatly enhanced with the addition of PDGF supplemented media.

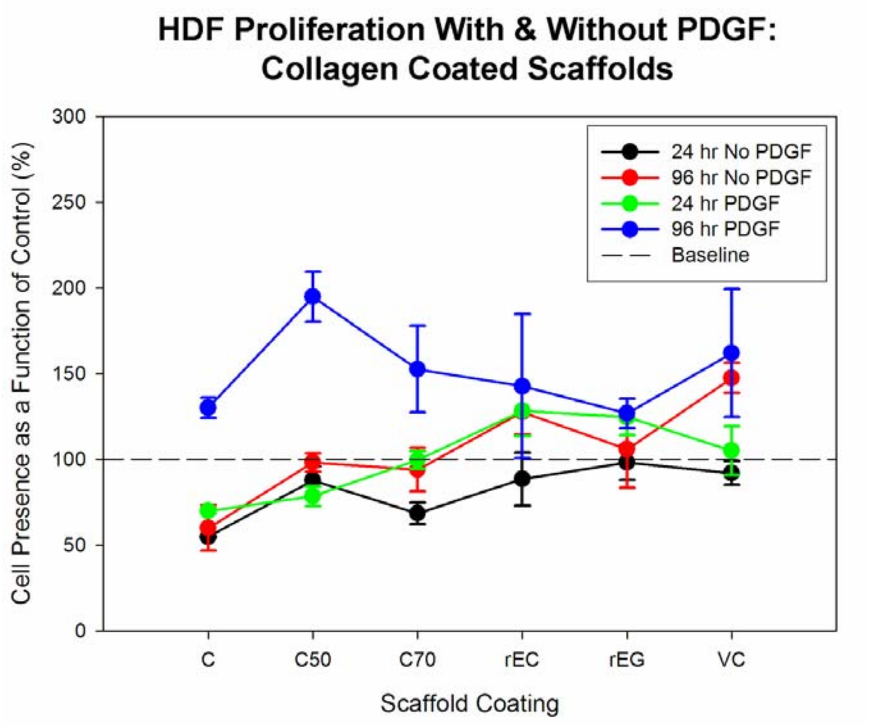

Figure 6.10. Analysis of HDF proliferation. Plot of cell number (as judged by GAPDH intensity) when plated onto collagen-based coated scaffolds (at 24 and 96 hr, with and without PDGF). Results are expressed as a function of BSA control. At 24 hr, cell number on all scaffolds was similar. At 96 hr, scaffolds incubated *without* PDGF exhibited no change or a slight increase in cell number while scaffolds incubated *with* PDGF demonstrated no change or a significant increase in cell number. Error bars are ± standard error.

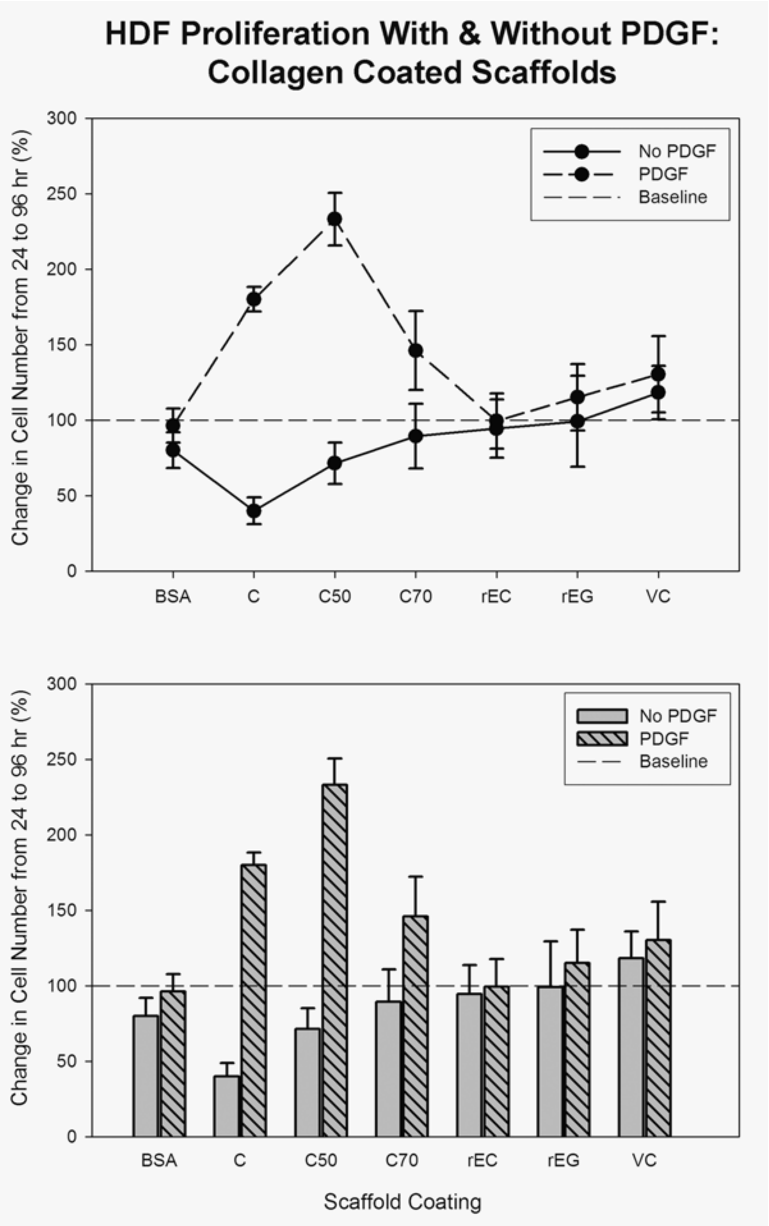

Figure 6.11 A-B. Analysis of HDF proliferation. Plots of change in cell number (as judged by GAPDH intensity) from 24 to 96 hr (A and B). For scaffolds incubated *without* PDGF, change in cell number dropped or remained the same. No statistically significant differences were detected between any of the non-PDGF supplemented treatment groups. For scaffolds incubated *with* PDGF, C, C50 and C70 demonstrated a large increase in cell number from 24 to 96 hr while all other treatment groups exhibited little or no change. Statistically significant differences were detected between C50 and all other PDGF supplemented treatment groups, with the exception of C ($P<0.05$). Error bars are ± standard error.

DISCUSSION

In this study we examined how the chemical and physical composition of the local microenvironment and exposure of RGD sensitive binding sites influences cellular processes. By using electrospun nylon as a foundation material and coating it with proteins of interest, we were able to create scaffolds with identical pore dimensions, fiber sizes and material properties, thus allowing us to pinpoint any differences in adhesion, proliferation or migration as a result of protein coating identity. In this study we describe the use of a number of novel assays in examining how various degrees of thermal denaturation and the electrospinning process might alter collagen function in adhesion, migration and proliferation.

Protein Analysis. We examined collagen structure as a function of thermal denaturation by SDS gel electrophoresis in order to characterize the physical state of the proteins of interest and their similarities to one another. Protein analysis of type I collagen heated for varying lengths of time (Figure 6.4 A) or at varying temperatures for a fixed interval (Figure 6.4 B) demonstrated that while both temperature and exposure time play a role in the denaturation of proteins, temperature is the key variable controlling protein fragmentation in this type of sample. This result is consistent with previous reports indicating that collagen isolated from rat tail tendon does not exhibit any substantive changes in structure at temperatures below 54°C [139]. It appears that a specific heat threshold is needed to induce significant fragmentation of the collagen α chains; a rise in temperature rapidly increases the rate and extent to which these chains are broken down. While our experiments did show some protein degradation with prolonged heat exposure (at a temperature below 54°C), this process appears to be considerably more gradual then exposure to higher temperatures.

Recently, questions have arisen regarding the effect of the electrospinning process on the integrity of the collagen triple helical structure. In past studies we have demonstrated that electrospun collagen exhibits a 67 nm repeat that resembles the native polymer [13][15]. However, not all investigators have observed the formation of this characteristic structure in fibers of electrospun collagen and it is unclear where this discrepancy might arise [97]. Our protein analysis (and subsequent assays) detected no difference between non-electrospun and electrospun collagen (Figure 6.5, lanes 2 and 3) with respect to apparent protein structure, cell adhesion processes, cell migration or proliferation. Analysis of the 75 and 225 bloom commercially purchased gelatin revealed that these products behaved similar to collagens exposed to thermal denaturation and exhibited substantial α chain fragmentation (Figure 6.5, lanes 5 and 6). This result is in contrast to the expected results; a higher bloom number indicates a higher triple helix content but our analysis demonstrated no discernable difference between the triple helix content of the 75 and 225 bloom gelatin [135].

HDF Adhesion. Adhesion assays conducted on thermally degraded collagen proteins yielded results that indicate an unmasking of RGD binding sites during thermal denaturation. While a number of integrins (α1β1, α2β1, α3β1) bind to type I collagen in a

RGD-independent manner, integrin αvβ3 binds very strongly to *denatured* collagen in a RGD-dependent manner [138]. Upon denaturation of type I collagen, RGD sites appear to become exposed, allowing the cells to bind to these sites through the αvβ3 integrin [138][140]. The implications concerning this unmasking phenomenon are crucial in the understanding of the wound healing process; the unmasking of RGD peptides in injured tissue and the subsequent integrin binding to these peptides indicates a highly regulated signaling method that may play a role in determining the outcome of the wound healing process.

In our experiments, lower adhesion was seen on scaffolds coated with collagen thermally denatured at 50 and 60°C; the modest degree of α chain fragmentation seen in these samples may explain this result (Figure 6.4 B, lanes 3 and 4). These proteins are no longer completely composed of native type I collagen, but the transition to a fully denaturated protein has not occurred. It is possible that the RGD-*independent* adhesion sites used by integrins (α1β1, α2β1, α3β1) are destroyed or becoming masked during collagen denaturation (as RGD sites become unmasked) and since these proteins are only slighted denatured, the number of unmasked RGD peptides may be minimal. Conversely, the peak in cell adhesion observed on scaffolds coated with collagen thermally denatured at 70°C may be indicate a more complete exposure of the RGD sites and, consequently, αvβ3 or perhaps α5β1 binding to these sites. The highest levels of adhesion were seen on scaffolds coated with a mixture of non-denatured collagen and collagen thermally denatured at 50°C. The elevated adhesion levels on the mixed protein coating may be attributed to high binding site availability due to non-denatured collagen RGD-*independent* and denatured collagen RGD-*dependent* binding occurrences.

Overall, electrospun nylon scaffolds coated with commercially purchased proteins (75 and 225 bloom gelatin, recovered electrospun gelatin and Vitrogen type I collagen) had the lowest levels of adhesion. Scaffolds coated with commercially purchased gelatin (75 bloom gelatin, 225 bloom gelatin and recovered electrospun gelatin), proteins which demonstrated similar α chain fragmentation to collagen thermally denatured at 80°C, exhibited lower levels of adhesion than their "corresponding" calfskin collagen counterpart (Figure 6.6 B). It is feasible that these proteins were so degraded as to not have functional binding sites. This conclusion is supported by the protein separation studies that revealed these materials exhibit virtually no α chains. The lower adhesion exhibited on Vitrogen type I collagen fractions may be attributed to the lack of telopeptides present (this collagen is pepsin solubilized, a process that may or may not damage collagen structure) or its high level of purity; while not visible on our protein gels, we cannot exclude the activity of possible contaminating proteins present in our collagen fractions that aided in cell adhesion.

Adhesion inhibition assays conducted on tissue culture plastic demonstrated the viability of the cyclic RGD peptide at inhibiting adhesion. An expected decrease in adhesion (as a function of increasing peptide concentration) was seen on laminin and fibronectin; integrins bind to these proteins in an RGD-*dependent* manner. The slight decrease in adhesion exhibited on Vitrogen type I collagen (which was also seen on assays conducted with Vitrogen prepared on electrospun scaffolds of nylon) was less expected; integrins primarily bind to this protein in an RGD-*independent* manner. Given that RGD binding site exposure is believed to occur on thermally degraded proteins, questions arise regarding possible collagen degradation during the preparation of this collagen, specifically during the pepsin-solubilization step.

Cells plated onto electrospun scaffolds of nylon coated with the denatured protein fraction were sensitive to RGD challenge. Conversely, cells plated onto the non-denatured isoforms were not sensitive to this treatment, indicating the RGD dependent binding sites are exposed when collagen is damaged. Adhesion to collagen heated at 70° was very sensitive to RGD challenge, even at lower doses, again indicating that this level of degradation induces a mass exposure of RGD binding sites. The adhesion assays conducted demonstrated that electrospun collagen supports high levels of adhesion (similar to that of unheated collagen) and adhesion was not inhibited with the RGD peptide, indicating that binding is occurring through a RGD-*independent* manner.

HDF Migration and Proliferation. Migration and proliferation assays conducted on a variety of collagen proteins yielded results that correlate well to cell adhesion results. The highest levels of migration and proliferation were demonstrated on scaffolds that exhibited intermediate levels of adhesion strength and number. If adhesion is too weak or too few adhesions have been made, a cell cannot develop enough traction to propel forward (or divide) and if adhesion is too strong or too many adhesions have been made, it is difficult for cells to release from the substrate and undergo motile activity [142]. However, recovered electrospun collagen exhibited excellent adhesion and migration results but did not change with regards to cell proliferation. This result is reminiscent of the early presence of fibroblasts in wound healing; when fibroblasts are signaled to a wound bed, the immediate task of the fibroblast is migration and infiltration, proliferation occurs at a later time point [1].

CONCLUSION

Based on our gel analysis and the results of our functional assays we conclude that collagen α chain structure is not directly altered by the electrospinning process. Exposure to HFIP, the electrospinning process itself and subsequent recovery of the protein from the resulting scaffolds did not alter cellular response to the parent molecule. We believe that processing variables that occur prior to the actual electrospinning process may be responsible for some of the conflicting reports concerning the structure of electrospun collagen [13][15][97]. In our experience we have observed that the collagen is very susceptible to over-drying and denaturation during the lyopholization steps used to prepare the material for electrospinning. In essence, it is not possible to induce native fiber structure into an electrospun collagen fiber if a partially denatured form of the molecule is used to prepare that fiber. We also note that the structure of electrospun collagen can be extensively modulated in post-processing. These scaffolds must be cross-linked in order to be useful as tissue engineering scaffolds. The identity of the cross linking agent and the actual extent to which a scaffold is cross-linked directly impacts the physically properties of electrospun collagen [89].

The assays described in this paper represent a systematic method for the evaluation of protein structure. Cellular processes are controlled by a complex orchestra of events; however, it is clear that identity and structure of the surrounding ECM play a crucial role in directing these processes. The exposure or unmasking of RGD sites through the denaturation of collagen proteins represents an important regulatory step in the wound healing paradigm; if tissue injury causes collagen denaturation, exposure of RGD sites to a cell may represent a signaling cue that alters cell phenotype and literally prepares the fibroblasts to reconstitute the damaged ECM. Our results suggest that cell phenotype can be regulated by the composition and architecture of the ECM, how this might be exploited to modulate the wound healing process remains to be fully defined.

CHAPTER 7 Overall Conclusions and Future Directions

Defining the complex and multifunctional nature of the native ECM remains an active component of the research endeavor. Fundamentally, scaffolds must provide the structural integrity necessary to support normal cell function and interaction in three-dimensional space. This structural integrity is established by a variety of factors, some of which are determined at the onset of scaffold fabrication (i.e. material identity, fiber alignment) while others result from additional processing methods utilized post-fabrication (i.e. cross-linking). Progress regarding scaffold composition and methods designed to control various aspects of scaffold architecture and function should yield insights into the processes that regulate normal tissue hemostasis. Characterizing the structural and molecular distinctions of the native ECM will aid in the production of meaningful scaffolds.

In this study, structural issues were first addressed. Architectural features play a central role in determining the material properties of the native ECM and classically, material identity has been the chief variable examined with regards to scaffold strength. However, our results clearly demonstrate that it is also necessary to take into account the relative degree of fiber alignment present in an electrospun material. It is likely that subtle changes in alignment can be correlated with specific material properties and/or features that control cell phenotype. Structural properties are critical in determining wound resolution; the material properties felt by individual cells must initiate and allow normal cell processes to occur. For example, the stiffness of individual fibers has a significant impact in determining the differentiation of a fibroblast to a myofibroblast, a cell type that is critical with regards to wound closure [25]. In addition, the degree of alignment in a scaffold may direct cells in terms of phenotype or migratory processes. While much of our investigation centered on determining the point of induction and presence of alignment in a scaffold (a quality that is ideal for applications involving tendons and ligaments), the FFT technique can just as easily be used to observe the absence of alignment in a scaffold (a characteristic necessary for dermal applications).

Addressing the bulk structural properties of a scaffold is vital with regards to clinical relevance. A dermal template must allow for easy handling; this feature may be determined by a variety of considerations such as material identity, initial starting concentration (and consequently fiber and pore size) and scaffold thickness. However, the main point regarding clinical relevance is that a clinically-relevant scaffold must be one that is effortless with regards to clinician handling and implantation. A scaffold implant that is difficult to manage and maneuver will not encounter clinical success.

In addition to addressing scaffold structural issues, the work here examined the molecular properties and biological cues divulged to cells through scaffold material identity. Our efforts were focused on type I collagen, a protein native to the ECM that appears to impart unique biological properties to scaffold constructs [15]. While both extremes of non-denatured and denatured collagen have been examined, a study investigating the relative degree of collagen protein degradation and how this characteristic impacts biological processes had yet to be conducted. Based on our results, it appears that the actual degree of protein denaturation plays a role in directing cell processes and causes the exposure of cryptic RGD sites that then become available for integrin binding. This insight is crucial with regards to tissue injury and would resolution; if tissue injury causes collagen denaturation, the exposure of RGD binding sites to a cell may represent a signaling cue that is necessary for wound resolution. Although native non-denatured collagen is a highly regarded scaffold material, the placement of a dermal template composed of materials that represent a mature and healthy matrix into an immature wound bed may communicate the wrong message to cells that are awaiting signaling cues regarding wound remodeling. However, denatured collagen implant studies conducted in our laboratory resulted in significant inflammation while implanted collagen induced nominal, if any, inflammation (see figure 2.4) [15]. The most advantageous scaffold may be one that utilizes a mixture of both non-denatured and denatured collagen (as evidenced by our adhesion results when HDFs were plated onto a mixture of non-denatured collagen and collagen denatured at 50°C).

One of the most interesting aspects of this work was the examination of how the electrospinning process might alter collagen function. This inquiry was conducted by using our SDS gel electrophoresis and HDF assay results that utilized denatured collagen; the results from these proteins were used as a barometer to determine whether protein degradation was occurring during the electrospinning process. Overall, it appears that the electrospinning process does not degrade the collagen protein and does not significantly alter the biological cues presented to cells through matrix molecules. This result is critical in regards to understanding the structure and function of a scaffold material; if the fabrication technique is adversely altering the material, the actual identity, structure and function of the implanted material is unknown.

Overall, designing a scaffold that in any way mimics the role of the native ECM is an intricate and complicated task. In regards to wound resolution, a dermal template must support regular cell function and offer the correct biological cues; cells must be able to adhere and remodel the scaffold as they migrate across it, all the while undergoing proliferation to increase cell presence and differentiation into the correct cell type needed for eventual wound closure and resolution. The structural and functional characteristics investigated in this study must be addressed in order to fabricate a functional dermal template that improves wound resolution.

FUTURE DIRECTIONS

Future directions regarding this research should begin with further *in vitro* inquiry into the proteins and how they alter cell function. It would be interesting to explore cell remodeling (collagen synthesis and degradation) as a function of the thermally denatured proteins; further examination into scaffolds containing a mixture of both non-denatured and denatured proteins would also be useful. More specifically, the investigation of MMP expression of fibroblasts on the different proteins would provide insight into how these scaffolds may function *in vivo*. Additionally, examining cell function on these proteins when fully electrospun (not just coated onto nylon scaffolds) is necessary to examine how fiber diameter, pore size and material properties alter cell function on the proteins. Following *in vitro* investigations, *in vivo* experiments using the electrospun proteins would be the next phase. Dermal implantation of electrospun scaffolds composed of non-denatured, denatured and a mixture of non-denatured and denatured calfskin type I collagen proteins, followed by a wound bed histology examination, would yield realistic insights into scaffold function. Overall, the main direction of any further research should be to examine the functionality of scaffolds composed of both non-denatured and denatured collagen proteins and how this functionality may be exploited to promote scarless wound resolution. The cell penetration and non-inflammatory properties of non-denatured collagen scaffolds combined with the active remodeling characteristics observed on denatured collagen scaffolds may work in concert to improve wound resolution. Furthermore, it may also be valuable to investigate the addition of RGD peptides onto a non-denatured collagen electrospun scaffold. The addition and presence of these binding sites on a protein may provide the correct signaling cues to cells without the addendum of denatured collagen.

Literature Cited

Literature Cited

[1] Singer, AJ, Clark, RA. Cutaneous wound healing. N Engl J Med. 1999 Sep. 341(10):738-46.

[2] Wysocki, AB. Skin anatomy, physiology, and pathophysiology. Nurs Clin North Am. 1999 Dec. 34(4):777-97.

[3] Goldsmith, LA, ed. Biochemistry and Physiology of the Skin, Vol. 1. 1983. Oxford University Press: New York.

[4] Regnier, M, Caron, D, Reichert, U, Schaefer, H. Barrier function of human skin and human reconstructed epidermis. J Pharm Sci. 1993 Apr. 82[4):404-7.

[5] Daly, TJ. Contraction and Re-Epithelialization. Pp 32-46 **in** McCullock, JM, Kloth, LC and JA Feedar, eds. Wound Healing Alternatives in Management, 2nd ed. 1995. FA Davis, Philadelphia.

[6] Montagna, W, Parakkal, PF. The Structure and Function of Skin, 3rd ed. 1974. Academic Press, New York.

[7] Feedar, JA. Clinical Management of Chronic Wounds. Pp 137-185 **in** McCulloch, JM, Kloth, LC, and JA Feedar, eds. Wound Healing Alternatives in Management, 2nd ed. 1995. FA Davis, Philadelphia.

[8] Waldorf, H, Fewkes, J. Wound healing. Adv Dermatol. 1995. 10:77-96.

[9] Kielty, CM, Shuttleworth, CA. Microfibrillar elements of the dermal matrix. Microsc Res Tech. 1997 Aug. 38(4):413-27.

[10] Yannas, IV. Regeneration Templates. Bronzino, JD, ed. The Biomedical Engineering Handbook, 2nd ed. 2000. CRC Press, New York.

[11] Yannas, IV, Burke, JF. Design of an artificial skin. I. Basic design principles. J Biomed Mater Res. 1980 Jan. 14:65–81.

[12] Dagalakis, N, Flink, J, Stasikelis, P, Burke, JF, Yannis, IV. Design of an artificial skin. III. Control of pore structure. J Biomed Mater Res. 1980 Jul. 14(4): 511-28.

[13] Matthews, JA, Wnek, GD, Simpson, DG, Bowlin, GL. Electrospinning of collagen nanofibers. Biomacromolecules. 2002 Mar. 3(2):232-8.

[14] Ayres, CE, Bowlin, GL, Henderson, SC, Taylor, L, Shultz, J, Alexander, J, Telemeco, TA, Simpson, DG. Modulation of anisotropy in electrospun tissue engineering scaffolds: analysis of fiber alignment by the fast Fourier transform. Biomaterials. 2006 Nov. 27(32): 5524-34.

[15] Telemeco, TA, Ayres, CE, Bowlin, GL, Wnek, GE, Boland, ED, Cohen, NM, Baumgarten, CM, Matthews J, Simpson, DG. Regulation of cellular infiltration into tissue engineering scaffolds composed of submicron diameter fibers produced by electrospinning. Acta Biomater. 2005 Jul. 1(4):377-85.

[16] Ayres, CE, Jha, BS, Sell, SA, Bowlin, GL, Simpson, DG. Nanotechnology in the design of scaffolds: innovations in structure and function. Wiley Inter Rev Nanomed (Under review).

[17] Abraham, LC, Dice, JF, Lee, K, Kaplan, DL. Phagocytosis and remodeling of collagen matrices. Exp Cell Res. 2007 Mar. 313(5):1045-55.

[18] Nathan, C. Points of control in inflammation. Nature. 2002 Dec. 420(6917):846-52.

[19] Szpaderska, AM, DePietro, LA. Inflammation in surgical wound healing: friend or foe. Surgery. 2005 May. 137(5):571-3.

[20] Broughton, G, Janis, JE, Attinger, CE. The basic science of wound healing. Plast Reconstr Surg. 2006 Jun. 117(7):12S-34S.

[21] Werner, S, Grose, R. Regulation of wound healing by growth factors and cytokines. Physiol Rev. 2003 Jul. 83(3): 835-70.

[22] Nath, RK, LaRegina, M, Markham, H, Ksander, GA, Weeks, PM. The expression of TGF type beta in fetal and adult rabbit skin. J Pediatr Surg. 1994 Mar. 29(3):416-21.

[23] Sullivan, KM, Lorenz, HP, Meuli, M, Lin, RY, Adzick, NS. A model of scarless human fetal wound repair is deficient in transforming growth factor beta. J Pediatr Surg. 1995 Feb. 30(2):198-203.

[24] Ferguson, MWJ, O'Kane, S. Scar-free healing: From embryonic mechanisms to adult therapeutic intervention. Philos Trans R Soc Lond B Biol Sci. 2004 May. 359(1445): 8398-50.

[25] McAnulty, RJ. Fibroblasts and myofibroblasts: their source, function and role in

disease. Int J Biochem Cell Biol. 2006. 39(4): 666-71.

[26] Gabbiani, G, Hirschel, BJ, Ryan, GB, Statkov, PR, Majno, G. Granulation tissue as a contractile organ: A study of structure and function. J Exp Med 1972 Apr. 135(4): 719-34.

[27] Desmouliere, A, Geinoz, A, Gabbiani, F, Gabbiani, G. Transforming growth factor beta 1 induces α-smooth muscle actin expression in granulation tissue myofibroblasts and in quiescent and growing cultured fibroblasts. J Cell Biol. 1993 Jul. 122(1): 103–11.

[28] Chujo, S, Shirasaki, F, Kawara, S, Inagaki, Y, Kinbara, T, Inaoki, M, Takigawa, M, Takehara, K. Connective tissue growth factor causes persistent proalpha2(I) collagen gene expression induced by transforming growth factor-beta in a mouse fibrosis model. J Cell Physiol. 2005 May. 203(2):447-56.

[29] Asano, Y, Ihn, H, Yamane, K, Jinnin, M, Tamaki, K. Increased expression of integrin alphavbeta5 induces the myofibroblastic differentiation of dermal fibroblasts. Am J Pathol. 2006 Feb. 168(2):499-510.

[30] Dang, CM, Beanes, SR, Lee, H, Zhang, X, Soo, C, Ting, K. Scarless fetal wounds are associated with an increased matrix metalloproteinase to tissue derived inhibitor of metalloproteinase ratio. Plast Reconstr Surg. 2003 Jun. 111(7):2273-85.

[31] Huet, E, Vallee, B, Szul, D, Verrecchia, F, Mourah, S, Jester, JV, Hoang-Xuan, T, Menashi, S, Gabison, EE. Extracellular matrix metalloproteinase inducer/CD147 promotes myofibroblast differentiation by inducing α-smooth muscle actin expression and collagen gel contraction: Implications in tissue remodeling. FASEB J. 2008 Apr. 22(4):1144-54.

[32] Metz, CN. Fibrocytes: a unique cell population implicated in wound healing. Cell Mol Life Sci. 2006 Jul. 60(7):1342-50.

[33] Abe, R, Donnelly, SC, Peng, T, Bucala, R, Metz, CN. Peripheral blood fibrocytes: differentiation pathway and migration to wound sites. Immunol. 2001 Jun. 166(12):7556–62.

[34] Hinz, B. Formation and function of the myofibroblast during tissue repair. J Invest Dermatol. 2007 Mar. 127(3):526-37.

[35] Desmouliere, A, Chaponnier, C, Gabbiani, G. Tissue repair, contraction and the myofibroblast. 2005 Jan-Feb. Wound Rep Reg. 13(1):7-12.

[36] Tomasek, JJ, Vaughan, MB, Kropp, BP, Gabbiani, G, Martin, MD, Haaksma, CJ, Hinz, B. Contraction of myofibroblasts in granulation tissue is dependent on

Rho/Rhokinase/myosin light chain phosphatase activity. 2006 May-Jun. Wound Rep Reg. 14: 313-20.

[37] Clark, R.A., et al. Fibronectin and fibrin provide a provisional matrix for epidermal cell migration during wound reepithelialization. J Invest Dermatol. 79(5): 264-269 (1982).

[38] Cook, H, Stephens, P, Davies, KJ, Harding, KG, Thomas, DW. Defective ECM reorganization by chronic wound fibroblasts is associated with alterations in TIMP-1, TIMP-2 and MMP-2 activity. J Invest Dermatol. 2000. 115(2): 225-33.

[39] Colwell, AS, Krummel, TM, Longaker, MT, Lorenz, HP. Fetal and adult fibroblasts have similar TGF-beta-mediated, Smad-dependent signaling pathways. Plast Reconstr Surg. 2006 Jun. 117(7): 2277-83.

[40] Smith, PC, Caceres, M, Martinez, J. Induction of the myofibroblastic phenotype in human gingival fibroblasts by transforming growth factor-β1: role of RhoA-Rock and c-Jun N-terminal kinase signaling pathways. J Periodont Rest. 2006 Oct. 41:418-25.

[41] Barnes, CP, Sell, SA, Boland, ED, Simpson, DG, Bowlin, GL. Nanofiber technology: designing the next generation of tissue engineering scaffolds. Adv. Drug. Deliv. Rev. 2007 Dec. 59(14):1413-33.

[42] Boland, ED, Espy, PG, Bowlin, GL. Tissue Engineering Scaffolds. Pp 1630-8 **in** Bowlin, GL and GE Wnek, eds. Encyclopedia of Biomaterials and Biomedical Engineering. 2004. Marcel Dekker, New York.

[43] Sell, SA, McClure, MJ, Barnes, CP, Knapp, DC, Walpth, BH, Simpson, DG, Bowlin, GL. Electrospun polydioxanone elastin blends: potential for bioresorbable vascular grafts. Biomed. Mater. 2006 Jun. 1:72-80.

[44] Simpson, DG, Terracio, L, Terracio, M, Price, RL, Turner, DC, Borg, TK. Modulation of cardiac myocyte phenotype in vitro by the composition and orientation of the extracellular matrix. J. Cell. Physiol. 1994 Oct. 161(1):89-105.

[45] Simpson, DG, Majeski, M, Borg, TK, Terracio, L. Regulation of cardiac protein turnover and myofibrillar structure in vitro by specific directions of stretch. Circ. Res. 1999 Nov. 85(10):e59-69.

[46] Ma, Z, Kotaki, M, Inai, R, Ramakrishna, S. Potential of nanofiber matrix as tissue-engineering scaffolds. Tissue Eng. 2005 Jan-Feb. 11(1-2):101-9.

[47] Vasita, R, Khatti, DS. Nanofibers and their applications in tissue engineering. Int. J. Nanomedicine. 2006. 1(1):15-30.

[48] Zhang, S. Fabrication of novel biomaterials through molecular self-assembly. Nat. Biotechnol. 2003 Oct. 21(10):1171-8.

[49] Hosseinkhani, H, Hosseinkhani, M. Kobayashi, H. Proliferation and differentiation of mesenchymal stem cells using self-assembled peptide amphiphile nanofibers. Biomed. Mater. 2006 Mar. 1(1):8-15.

[50] Stendahl, JC, Wang, LJ, Chow, LW, Kaufman, DB, Stupp, SI. Growth factor delivery from self-assembling nanofibers to facilitate islet transplantation. Transplantation. 2008 Aug. 86(3):478-81.

[51] Sargeant, TD, Guler, MO, Oppenheimer, SM, Mata, A, Satcher, RL, Dunand, DC, Stupp, SI. Hybrid bone implants: self-assembly of peptide amphiphiles nanofibers within porous titanium. Biomaterials. 2008 Jan. 29(2):161-71.

[52] Ma, PX, Zhang, R. Synthetic nano-scale fibrous extracellular matrix. J. Biomed. Mater. Res. 1999 Jul. 46(1):60-72.

[53] Zhang, R, Ma, PX. Synthetic nano-fibrillar extracellular matrices with predesigned macroporous architectures. J. Biomed. Mater. Res. 2000 Nov. 52(2):430-8.

[54] Chen, VJ, Ma, PX. Nano-fibrous poly(L-lactic acid) scaffolds with interconnected spherical macropores. Biomaterials. 2004 May. 25(11):2065-73.

[55] Fromstein, JD, Zandstra PW, Alperin C, Rockwood D, Rabolt JF, Woodhouse KA. Seeding bioreactor-produced embryonic stem cell-derived cardiomyocytes on different porous, degradable, polyurethane scaffolds reveals the effect of scaffold architecture on cell morphology. Tissue Eng. Part A. 2008 Mar. 14(3):369-78.

[56] Huang, YX, Ren, J, Ren, TB, Zhou, XY. Preparation and properties of poly(lactide-co-glycolide) (PLGA) / nano-hydroxyapatite (NHA) scaffolds by thermally induced phase separation and rabbit MSC's culture on scaffolds. J. Biomater. Appl. 2008 Mar. 22(5):409-32.

[57] Cao, Y, Zhang, B, Croll, T, Rolfe, BE, Campbell, JH, Campbell, GR, Martin, D, Cooper-White, JJ. Engineering tissue tubes using novel multilayered scaffolds in the rat peritoneal cavity. J. Biomed. Mater. Res. A. 2008 Dec. 87(3):719-27.

[58] Cui, T, Yan, Y, Zhang, R, Liu, L, Xu, W, Wang, X. Rapid prototyping of a double-layer polyurethane-collagen conduit for peripheral nerve regeneration. Tissue Eng. Part C Methods. 2008 Oct (EPub ahead of print).

[59] Berndt, P, Fields, GB, Tirrell, M. Synthetic lipidation of peptides and amino acids: monolayer structure and properties. J. Am. Chem. Soc. 1995. 117(37):9515-22.

[60] Manis, AE, Bowman, JR, Bowlin, GL, Simpson, DG. Electrospun nitrocellulose and nylon: design and fabrications of novel high performance platforms for protein blotting applications. J. Biol. Eng. 2007 Oct. 1(2).

[61] Boland, ED, Matthew, JA, Pawlowski, KJ, Simpson, DG, Wnek, GE, Bowlin, GL. Electrospinning collagen and elastin: preliminary vascular tissue engineering. Front. Biosci. 2004 May. 1(9):1422-32.

[62] Wnek, GE, Carr, ME, Simpson, DG, Bowlin, GL. Electrospinning of nanofiber fibrinogen structures. Nano Letters. 2003 Feb. 3(2):213-6.

[63] Ayres, CE, Bowlin, GL, Pizinger, R, Taylor, LT, Keen, CA, Simpson, DG. Incremental changes in anisotropy induce incremental changes in the material properties of electrospun scaffolds. Acta Biomater. 2007 Sep. 3(5):651-61.
[64] Barnes, CP, Pemble, CW, Brand, DD, Simpson, DG, Bowlin, GL. Cross-linking electrospun type II collagen tissue engineering scaffolds with carbodiimide in ethanol. Tissue Eng. 2007 Jul. 13(7): 593-1605.

[65] McManus, MC, Boland, ED, Simpson, DG, Barnes, CP, Bowlin GL. Mechanical properties of electrospun fibrinogen structures. Acta Biomater. 2006 Jan. 2(1):19-28.

[66] Simpson, DG, Bowlin, GL. Tissue-engineering scaffolds: can we re-engineer mother nature? Expert Rev. Med. Devices. 2006 Jan. 3(1):9-15.

[67] Abraham, LC, Dice, JF, Finn, PF, Mesires, NT, Lee, K, Kaplan, DL. Extracellular matrix remodeling- methods to quantify cell-matrix interactions. Biomaterials. 2007 Jan. 28(2):151-61.

[68] Karamichos, D, Brown, RA, Mudera, V. Collagen stiffness regulates cellular contraction and matrix remodeling gene expression. J. Biomed. Mater. Res. A. 2007 Dec. 78(2):406-15.

[69] Lu, H, Zhang, T, Wang, XP, Fang, QF. Electrospun submicron bioactive glass fibers for bone tissue scaffold. J. Mater. Sci. Mater. Med. 2008 Nov (Epub before print).

[70] Zoccola, M, Aluigi, A, Vineis, C, Tonin, C, Ferrero, F, Piacentino, MG. Study on cast membranes and electrospun nanofibers made from keratin/fibroin blends. Biomacromolecules. 2008 Oct. 9(10):2819-25.

[71] Yeo, IS, Oh, JE, Jeong, L, Lee, TS, Lee, SJ, Park, WH, Min, BM. Collagen-based biomimetic nanofibrous scaffolds: preparation and characterization of collagen/silk

fibroin bicomponent nanofibrous structures. Biomacromolecules. 2008 Apr. 9(4):1106-16.

[72] Yao, C, Li, X, Song, T. Fabrication of zein/hyaluronic acid fibrous membranes by electrospinning. J. Biomater. Sci. Polym. Ed. 2007. 18(6):731-42.

[73] Panseri, S, Cunha, C, Lowery, J, Del Carro, U, Taraballi, F, Amadio, S, Vescovi, A, Gelain, F. Electrospun micro- and nanofiber tubes for functional nervous regeneration in sciatic nerve transactions. BMC Biotechnol. 2008 Apr. 8:39.

[74] Heydarkhan-Hagvall, S, Schenke-Layland, K, Dhanasopon, AP, Rofail, F, Smith, H, Wu, BM, Shemin, R, Beygui, RE, MacLellan, WR. Three-dimensional electrospun ECM-based hybrid scaffolds for cardiovascular tissue engineering. Biomaterials. 2008 Jul. 29(19):2907-14.

[75] Choi, JS, Lee, SJ, Christ, GJ, Atala, A, Yoo, JJ. The influence of electrospun aligned poly(epsilon-caprolactone)/collagen nanofiber meshes on the formation of self-aligned skeletal muscle myotubes. Biomaterials. 2008 Jul. 29(19):2899-906.

[76] Ko, EK, Jeong, SI, Rim, NG, Lee, YM, Shin, H, Lee, BK. In vitro osteogenic differentiation of human mesenchymal stem cells and in vivo bone formation in composite nanofiber meshes. Tissue Eng. Part A. 2008 Dec. 14(12):2105-19.

[77] Kowalczyk, T, Nowicka, A, Elbaum, D, Kowalewski, TA. Electrospinning of bovine serum albumin. Optimization and the use for production of biosensors. Biomacromolecules. 2008 Jul. 9(7):2087-90.

[78] Zhang, YZ, Venugopal, J, Huang, ZM, Lim, CT, Ramakrishna, S. Characterization of the surface biocompatibility of the electrospun PCL-collagen nanofibers using fibroblasts. Biomacromolecules. 2005 Sep-Oct. 6(5):2583-9.

[79] Duan, Y, Wang, Z, Yan, W, Wang, S, Zhang, D, Jia, J. Preparation of collagen-coated electrospun nanofibers by remote plasma treatment and their biological properties. J. Biomater. Sci. Polym. Ed. 2007. 18(9):1153-64.

[80] Li, X, Xie, J, Yuan, X, Xia, Y. Coating electrospun poly(epsilon-caprolactone) fibers with gelatin and calcium phosphate and their use as biomimetic scaffolds for bone tissue engineering. Langmuir. 2008 Dec. 24(24):14145-50.

[81] Zhu, Y, Cui, W, Li, X, Jin, Y. Electrospun fibrous mats with high porosity as potential scaffolds for skin tissue engineering. Biomacromolecules. 2008 Jul. 9(7): 1795-801.

[82] Jia, J, Duan, YY, Yu, J, Lu, JW. Preparation and immobilization of soluble eggshell membrane protein on the electrospun nanofibers to enhance cell adhesion and growth. J. Biomed. Mater. Res. A. 2008 Aug. 86(2): 364-73.

[83] Ayres, CE, Jha, BS, Meredith, H, Bowman, JR, Bowlin, GL, Henderson, SC, Simpson, DG. Measuring fiber alignment in electrospun scaffolds: a user's guide to the 2D fast fourier transform approach. J. of Biomater. Sci. Polym. Ed. 2008. 19(5):603-21.

[84] Chow, WN, Simpson, DG, Bigbee, JW, Colello, RJ. Evaluating neuronal and glial growth on electrospun polarized matrices: bridging the gap in percussive spinal cord injuries. Neuron Glia Biol. 2007 May. 3(2):119-26.

[85] Soffer, L, Wang, X, Zhang, X, Kluge, J, Dorfmann, L, Kaplan, DL, Leisk, G. Silk-based electrospun tubular scaffolds for tissue-engineered vascular grafts. J. Biomater. Sci. Polym. Ed. 2008. 19(5):653-64.

[86] Wang, WB, Mullins, ME, Cregg, JM, Hurtado, A, Oudega, M, Trombley, MT, Gilbert, RJ. Creation of highly aligned electrospun poly-L-lactic acid fibers for nerve regeneration applications. J. Neural Eng. 2009 Feb. 6(1):16001.

[87] Matsuda, T, Kawahara, D. Electrospinning fabrication of high-trackable catheter tip with gradually graded or gradient flexibility. J. Biomed. Mater. Res. B Appl. Biomater. 2008 Oct. 87(1):35-41.

[88] Leong, MF, Rasheed, MZ, Lim, TC, Chian, KS. In vitro cell infiltration and in vivo cell infiltration and vascularization in a fibrous, highly porous poly(D,L-lactide) scaffold fabricated by cryogenic electrospinning technique. J. Biomed. Mater. Res. A. 2008 Sept (Epub ahead of print).

[89] Newton, D, Mahajan, R, Ayres, CE, Bowman, JR, Bowlin, GL, Simpson, DG. Regulation of material properties in electrospun scaffolds: role of cross-linking and fiber tertiary structure. Acta Biomater. 2009 Jan. 5(1):518-29.

[90] Jayakrishnan, A, Jameela, SR. Glutaraldehyde as a fixative in bioprostheses and drug delivery matrices. Biomaterials. 1996 Mar. 17(5): 471-84.

[91] van Aalst, JA, Reed, CR, Han, L, Andrady, T, Hromadka, M, Bernacki, S, Kolappa, K, Collins, JB, Loboa, EG. Cellular incorporation into electrospun nanofibers: retained viability, proliferation, and function in fibroblasts. Ann. Plast. Surg. 2008 May. 60(5):577-83.

[92] Fu, YC, Nie, H, Ho, ML, Wang, CK, Wang, CH. Optimized bone regeneration based on sustained release from three-dimensional fibrous PLGA/HAp composite scaffolds loaded with BMP-2. Biotechnol. Bioeng. 2008 Mar. 99(4):996-1006.

[93] Ranganath, SH, Wang, CH. Biodegradable microfiber implants delivering paclitaxel for post-surgical chemotherapy against malignant glioma. Biomaterials. 2008 Jul. 29(20):2996-3003.

[94] Hong, Y, Fujimoto, K, Hashizume, R, Guan, J, Stankus, JJ, Tobita, K, Wagner, WR. Generating elastic, biodegradable polyurethane/poly(lactide-co-glycolide) fibrous sheets with controlled antibiotic release via two-stream electrospinning. Biomacromolecules. 2008 Apr. 9(4):1200-7.

[95] Maretschek, S, Greiner, A, Kissel, T. Electrospun biodegradable nanofiber nonwovens for controlled release of proteins. J. Control. Release. 2008 Apr. 127(2):180-7.

[96] Baker, BM, Gee, AO, Metter, RB, Nathan, AS, Marklein, RA, Burdick, JA, Mauck, RL. The potential to improve cell infiltration in composite fiber-aligned electrospun scaffolds by the selective removal of sacrificial fibers. Biomaterials. 2008 May. 29(15):2348-58.

[97] Zeugolis, DI, Khew, ST, Yew, ES, Ekaputra, AK, Tong, YW, Yung, LY, Hutmacher, DW, Sheppard, C, Raghunatch, M. Electrospinning of pure collagen nano-fibres: just an expensive way to make gelatin? Biomaterials. 2008 May. 29(15):2293-305.

[98] Dong, B, Arnoult, O, Smith, ME, Wnek, GE. Electrospinning of collagen nanofiber scaffolds from benign solvents. Micromol Rapid Commun. 2009 Feb. 30(7):539-542.

[99] Klinkhammer, K, Seiler, N, Grafahrend, D, Gerardo-Nava, J, Mey, J, Brook, GA, Moller, M, Dalton, PD, Klee, D. Deposition of electrospun fibers on reactive substrates for in vitro investigations. 2009 Mar. 15(1):77-85.

[100] Pham, QP, Sharma, U, Mikos, AG. Electrospun poly(epsilon-caprolactone microfiber and multilayer nanofiber/microfiber scaffolds: characterization of scaffolds and measurement of cellular infiltration. Biomacromolecules. 2006 Oct. 7(10):2796-805.

[101] Yang, X, Shah, JD, Wang, H. Nanofiber enabled layer-by-layer approach toward three-dimensional tissue formation. Tissue Eng Part A. 2008 Sept (EPub before print).

[102] Zhou, M, Smith, M, Das, AK,Hodson, NW, Collins, RF, Ulijn, RV, Gough, JE. Self-assembled peptide-based hydrogels as scaffolds for anchorage dependent cells. Biomaterials. 2009 May. 30(13):2523-30.

[103] Kraehenbuehl, TP, Zammaretti, P, Van der Vlies, AJ, Schoenmakers, RG, Lutolf, MP, Jaconi, ME, Hubbell, JA. Three-dimensional extracellular matrix directed

cardioprogenitor differentiation: systematic modulation of a synthetic cell-responsive PEG hydrogel. Biomaterials. 2008 Jun. 29(18):2757-55.

[104] Park, Y, Lutolf, MP, Hubbell, JA, Hunziker, EB, Wong, M. Bovine primary chondrocyte culture in synthetic matrix metalloproteinase-sensitive poly(ethylene glycol)-based hydrogels as a scaffold for cartilage repair. Tissue Eng. 2004 Mar-Apr. 10(3-4):515-22.

[105] Boland, ED, Wnek, GE, Simpson, DG, Pawlowski, KJ, Bowlin, GL. Tailoring Tissue Engineering Scaffolds Using Electrostatic Processing Techniques: A Study of Poly(Glycolic Acid). J Macromol Sci. 2001 Nov. 38(12):1231-43.

[106] Boland, ED, Coleman, BD, Barnes, CP, Simpson, DG, Wnek, GE, Bowlin, GL. Electrospinning polydioxanone for biomedical applications. Acta Biomater. 2005 Jan. 1(1):115-23.

[107] Frenot, A, Chronakis, S. Polymer nanofibers assembled by electrospinning. Curr Opin Colloid Interface Sci. 2003. 8(1):64-75.

[108] Courtney, T, Sacks, MS, Stankus, J, Guan, J, Wagner, WR. Design and analysis of tissue engineering scaffolds that mimic soft tissue mechanical anisotropy. Biomaterials. 2006 Jul. 27(19):3631-8.

[109] Kessick, R, Fenn, J, Tepper, G. The use of AC potentials in electrospraying and electrospinning processes. Polymer. 2004. 45:2981-4.

[110] Yang, F, Murugan, R, Wang, S, Ramakrishna, S. Electrospinning of nano/micro scale poly(L-lactic acid) aligned fibers and their potential in neural tissue engineering. Biomaterials. 2005 May. 26(15):2603-10.

[111] Sacks, MS, Smith, DB, Hiester, ED. A small angle light scattering device for planar connective tissue microstructural analysis. Ann Biomed Eng. 1997 Jul. 25(4):678–89.

[112] Sacks, MS, Schoen, FJ. Collagen fiber disruption occurs independent of calcification in clinically explanted bioprosthetic heart valves. J Biomed Mater Res. 2002 Dec. 62(3):359-71.

[113] Moell, MK, Fujita, M. Fourier transform methods in image analysis of compression wood at the cellular level. IAWA J. 2004. 25(3):311-2.

[114] van Zuijen, PP, de Vries, HJ, Lamme, EN, Coppens, JE, can Marle, J, Kreis, RW, Middelkoop, E. Morphometry of dermal collagen orientation by Fourier analysis is superior to multi-observer assessment. J Pathol. 2002; 198(3):284-91.

[115] Karlon, WJ, Covell, JW, McCulloch, AD, Hunter, JJ, Omens, JH. Automated measurement of myofiber disarray in transgenic mice with ventricular expression of ras. Anat Rec. 1998 Dec. 252(4):612–25.

[116] Leong, FJ, Brady, M, McGee, JQ. Correction of uneven illumination (vignetting) in digital microscopy images. J Clin Pathol. 2003. 56:619-21.

[117] Doshi, J, Reneker, DH. Electrospinning process and applications of electrospun fibers. J Electrostatics. 1995 Aug. 35(2-3):151-60.

[118] Deitzel, JM, Kleinmeyer, J, Harris, D, Tan, NCB. The effect of processing variables on the morphology of electrospun nanofibers and textiles. Polymer 2001 Jan. 42(1):261-72.

[119] Kenawy, E., Mansfield, K., Bowlin, G.L., Simpson, D.G. and G.E. Wnek. Release of tetracycline hydrochloride from electrospun poly(ethylene-co-vinylacetate), poly(lactic acid), and a blend. J Control Release. 2002 May. 81(1-2):57-64.

[120] Landmann, L, Marbet, P. Colocalization analysis yields superior results after image restoration. Micro Res Tech. 2004. 64(2):103-12.

[121] Simpson, DG. Dermal regeneration and the wound healing paradigm: the promise of tissue regeneration. Expert Rev Med Dev. 2006 Jul. 3(4):471-84.

[122] Boland, ED, Telemeco, TA, Simpson, DG, Wnek, GE, Bowlin, GL. Utilizing acid pretreatment and electrospinning to improve biocompatibility of poly (glycolic acid) for tissue engineering. J Biomed Mater Res B Appl Biomater. 2004 Oct. 71(1):144-52.

[123] Kim, K, Yu, M, Zong, X, Chiu, J, Fang, D, Seo, YS, Hsiao, BS, Chu, B, Hadjiargyrou, M. Control of degradation rate and hydrophilicity in electrospun non-woven poly(D.L-lactide) nanofiber scaffolds for biomedical applications. Biomaterials 2003 Dec. 24(27):4977-85.

[124] Matthews, JA, Boland, ED, Wnek, GE, Simpson, DG, Bowlin, GL. Electrospinning of collagen type II: a feasibility study. J Bioactive Comp Polym. 2003 Mar. 18(2):125-34.

[125] Alexander, JK, Fuss, B, Colello, RJ. Electric field-induced astrocyte alignment directs neurite outgrowth. Neuron Glia Biol. 2006 May. 2(2):93-103.

[126] Koombhongse, S, Wenxial, L, Reneler, DH. Flat Polymer Ribbons and Other Shapes by Electrospinning. J Polym Sci. 2001 Nov. 39(21):2598-606.

[127] Fridrikh, SV, Yu, JH, Brenner, MP, Rutledge, GC. Controlling the fiber diameter during electrospinning. Phys Rev Lett. 2003 Apr. 90(14):144502.1-144502.4.

[128] Baumgarten PK. Electrostatic spinning of acrylic microfibres. J Coll Interface Sci. 1971 May. 36(1):71-9.

[129] Vaz, CM, van Tuijl, S, Bouten, CVC, Baaijens, FPT. Design of scaffolds for blood vessel tissue engineering using a multi-layering electrospinning technique. Acta Biomater. 2005 Sept. 1(5):575-82.

[130] Keen, C, Wnek, GE, Baumgarten, CM, Newton, D, Bowlin, GL, Simpson, DG. Bioengineered Skeletal Muscle. Pp 1639-51 **in** Wnek, GE, and Bowlin, GL, eds. Encyclopedia of Biomaterials and Biomedical Engineering. 2004. Marcel Dekker. New York.

[131] Subbiah, T, Bhat, GS, Tock, RW, Parameswaran, S, Ramkumar, SS. Electrospinning of nanofibers. J Appl Poly Sci. 2005 Apr. 96(2):557-69.

[132] Thandavmoorthy, S, Gopinath, S, Ramkumar, S. Self-assembled honeycomb polyurethane nanofibers. J Appl Poly Sci. 2006 Sept. 101(5):3121-4.

[133] Sanders, EH, Kloefkorn, R, Bowlin, GL, Simpson, DG, Wnek, GE. Two phase electrospinning from a single electrified jet: microencapsulation of aqueous reservoirs in poly(ethylene-co-vinyl acetate) fibers. Macromolecules. 2003. 36(11):3803-5.

[134] Martins-Green, M. The Dynamics of Cell-ECM Interactions with Implications for Tissue Engineering. Principles of Tissue Engineering. Pp 23-46 in Lanza, R, Langer, R, and W Chick, eds. 1997. RG Landes Company, New York.

[135] Bigi, A, Panzavolta, S, Rubini, K. Relationship between triple-helix content and mechanical properties of gelatin films. Biomaterials, 2004 Nov. 25(25):5675-80.

[136] Abraham, LC, Vorrasi, J, Kaplan, DL. Impact of collagen structure on matrix trafficking by human fibroblasts. J Biomed Mater Res A. 2004 Jul. 70(1):39-48.

[137] Xu, J, Clark, RA. Extracellular matrix alters PDGF regulation of fibroblast integrins. J Cell Biol. 1996 Jan. 132(1-2):239-49.

[138] Davis, GE. Affinity of integrins for damaged extracellular matrix: alpha v beta 3 binds to denatured collagen type I through RGD sites. Biochem Biophys Res Commun. 1992 Feb. 182(3):1025-31.

[139] Sun, Y, Chen, WL, Lin, SJ, Jee, SH, Chen, YF, Lin, LC, So, PTC, Dong, CY. Investigating mechanisms of collagen thermal denaturation by high resolution second harmonic generation imaging. Biophys J. 2006 Oct. 91(7):2620-5.

[140] Agrez, MV, Bates, RC, Boyd, AW, Burns GF. Arg-Gly-Asp-containing peptides expose novel collagen receptors on fibroblasts: implications for wound healing. Cell Regul. 1991 Dec. 2(12):1035-44.

[141] Barrientos, S, Stojadinovic, O, Golinko, MS, Brem, H, Tomic-Canic, M. Growth factors and cytokines in wound healing. Wound Repair Regen. 2008 Sep-Oct. 16(5):585-601.

[142] Monteiro, GA, Fernandes, AV, Sundararaghaven, HG, Shreiber, DI. Positively and negatively modulating cell adhesion to type I collagen via peptide grafting. Tissue Eng Part A. 2009 Jan (Epub ahead of print).

[143] Sykes, B, Puddle, B, Francis, M, Smith, R. The estimation of two collagens from human dermis by interrupted gel electrophoresis. Biochem Biophys Res Commun. 1976 Oct. 72(4):1472-80.

APPENDIX A

Control of Fiber Alignment: Electrospinning Voltage and Air Gap Distance

Preface: The work included in Appendix A was originally conducted for the manuscript found in chapter 4 titled “Modulation of anisotropy in electrospun tissue-engineering scaffolds: analysis of fiber alignment by the fast Fourier transform”. However, length constraints prompted the removal of the results from the published manuscript. This work demonstrates the effect of electrospinning voltage and air gap distance on the induction of anisotropy in electrospun scaffolds.

MATERIALS AND METHODS

Electrospinning. Reagents were purchased from Sigma Aldrich (St. Louis, MO) unless noted. Gelatin was suspended in 2,2,2 trifluoroethanol (TFE) for 48 hr prior to electrospinning. Starting concentrations of 130 mg/ml TFE were prepared. Suspensions were electrospun onto a stainless steel rectangular mandrel (70 mm x 10 mm x 5 mm) as previously described. The gelatin solution was delivered at a rate of 21 ml/hr and the target mandrel speed was set to 4000 RPM (this speed was chosen to maximize fiber alignment). A digital stroboscope (Shimpo Instruments DT3-11A) was used to continuously monitor the RPM of the target mandrel. Samples were stored in a desiccation chamber prior to analysis.

Light Microscopy. All imaging and materials testing was conducted with dry, unfixed samples. This approach was selected to allow us to make direct comparisons between the different analytical approaches described in this study. Dry sheets of electrospun gelatin were cut into 10 mm diameter disks using a circular biopsy punch. Samples were imaged with a Nikon TE300 microscope equipped with a Nikon DXM 1200 digital camera. Images (3840 x 3072 pixels) were captured with a 20X (0.40 n.a.) bright field objective lens, resulting in pixel dimensions of 0.17 x 0.18 μm.

Fast Fourier Transform (FFT). Digitized bright field light microscopic images were converted to 8-bit grayscale .TIF files and cropped to 2048 x 2048 pixels. Images were processed using ImageJ software (NIH, http://rsb.info.nih.gov/ij) as previously described. All FFT data was normalized to a baseline value of 0 and plotted in arbitrary units, allowing different data sets to be directly compared.

RESULTS

We used FFT analysis to examine how electrospinning variables, namely voltage and air gap distance, impact scaffold structure. To test the effects of voltage, a gelatin solution was electrospun over an air gap distance of 20 cm and the voltage applied when electrospinning each individual scaffold was 10, 15, 22 or 30 kV. Electrospun fibers formed at each voltage tested. The FFT alignment values increased as a function of voltage and reached nearly 0.10 units in scaffolds electrospun at 30 kV (Figure A.1 top). We have previously reported that the evolution of an aligned scaffold begins at approximately 0.05 FFT units, thus the electrospinning solutions charged to 10 and 15 kV failed to produce scaffolds composed of aligned elements (these scaffolds had FFT values of approximately 0.04 units) even under other theoretically ideal conditions (large starting concentration and high mandrel speed). Scaffolds produced from electrospinning solutions charged to 20, 25 and 30 kV all produced scaffolds made up of aligned fibers (0.07, 0.08 and 0.09 FFT units, respectively).

To examine how air gap distance affects scaffold structure, a gelatin solution was electrospun at a voltage of 30 kV over an air gap distance 5, 10, 15, 20, 25 or 30 cm for each individual scaffold. Scaffolds electrospun over an air gap distance of 5 and 30 cm produced scaffolds composed of random elements; the FFT values for these scaffolds were 0.03 and 0.04 units, respectively (Figure A.1 bottom). Scaffolds electrospun across an air gap of 10, 15, 20 and 25 cm demonstrated alignment values that increased sequentially with greater air gap distance. The scaffold electrospun over 10 cm had an intermediate alignment value of 0.07 units and the scaffolds electrospun across an air gap of 15 and 20 cm demonstrated FFT alignment values of 0.09 units. FFT alignment peaked at an air gap distance of 25 cm with an FFT alignment value of 0.1 units.

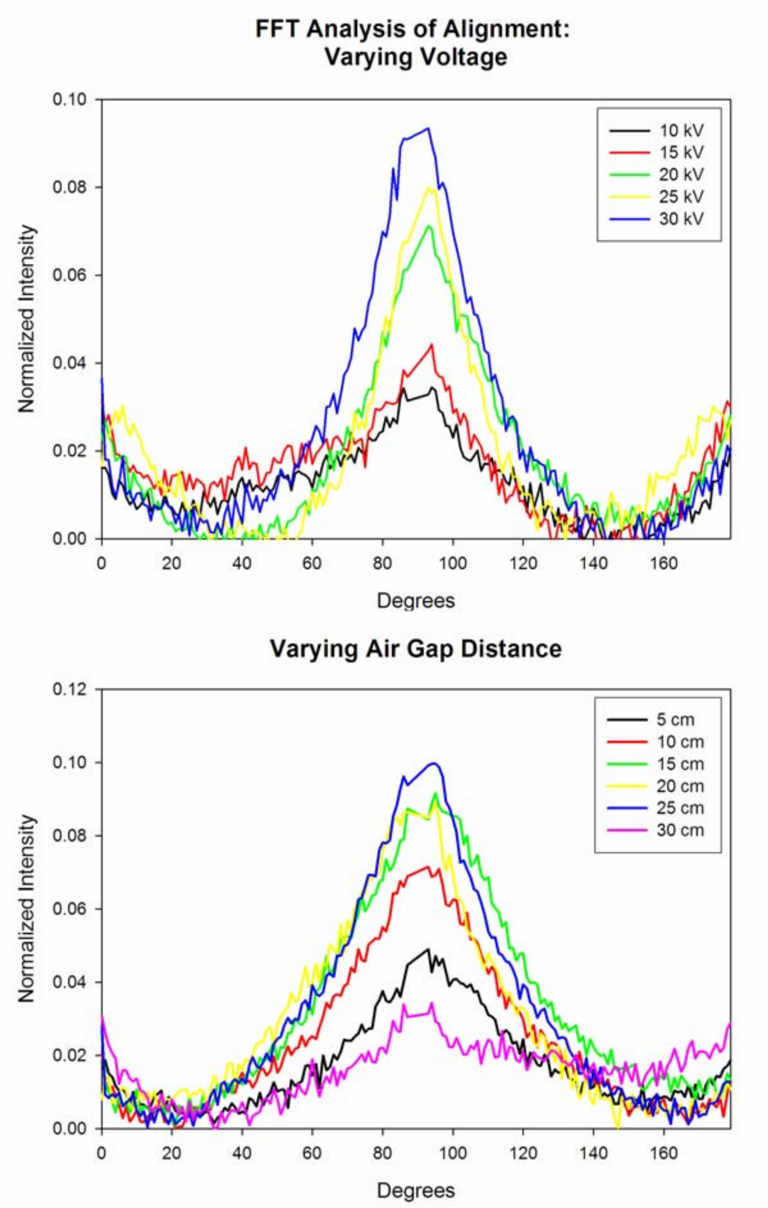

Figure A.1. Electrospun gelatin scaffold (130 mg/ml) alignment as a function of varying voltage (top) and air gap distance (bottom). Degree of alignment improved sequentially as voltage increased and air gap distance lengthened.

DISCUSSION

We propose that interactions between local movements within the charged jet and the overall trajectory of a forming fiber underlie the induction of scaffold anisotropy in our electrospinning system. A charged electrospinning jet grossly follows a spiraling pathway across the air gap. Bending instabilities develop in the forming fiber, leading to the formation of small scale loops. In response to solvent evaporation and increased charge density these loops elongate and thin in parallel with the longitudinal axis of the forming fiber. Loop formation and elongation are believed to occur sequentially, and repeatedly, along the forming fiber for as long as charge repulsions can overcome the viscosity of the drying jet.

Increasing the electrospinning voltage and air gap distance induced a higher degree of alignment into the scaffolds, indicating that an increased charge and greater air gap distance aids in dampening the whipping motions of an electrospun fiber. However, alignment was not induced for solutions charged to low voltages (10 and 15 kV), indicating that the charge was not large enough to control and direct the fiber across the electrospinning air gap. It is likely that the fibers did not have a large charge density and were thus approaching and depositing onto the mandrel in a loop formation from a number of directions, thus created a scaffold composed of random elements. Alignment was also not achieved for solutions electrospun over a very short (5 cm) or long (30 cm) air gap distance, results that may be attributed to solvent evaporation. A fiber moving across the air gap toward a close target is likely still wet and at a very high potential when it reaches the mandrel; a fiber in this state has not had enough time to dry and elongate as it approaches the mandrel for deposition. Conversely, a fiber moving across the air gap toward a distant target may have dried some time ago and would act similar to a fiber only charged to 10 or 15 kV.

Overall, small diameter fibers undergo high velocity, erratic, whipping motions in the electrospinning air gap. These motions are associated with a considerable degree of radial displacement of the charged jet from the central electrospinning axis as the forming fiber traverses the spiral pathway. These macroscopic deviations from the central electrospinning axis “present” the fiber to the target mandrel in a variety of different orientations. Local bending instabilities further degrade alignment, especially at low mandrel RPM. Apparently, evidence of these small scale instabilities may be partially preserved in the tortuous profile that small diameter fibers can exhibit upon deposition onto the target mandrel. At higher RPMs, fiber tortuosity may be reduced to some degree; however, as a population, overall fiber alignment is nominal. In the electrospinning of larger diameter fibers, the increased inertia and mass of the charged jet/forming fiber appears to dampen the radial displacement of the spiral pathway. This allows large diameter fibers to take a nearly linear trajectory across the electrospinning air gap. The mass of large diameter fibers also appears to suppress the formation of local bending instabilities, resulting in a nearly linear fiber at deposition.

APPENDIX B

Modulation of Electrospun Scaffolds through Cross-Linking

Preface: The work included in Appendix B was originally conducted for a manuscript published in Acta Biomaterialia, 2009, volume 5, pages 518-529, titled "Regulation of material properties in electrospun scaffolds: role of cross-linking in fiber tertiary structure", authored by D Newton[1], R Mahajan[1], CE Ayres[2], JR Bowman[3], GL Bowlin[2] and DG Simpson[3]. This work explores how cross-linking modulates the material properties of an electrospun scaffold.

[1]School of Medicine
Virginia Commonwealth University
Richmond, VA 23298

[2]Department of Biomedical Engineering
Virginia Commonwealth University
Richmond, VA 23284

[3]Department of Anatomy and Neurobiology
Virginia Commonwealth University
Richmond, VA 23298

MATERIALS AND METHODS

Collagen Isolation. Type I collagen was acid-extracted from calfskin corium (animals <6 months old; Lampire Biologics, Pipersville, Pa.). Corium was defrosted at 4^0C, diced into 10-20 cm^3 squares and placed into ice cold distilled water at a concentration of 25-50 g of solid per liter of solution. Glacial acetic acid was added to the suspension to bring the molarity to 0.5M, the solution was stirred and allowed to incubate for 12 hr at 4^0C. The ice cold suspension was then homogenized in a commercial grade blender (Waring) in 10-15 second bursts to limit heating. After an additional 48 hr of incubation at 4^0C under gentle stirring, the resulting collagen-rich solution was centrifuged for 12 hr at 14,000G (4^0C). Pellets were discarded, and the supernatant was dialyzed against 20 volumes of 18 MΩ-cm water. Water was changed 3-4 times while maintaining the dialysis at 4^0C. The extract was then frozen to -70^0C and lyophilized until dry.

Electrospinning. Reagents were purchased from Sigma Aldrich (St. Louis, MO) unless noted. Collagen was suspended in 2,2,2 trifluoroethanol (TFE) at 55, 70 or 90 mg/ml for 24 hr prior to electrospinning. Collagen suspensions were electrospun onto a stainless steel rectangular mandrel (70 mm x 10 mm x 5 mm) as previously described. The collagen solution was delivered at a rate of 8-12 ml/hr over an air gap distance of 20 cm and the target mandrel speed was set to 200 RPM to ensure the production of scaffolds composed of random elements. A digital stroboscope (Shimpo Instruments

DT3-11A) was used to continuously monitor the RPM of the target mandrel. Samples were stored in a desiccation chamber prior to analysis.

Materials Testing. Collagen scaffolds prepared from 55 mg/ml suspensions were removed from the mandrel and cut into dumbbell shaped samples using a die punch (2.67 mm wide, gauge length of 0.295 mm). The samples were then immersed in 0% (100% ethanol) 0.1%, 1%, 10% or 40% v/v glutaraldehyde prepared in ethanol for 12 hr. After cross-linking, each sample was sequentially washed in 15 minute rinses in 5%, 10%, 25%, 50%, and 75% PBS prepared in ethanol, followed by two PBS rinses. We have found that this graded series of rinses reduces solvent induced changes in fiber diameter (swelling). The thickness of each hydrated dumbbell shaped sample was determined with a Mitutoyo IP54 digital micrometer (Mitutoyo American Corp; Aurora, IL). Scaffolds were uniaxially tested to failure at an extension rate of 10 mm/min with a Bionix 200 Mechanical Testing Systems instrument (MTS Systems Corp, Eden Prairie, MN). Data sets were screened by one-way ANOVA ($P<0.01$) to test for the effects of cross-linking on material properties.

Cross-Linking Assay. Collagen scaffolds were removed from the mandrel and cut into 12 mm diameter disks using a dermal biopsy punch. The samples used for examining degree of cross-linking with regards to solvent identity were immersed in 0.5% v/v glutaraldehyde prepared in PBS, 100% ethanol, 99% water/1% ethanol, 50% water/50% ethanol, methanol, isopropyl alcohol or iso amyl alcohol. The samples used for investigating degree of cross-linking as a function of glutaraldehyde fixation were immersed in 0% (100% ethanol) 0.1%, 1%, 10% or 40% v/v glutaraldehyde prepared in ethanol for 12 hr and rinsed as previously described. All data is expressed as the percentage of cross-linking present in a sample with respect to the cross-linking present in a dry, un-crosslinked control sample cut from the same sheet of electrospun material as the experimental groups [Barnes]. Samples were placed into 2 ml of a solution containing 2.0% (w/v) of sodium bicarbonate and 0.25% 2,4,6-Trinitrobenzenesulfonic acid (TNBS) prepared in distilled water and heated for 2 hr at 40^0C. Next, 3 ml of 6M HCL was added to each sample and the samples were then incubated an additional 1.5 hr at 60^0C. Aliquots of equal volume from each sample were placed into a 96 well plate and read at 345 nm on a Spectramax Plus microplate spectrophotometer (Molecular Devices). Percent cross-linking was calculated from the formula:

$$\% \text{ Cross-linked} = 1- \frac{\text{Abs}_c}{\text{mass}_c} \Big/ \frac{\text{Abs}_{nc}}{\text{mass}_{nc}}$$

Where Abs_c= absorbance of the cross-linked sample at 345 nm; the unit of mass is given in mg. Abs_{nc}= absorbance of the untreated or non-cross-linked sample at 345 nm; the unit of mass is given in mg. This assay is colorimetric in nature and detects free amines. As the percentage of cross-linking increases in a sample, there is a parallel decrease in the number of free amines and therefore a decrease in the number of binding sites available for TNBS to interact with on the protein substrate. For statistical analysis, data sets were screened by one-way ANOVA, a Tukey test was used in pairwise comparison.

RESULTS

Cross-Linking: Varying Solvent Identity. The identity of the solvent used in the glutaraldehyde cross-linking solution was examined to determine how solvent identity affects degree of cross-linking and maintenance of scaffold integrity. Scaffolds electrospun from 55 mg/ml collagen solutions were cross-linked in 0.5% glutaraldehyde prepared in PBS, 100% ethanol, 99% water/1% ethanol, 50% water/50% ethanol, methanol, isopropyl alcohol or iso amyl alcohol. Scaffolds prepared in iso amyl alcohol revealed little cross-linking (38.2%) while scaffolds prepared in PBS or 99% water/1% ethanol demonstrated a high degree of cross-linking (68.5 and 70.1%, respectively) (Table B.1). However, all of these scaffolds exhibited poor scaffold integrity and showed signs of disintegration. Cross-linking the scaffolds in 50% water/50% ethanol or isopropyl alcohol produced scaffolds of reasonable structural integrity yet while the degree of cross-linking calculated from the water/ethanol solution was 69.2% the isopropyl alcohol demonstrated only 34.6% cross-linking. Scaffolds cross-linked using methanol and 100% ethanol produced scaffolds of excellent quality and a high degree of cross-linking (59.6 and 62.9%). For electrospun collagen scaffolds, the use of ethanol or methanol as the cross-linking solvent appears to be advantageous.

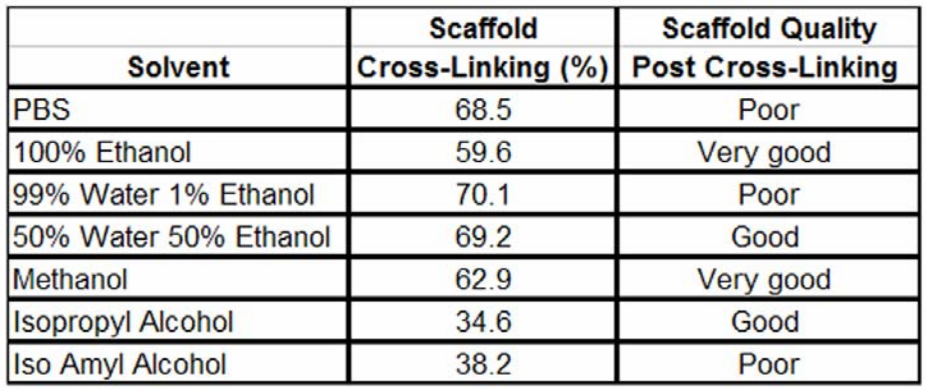

Solvent	Scaffold Cross-Linking (%)	Scaffold Quality Post Cross-Linking
PBS	68.5	Poor
100% Ethanol	59.6	Very good
99% Water 1% Ethanol	70.1	Poor
50% Water 50% Ethanol	69.2	Good
Methanol	62.9	Very good
Isopropyl Alcohol	34.6	Good
Iso Amyl Alcohol	38.2	Poor

Table B.1. Electrospun collagen cross-linked with various solvents. Electrospun collagen (55 mg/ml) scaffolds were cross-linked in 0.5% glutaraldehyde with the above solvents. Scaffolds cross-linked using PBS, 99% water/1% ethanol or iso amyl alcohol all yielded unusable scaffolds. Scaffolds cross-linked using 50% water/50% ethanol or isopropyl alcohol produced scaffolds of decent quality and in the case of 50% water/50% ethanol, acceptable cross-linking. Scaffolds cross-linked using 100% ethanol or methanol yielded scaffolds of excellent quality and a satisfactory degree of cross-linking.

Cross-Linking: Varying Glutaraldehyde Percentage. The degree of cross-linking present in an electrospun scaffold as a function of the percentage of glutaraldehyde was investigated in order to determine how cross-linking impacts scaffold material properties. In conjunction with these experiments we also examined how changes in fiber diameter might impact the degree of cross-linking that occurs in an electrospun scaffold. Collagen scaffolds were electrospun from starting concentrations of 55, 70 and 90 mg/ml and then cross-linked to varying degrees using a range of glutaraldehyde (0, 0.1, 1, 10 and 40%).

The degree of cross-linking present in the samples electrospun from 55 mg/ml collagen varied as a function of the initial percentage of glutaraldehyde present at the onset of cross-linking (Figure B.2). Our analysis indicated that 40.6% of the available sites were cross-linked in samples that were immersed in 0% glutaraldehyde:100% alcohol for 12 hr. At 0.1% glutaraldehyde, average cross-linking increased to 48.2%. Scaffolds processed in 1% glutaraldehyde were 55.3% cross-linked, scaffolds processed with 10% glutaraldehyde were 64.2% cross-linked and scaffolds processed in 40% glutaraldehyde were 66.1% cross-linked. One-way ANOVA indicated that samples cross-linked in 10 and 40% glutaraldehyde were different than samples processed in 0 and 0.1% glutaraldehyde ($P<0.05$). There was a subjective increase in the amount of cross-linking present in samples processed with 0, 0.1, and 1% glutaraldehyde; however, no statistical differences were detected among these groups (Figure B.2). In conjunction with these experiments we also examined how changes in fiber diameter might impact the degree of cross-linking that occurs in an electrospun scaffold.

The degree of cross-linking present in the samples electrospun from 70 mg/ml collagen varied as a function of the initial percent of glutaraldehyde present at the onset of cross-linking (Figure B.2). Our analysis indicated that 44.1% of the available sites were cross-linked in samples that were immersed in 0% glutaraldehyde:100% alcohol for 12 h. At 0.1% glutaraldehyde, average cross-linking increased to 60.6%. Scaffolds processed in 1% glutaraldehyde were 61.8% cross-linked, scaffolds processed with 10% glutaraldehyde were 65.1% cross-linked and scaffolds processed in 40% glutaraldehyde were 65.3% cross-linked. As demonstrated in collagen 55 mg/ml, one-way ANOVA indicated that samples cross-linked in 10 and 40% glutaraldehyde were different than samples processed in 0 and 0.1% glutaraldehyde ($P<0.05$).

The degree of cross-linking present in the samples electrospun from 90 mg/ml collagen varied as a function of the initial percent of glutaraldehyde present at the onset of cross-linking (Figure B.2). Our analysis indicated that 43.7% of the available sites were cross-linked in samples that were immersed in 0% glutaraldehyde:100% alcohol for 12 h. At 0.1% glutaraldehyde, average cross-linking increased to 53.6%. Scaffolds processed in 1% glutaraldehyde were 57.9% cross-linked, scaffolds processed with 10% glutaraldehyde were 73.3% cross-linked and scaffolds processed in 40% glutaraldehyde were 78.1% cross-linked. One-way ANOVA indicated that samples cross-linked in 10 and 40% glutaraldehyde were different than samples processed in 0, 0.1 and 1% glutaraldehyde ($P<0.05$).

For each concentration of glutaraldehyde used in these studies, the degree of cross-linking detected was similar in collagen scaffolds electrospun from concentrations of 55 and 70 mg/ml. However, collagen scaffolds electrospun from a concentration of 90 mg/ml demonstrated significantly different degrees of cross-linking to the 55 and 70 mg/ml collagen scaffolds. When compared to the 90 mg/ml scaffold cross-linked using 0% glutaraldehyde, the 55 mg/ml scaffolds cross-linked using 10 and 40% glutaraldehyde and the 70 mg/ml scaffolds cross-linked using 0.1, 1, 10 and 40% glutaraldehyde were cross-linked to higher degrees. The 90 mg/ml scaffold cross-linked using 1% glutaraldehyde was also cross-linked to a significantly higher degree when compared to the 70 mg/ml scaffold cross-linked using 0% glutaraldehyde. The 90 mg/ml scaffold cross-linked using 10% glutaraldehyde was cross-linked to a significantly higher degree when compared to the 70 mg/ml scaffold cross-linked using 0% glutaraldehyde and the 55 mg/ml scaffolds cross-linked using 0, 0.1 and 1% glutaraldehyde. The 90 mg/ml scaffold cross-linked using 40% glutaraldehyde was cross-linked to a significantly higher degree than all other when compared to the 55 mg/ml scaffolds cross-linked using 0, 0.1 and 1% glutaraldehyde and the 70 mg/ml scaffolds cross-linked using 0, 0.1, 1 and 10% glutaraldehyde.

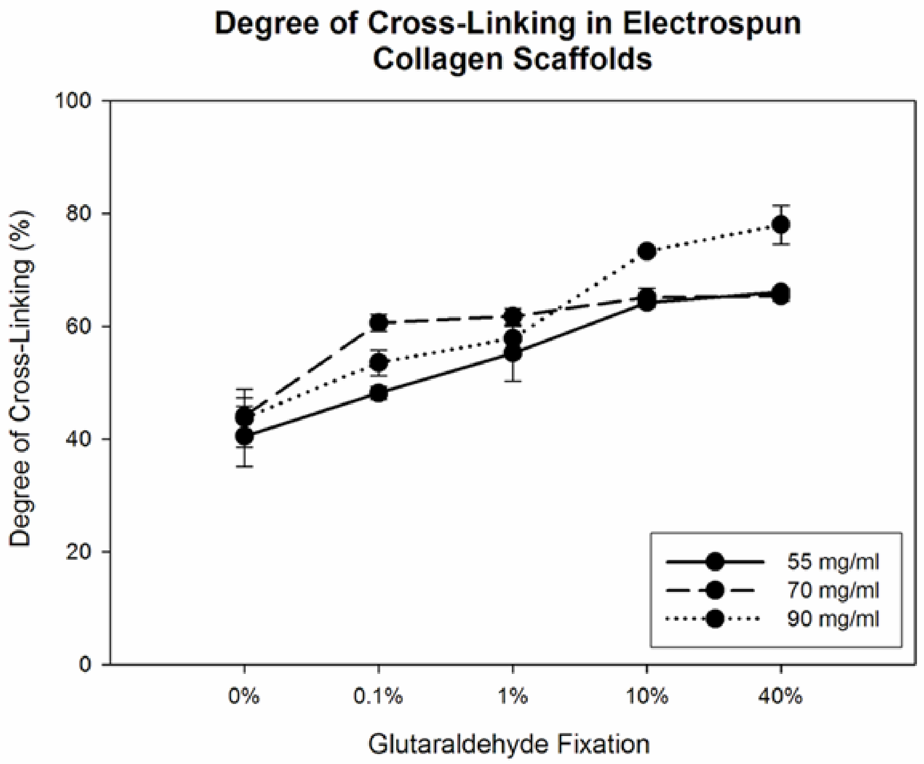

Scaffold Cross-linking (%)			
	Collagen Concentration		
Fixation	***55 mg/ml***	***70 mg/ml***	***90 mg/ml***
0%	40.6	44.1	43.7
0.10%	48.2	60.6	53.6
1%	55.3	61.8	57.9
10%	64.2	65.1	73.3
40%	66.1	65.3	78.1

Figure B.2. Electrospun collagen scaffold cross-linking. Degree of cross-linking increases as a function of starting electrospinning concentration and % glutaraldehyde in the cross-linking solution.

Material Properties. The material properties of the electrospun scaffolds varied as a function of the degree of cross-linking present in the samples. Stress at failure in scaffolds processed in 100% ethanol that were cross-linked 40.6% was 0.143 MPa (Figure B.2 A). This value ranged upward as the degree of cross-linking increased in the samples. For example, stress at failure in scaffolds cross-linked 48.2% was 0.255 MPA, samples cross-linked 55.3% exhibited a value of 0.283 MPa, samples cross-linked 64.2% exhibited a value of 0.317 MPa and samples cross-linked 66.1% exhibited a value of 0.325 MPa. Screening these data sets by one-way ANOVA indicated that stress at failure was similar in scaffolds processed with 10 and 40% glutaraldehyde ($P<0.001$). These results are not surprising given the observation that the percentage of cross-linking present in these samples is very similar (64.2 and 66.1% cross-linked, respectively). Stress at failure was different in scaffolds cross-linked 48.2, 64.2 and 66.1% with respect to scaffolds processed in 100% ethanol and cross-linked 40.6% ($P<0.004$).

Strain at failure, as judged by bulk materials testing, also varied as a function of the percentage of cross-linking induced into the samples (Figure B.2 B). Scaffolds processed in 100% ethanol and nominally cross-linked 40.6% exhibited a strain of 233% at failure. Scaffolds cross-linked 48.2% had an average strain value of 168% at failure, scaffolds cross-linked 55.3% demonstrated an average strain value of 210% at failure, scaffolds cross-linked 64.2% exhibited an average strain value of 169% at failure and scaffolds cross-linked 66.1% revealed an average strain value of 123% at failure. Once again, screening these data sets by one-way ANOVA indicated that strain at failure was similar in scaffolds processed in 10% glutaraldehyde (64.2% cross-linked) and 40%

glutaraldehyde (66.1% cross-linked) ($P<0.005$). Strain at failure in these scaffolds was different with respect to scaffolds cross-linked 40.6% ($P<0.005$). In addition, strain was different in scaffolds cross-linked 66.1% with respect to scaffolds cross-linked 55.3% ($P<0.005$), and scaffolds cross-linked 48.2% were different from scaffolds cross-linked 40.6% ($P<0.005$).

Consistent with these observations, modulus was lowest in scaffolds processed in 100% ethanol with respect to all other conditions assayed ($P<0.005$) (Figure B.2 C). This material property was increased in scaffolds processed in 40% glutaraldehyde (66.1% cross-linked) with respect to samples processed in 1% glutaraldehyde (48.2% cross-linked). Together, these data indicate that changes in cross-linking introduce fundamental changes into the structure of an electrospun collagen scaffold.

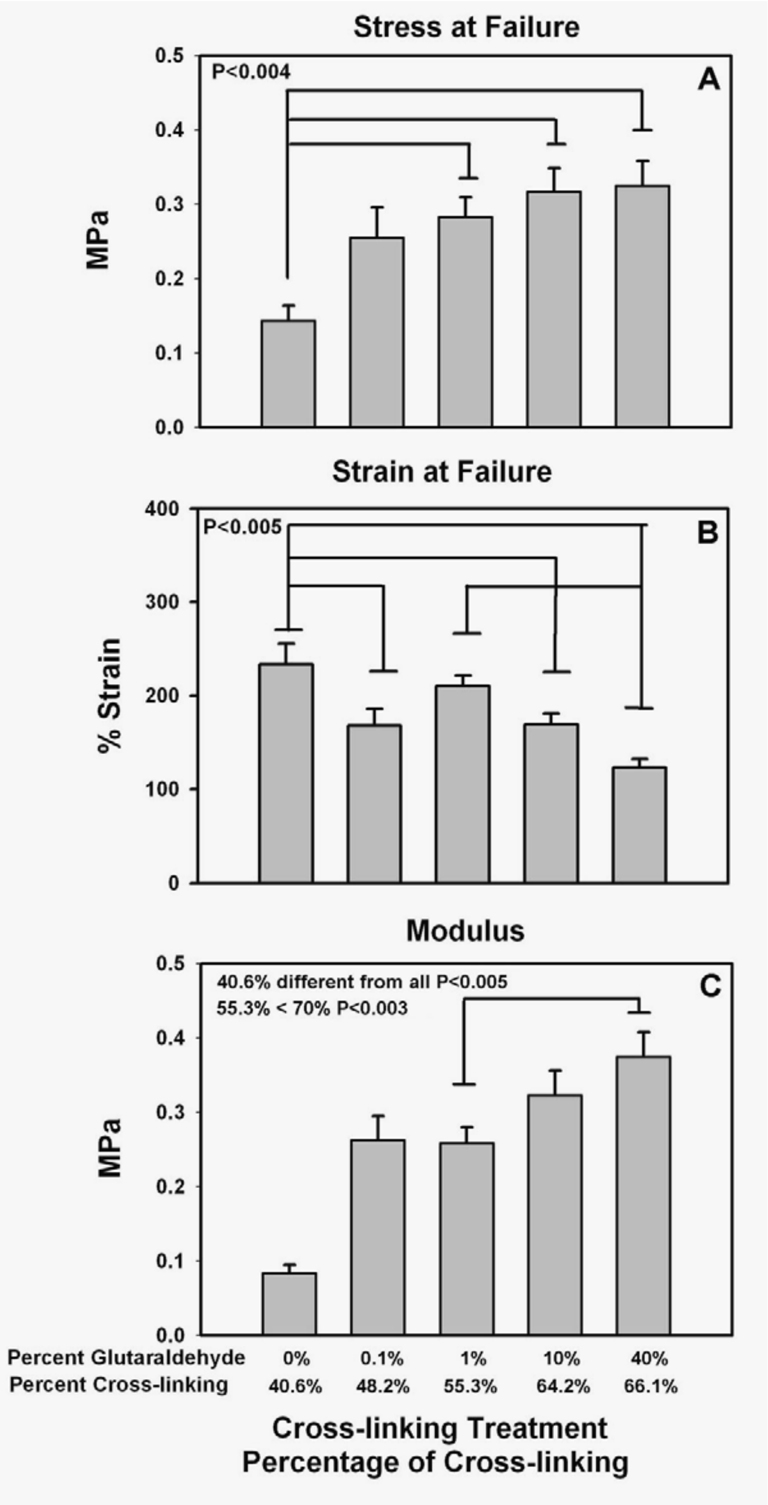
Stress at Failure
A
P<0.004
MPa
0.5
0.4
0.3
0.2
0.1
0.0
Strain at Failure
B
P<0.005
% Strain
400
300
200
100
0
Modulus
C
40.6% different from all P<0.005
55.3% < 70% P<0.003
MPa
0.5
0.4
0.3
0.2
0.1
0.0
Percent Glutaraldehyde
0%
0.1%
1%
10%
40%
Percent Cross-linking
40.6%
48.2%
55.3%
64.2%
66.1%
Cross-linking Treatment
Percentage of Cross-linking

Figure B.2 A-C. Material properties of electrospun collagen scaffolds as a function of cross-linking. Stress at failure (A) was similar in all samples with the exception that stress was decreased in scaffolds processed in 100% ethanol (no glutaraldehyde) with respect to all other scaffolds ($P<0.004$). Strain at failure (B) generally decreased as a function of increasing glutaraldehyde concentration ($P<0.005$). The modulus increased as a function of increased cross-linking ($P<0.005$)

DISCUSSION

The percentage of cross-linking present in the scaffolds did not change to any great extent in samples processed in 1, 10 and 40% glutaraldehyde (*e.g.* Figure B.1). Despite this result, scaffolds processed under these conditions exhibited subtle differences in material properties. We believe these differences can be attributed to the chemistry of glutaraldehyde and specific structural changes imparted on individual fibers by this cross-linking agent. Glutaraldehyde is described as a zero distance cross-linker, and as such, this agent should primarily impact the structure of individual fibers. However, at high concentrations glutaraldehyde can undergo polymerization, effectively increasing its cross-linking distance [23]. Highly cross-linked scaffolds also exhibit less elasticity than scaffolds processed with nominal amounts of cross-linking. Highly cross-linked scaffolds lack the coiled structures that appear to dampen the initial effects of strain on a scaffold that has been subjected to a nominal degree of cross-linking (*e.g.* “no coils to uncoil”).

We have detected evidence of cross-linking in scaffolds processed in 100% ethanol and believe this represents an artifact of the alcohol induced precipitation process; precipitation appears to sequester amines within the structure of the partially stabilized fibers, effectively reducing the number of TNBS binding sites. We note that ethanol treated scaffolds are stable in an aqueous environment when hydrated, including the bicarbonate/TNBS solution used in our cross-linking assay. In contrast, the dry, electrospun scaffolds that we use to generate baseline values of cross-linking undergo complete dissolution (nearly immediately) when exposed to the bicarbonate/TNBS buffer system used in the cross-linking assay. In theory, dissolution exposes all available sites to the colorimetric agent, thereby “inflating” the total number of binding sites that can be detected by the assay. The putative sequestered sites that we believe are present in the ethanol processed samples appear to exist in a very stable compartment and do not appear to be particularly susceptible to cross-linking with glutaraldehyde. It is possible that the glutaraldehyde does not effectively penetrate the surface of the electrospun fibers (possibly because the ethanol extracts water from the collagen) in the alcohol-based solvent system, a condition that may lead to the formation of a cross-linked “shell” on the fibers. We believe that as a result of these effects we cannot achieve 100% cross-linking under the conditions used to process our fibers.

Modulating the percentage of cross-linking present in a hydrated scaffold served to induce incremental changes in scaffold material properties. Scaffolds processed in 100% ethanol and low concentrations of glutaraldehyde exhibited a very regional response to strain. The hydrogen bonds present in these samples appear to stabilize the structure of individual fibers, however, it is unlikely these bonds can mediate fiber-to-fiber interactions to any great extent, resulting in a non-uniform response to strain. Similar arguments may explain why scaffolds processed in low concentrations of glutaraldehyde (<1%) exhibit this same behavior, especially if the use of an alcohol carrier induces the formation of a structure (“shell”) that largely excludes glutaraldehyde from the interior of the fibers. Strains were uniformly distributed in the scaffolds as the concentration of glutaraldehyde was increased beyond 1%.

In closing, the material properties of electrospun scaffolds can be modulated at several sites in the fabrication process. For example, the introduction of varying degrees of fiber alignment into a scaffold at the time of fabrication (through the use of rotating target mandrels) can be used to modulate the anisotropic material properties of this unique class of nano-scale biomaterials. We explored how changes in cross-linking hydration can be used to modulate the material properties of the electrospun scaffold; it should be possible to exploit this property to directly tailor these biomaterials to specific applications. For example, the introduction of high degrees of cross-linking into scaffolds composed of highly aligned fibers might be used to produce constructs that mimic relatively inelastic connective tissues like ligaments and tendons.

VITA

Chantal Emma Ayres was born in Surrey, England on March 4, 1980. She was raised in Fairfax, Virginia and graduated from W.T. Woodson High School in 1998. She attended Virginia Tech from August 1998 to May 2002 and was awarded a Bachelor of Science in Electrical Engineering. Shortly after graduating from Virginia Tech, she became a naturalized citizen of the United States of America. In January 2003 she began her graduate work at Virginia Commonwealth University and was awarded a Master of Science in Biomedical Engineering in December 2004. She began her doctoral work in August 2005. She currently resides in Richmond, Virginia with her husband-to-be, Christopher Sander, and their dog, Dozer, and two cats, Frank and Reggae.